

**Université de Lille**



École Doctorale Sciences Pour l'Ingénieur Lille Nord-de-France-072  
IEMN - Institut d'électronique de microélectronique et de nanotechnologie  
LIMMS/CNRS-IIS (UMI 2820)

Thèse présentée par

**Yuki TAKAYAMA**

En vue de l'obtention du grade de  
**Docteur de l'Université de Lille**

**Spécialité : Micro-nanosystèmes et capteurs**

**Développement d'un microsysteme intégrant les  
fonctions microfluidiques pour la caractérisation  
biophysique de cellules cancéreuses uniques**

Présentée et soutenue publiquement le 28 mars 2019

Membres du jury :

Directeur de thèse :	<b>D. Collard</b>	IEMN / CNRS
Rapporteurs :	<b>C. Dejous</b> <b>V. Taly</b>	IMS, Université de Bordeaux Université Sorbonne Paris Cité / INSERM, CNRS
Examineurs :	<b>C. Legallais</b> <b>C. Lagadec</b> <b>M. C. Tarhan</b>	Université de Technologie de Compiègne / CNRS CPAC, Université de Lille / INSERM ISEN Lille/ Yncréa
Invité :	<b>H. Fujita</b>	IIS, The University of Tokyo

Univeristy of Lille



École Doctorale Sciences Pour l'Ingénieur Lille Nord-de-France-072  
IEMN - Institut d'électronique de microélectronique et de nanotechnologie  
LIMMS/CNRS-IIS (UMI 2820)

Thesis submitted by

**Yuki TAKAYAMA**

In order to obtain the grade of  
**Doctor from the University of Lille**

**Specialty : Micro-nanosystems and sensors**

**MEMS Device with Built-in Microfluidics  
for Biophysical Characterization  
of Single Cancer Cells**

Presented and publicly supported on March 28, 2019

Jury members:

Thesis supervisor:	<b>D. Collard</b>	IEMN / CNRS
Rapporteurs :	<b>C. Dejous</b>	IMS, Université de Bordeaux
	<b>V. Taly</b>	Université Sorbonne Paris Cité / INSERM, CNRS
Examiners :	<b>C. Legallais</b>	Université de Technologie de Compiègne / CNRS
	<b>C. Lagadec</b>	CPAC, Université de Lille / INSERM
	<b>M. C. Tarhan</b>	ISEN Lille/ Yncréa
Guest :	<b>H. Fujita</b>	IIS, The University of Tokyo



# **MEMS Device with Built-in Microfluidics for Biophysical Characterization of Single Cancer Cells**



Institute of Industrial Science,  
The University of Tokyo



**Yuki Takayama**

L'École Doctorale Sciences Pour l'Ingénieur Lille Nord-de-France  
Université de Lille

This dissertation is submitted for the degree of  
*Doctor of Micro-nano systèmes et capteurs*

I dedicate this thesis to my beloved family.

## **Declaration**

I declare that except where specific reference is made to the work of others, the contents of this thesis are original and have not been submitted, in whole or in part, in any previous application for any other degree or qualification in this, or any other university. This thesis is my own work and contains nothing which is the outcome of work done in collaboration with others, except as specified in the text and acknowledgements. Parts of this work presented in Chapter 3 have been published in [Developing a MEMS Device with Built-in Microfluidics for Biophysical Single Cell Characterization].

Yuki Takayama

June 2019

## Résumé

Les masses tumorales, en se développant, permettent aux cellules cancéreuses d'acquérir un phénotype spécifique qui les rendent résistantes aux traitements et leur procure la possibilité d'envahir les tissus environnants, la circulation sanguine périphérique et diffuser dans l'organisme. Le traitement des tumeurs primaires par voie chirurgicale est la plupart du temps efficace, par contre cibler les cellules tumorales disséminées dans les organes distants restent extrêmement complexe. En conséquence, ~90 % de la mortalité liée au Cancer est due aux développements tumoraux sur des sites secondaires: les métastases. Le changement de phénotype de la cellule nécessaire à la progression métastatique s'accompagne également d'une réduction significative de sa rigidité qui lui permet de s'insérer dans les tissus environnants. De ce fait, la caractérisation des propriétés biomécaniques peut s'avérer être une approche originale pour détecter les cellules cancéreuses dans le réseau sanguin (les cellules tumorales circulantes).

De manière récurrente, les différentes techniques s'exposent à un compromis entre le débit de caractérisation (nombre de cellules traitées en un temps donné) et son contenu (nombre et précision des paramètres mesurés). Certaines techniques telle que la microscopie à force atomique (AFM) permettent des mesures très précises mais souffre d'un débit de caractérisation extrêmement faible, les méthodes basées sur la micro fluidique s'apparentant à la cytométrie de déformabilité en flux permettent des débits de mesures intéressants mais souffre d'un déficit de contenu ne permettant pas d'identifier précisément les différents phénotypes cellulaires.

Les cellules circulantes ont des tailles microniques (10-30 microns de diamètre), les microtechnologies présentent donc de multiples avantages dimensionnels pour les manipuler, les stimuler et les caractériser de manière individuelle. De ce fait, les MEMS (Micro Electro Mechanical Systems) s'avèrent des dispositifs tout à fait adaptés pour mesurer les différents paramètres biophysiques, propriétés mécaniques et électriques de cellule uniques. Cependant les dispositifs MEMS sont inopérants dans un environnement liquide conducteur pour y réaliser les caractérisations électriques et mécaniques. Afin de s'affranchir de cette limitation, cette étude

---

propose de séparer la partie qui manipule la cellule dans son environnement biologique et les actionneurs et capteurs du MEMS réalisant les mesures électriques et mécaniques. De plus, pour augmenter le débit de caractérisation et permettre une bonne opérabilité, le dispositif MEMS intègre directement le canal microfluidique dans lequel les cellules vont circuler.

Cette thèse propose un dispositif original qui permet la mesure simultanée des caractéristiques électriques et mécaniques de cellules circulantes uniques. Dans un premier temps, différentes lignées cellulaires sont comparées sur la base de caractérisations mécaniques réalisées par AFM, une technique qui, ici, s'est avérée difficile à mettre en œuvre pour ces cellules circulantes. Ensuite, des nanopincettes en silicium (SNTs, Silicon Nano tweezers) ont été modifiées pour permettre la manipulation de cellules et ont permis de concevoir et tester les éléments de base du futur dispositif MEMS, les caractérisations réalisées par les SNT ont permis de distinguer des cellules connues pour avoir des potentiels métastatiques différents. Finalement, la conception du nouveau dispositif MEMS intégrant le canal microfluidique est détaillée. Les actionneurs et les capteurs du dispositif ont ensuite été optimisés pour améliorer la sensibilité des mesures et le dispositif complet a ensuite été validé par la manipulation et les mesures électriques et mécaniques de cellules uniques.

Cette étude montre que les SNT sont capables de distinguer différentes lignées cellulaires par leur propriétés mécaniques. En exploitant la topologie des SNT, un micro dispositif original intégrant le canal microfluidique pour le transport des cellules a été conçu, optimisé, fabriqué et testé. Ce dispositif est capable de contrôler les écoulements des solutions dans le micro canal, et de détecter les effets mécaniques et électriques induits par différents types de solutions ayant des viscosités (solution avec différentes concentrations de glucose) et des conductivités variées (solution ayant différentes concentrations de NaCl). Ce dispositif est également capable de capturer des cellules uniques dans le canal intégré. Les cellules capturées ont été caractérisées mécaniquement et électriquement pour en extraire les informations relatives à leur taille, leur rigidité, leurs pertes visqueuses ainsi que leurs propriétés électriques. En conclusion, les analyses multi-paramètres réalisées par ce nouveau dispositif s'avère être une voie prometteuse pour examiner le caractère métastatique de cellules tumorales circulantes.

## Abstract

Tumour mass, as they develop, allows cancer cells to acquire specific phenotype with high resistance to treatments and, more importantly, ability to invade surrounded tissues to the extent that they can reach blood circulation and spread over the body. While targeting primary tumour with surgery is, most of the time, efficient, getting rid of spread cells in distant organs is meanwhile extremely challenging. As consequences, ~90 % of cancer deaths are induced by the development and growth of secondary cancer sites: metastasis. Interestingly, changes in phenotype during metastasis progression require drastic adaptation in cell morphology, switching from the rigid structure to a stretch/softer one, allowing deformability of cells to migrate through tissues. Thus, characterization of cell biomechanical properties could be a game changer by allowing the detection of spreading cells in blood (circulating tumour cells) and the prediction of metastatic potential or response to treatments.

There have been various techniques used for single cell biophysical (mainly mechanical) characterization. As a common issue, there is a trade-off between throughput and information content. Certain techniques such as Atomic Force Microscopy (AFM) allow very sensitive measurements but suffer from low-throughput while microfluidics-based methods like deformability cytometry provide rapid measurements but with limited information content. Due to the heterogeneity of cancer cells, a preferred characterization method should provide multi-parameter analysis for high performance without compromising neither the sensitivity nor the practicality.

Considering the dimensions of cells, using microtechnologies has numerous advantages to handle single cells for stimulation and detection. Biophysical properties, such as mechanical and electrical, can be targeted by the MEMS technology. However, MEMS devices perform poorly in conductive liquids for both mechanical and electrical detection. Therefore, this study proposes to separate the biological sample handling from mechanical actuation and electrical detection regions of a MEMS device. Moreover, to improve the throughput and provide higher practicality, the MEMS device is designed to have an integrated microfluidic channel.

In this thesis, a novel device has been introduced to perform simultaneous mechanical and electrical characterization of single circulating cells. Initially, different cell lines are compared based on mechanical properties obtained by AFM which perform poorly on circulating cells. As the next step, Silicon NanoTweezers (SNTs), modified to perform measurements on single cells, are used to test the MEMS elements of the proposed device as well as to distinguish cell lines with different metastatic potential. Finally, the proposed device is designed to have a microchannel integrated with the MEMS elements. The stimulating and detecting MEMS elements are optimized for better performance and the device is tested to perform single cell measurements.

Although the AFM measurements suffer from serious shortcomings when applied on circulating cells, this study shows that SNT can be used to distinguish different cell lines based on their mechanical properties. Using the SNT geometry, the proposed device with integrated microchannel is designed, optimized, fabricated and tested. The optimized device is capable of handling solutions inside the channel, and also detecting the mechanical and electrical alterations among various solutions having different viscosity and ionic strength. The device is also tested on capturing a single cell. The captured cells are used for performing mechanical and electrical measurements simultaneously to provide information on the size, stiffness and viscous losses together with electrical properties. To conclude, the practical multi-parameter analysis provided with the proposed device is a promising way to investigate the metastatic potentials of circulating tumour cells.

## Publications

1. **Yuki Takayama**, Grégoire Perret, Momoko Kumemura, Manabu Ataka, Samuel Meignan, Stanislav Karsten, Hiroyuki Fujita, Dominique Collard, Chann Lagadec, Mehmet Cagatay Tarhan, “Developing a MEMS Device with Built-in Microfluidics for Biophysical Single Cell Characterization”, *Micromachines*, Vol. 9, No. 6, p. 275, Jun. 2018.  
DOI: <https://doi.org/10.3390/mi9060275>
2. **Yuki Takayama**, Grégoire Perret, Momoko Kumemura, Chann Lagadec, Samuel Meignan, Manabu Ataka, Hiroyuki Fujita, Mehmet Cagatay Tarhan, Dominique Collard, “Simultaneous electrical and mechanical characterization of single cells by an integrated device”, *The 31st IEEE International Conference on Micro Electro Mechanical Systems (MEMS 2018)*, 2018, pp. 297-300, Jan. 2018.
3. Grégoire Perret, **Yuki Takayama**, Momoko Kumemura, Samuel Meignan, Hiroyuki Fujita, Chann Lagadec, Dominique Collard and Mehmet Cagatay Tarhan, “Mechanical characterization of single cells to distinguish different breast Cancer cells”, *The 21st International Conference on Miniaturized Systems for Chemistry and Life Sciences*, pp. 978-0-692-94183-6, Oct. 2017.
4. Tiffany Baëtens, Grégoire Perret, **Yuki Takayama**, Momoko Kumemura, Laurent Jalabert, Samuel Meignan, Chann Lagadec, Fujita Hiroyuki, Dominique Collard, Mehmet Cagatay Tarhan, “A practical single cell analysis method for mechanical characterization of cancer cells”, *The 30th IEEE International Conference on Micro Electro Mechanical Systems (MEMS 2017)*, 2017, pp. 608-611, Jan. 2017.



5. Mehmet Cagatay Tarhan, Grégoire Perret, Nicolas Lafitte, Momoko Kumemura, Laurent Jalabert, **Yuki Takayama**, Stanislav L. Karsten, Hiroyuki Fujita and Dominique Collard, “MANIPULATING DIFFERENT BIOLOGICAL SAMPLES BY SILICON NANOTWEEZERS”, The 8th International Conference on Microtechnologies in Medicine and Biology (MMB 2016), Apr. 2016.

## Acknowledgements

This work was conducted in SMMiL-E (Seeding Microsystems in Medicine in Lille, European-Japanese technology against Cancer) laboratory which is the research collaboration unit between the Institute of Industrial Science (IIS) - The University of Tokyo, CNRS, Center Oscar Lambret, and Lille 1 University, from October 2015 to September 2018. There are so many people who have been involved in the creation of this work and have helped me during the PhD. My research would never have existed without their support. There is not enough space, nor time to acknowledge everyone to the extent they deserve. I hope people understand the brevity of this part.

First of all, I would like to thank my doctorate advisors Prof. Dominique Collard (IEMN, CNRS, France) and Prof. Hiroyuki Fujita (IIS, The University of Tokyo, Japan) for their friendship, enthusiasm, energy, and fortitude to the research. In a special environment of French-Japanese joint laboratory, this work would not have been possible without their guidance and supports. By conducting research of boundary fields with people from different countries, I could learn from different cultures, points of view and way of thinking in each field and it was really impressed me. I look forward to continued interactions and collaborations with them in the future. Thanks for supporting and encouraging me through these years.

Secondly, I am highly grateful to my Co-supervisors, Prof. Mehmet Cagatay Tarhan. He always worked to promote me in the planning aspects of experiments and journal writing. He advised me many things for my experiments and also my presentation at the lab meeting. He always provided sound advice and guidance, and I am truly grateful.

Also, I would like to thank to my second Co-supervisors, Prof. Chann Lagadec for every biologically relevant things. As I am from the background of the electrical engineering, I started from scratch for all biological things. I am grateful his significant assistance, advice for the research, and personal encouragement.

Thirdly, I would like to thank the member of my oral defence committee. It was a great honour and a privilege for me to have the chance too present my research work to them.

I am also grateful to Dr. Laurent Jalabert for teaching me all fabrication techniques in the cleanroom. Without his previous works and experiences, I could not done efficiently of my fabrication process and might be never succeeded in developing a new channel integrated device.

I would like to thank Dr. Manabu Ataka and Dr. Hiroaki Honma for their helps, supports and valuable advice when I faced troubles in the cleanroom.

I would like to express real thanks for kindly advice, useful discussions, helping my experiments and taking care of many stuffs in the experiment room to Dr. Momoko Kumemura and Dr. Grégoire Perret.

I wish to thank Prof. Teru Okitsu and Prof. Shoji Takeuchi for their significant assistance through the SMMiL-E project and always providing valuable advice.

I am grateful to Prof. Teruo Fujii for hosting me in his lab at the IIS, The University of Tokyo and for some advice. The content being carried out in his lab was very close to my work and it was really stimulated me. Also, I would like to express real thanks for warmly welcome to Prof. Fujii lab to all Fujii lab member. I would like to express thanks to Dr. Shohei Kaneda and Dr. Toshiro Maekawa in Fujii lab for providing me various advice and assistance.

I am highly grateful to Prof. Frank Lafont for providing me the permission to use AFM in his lab (CMPI - Microbiologie Cellulaire et Physique de l'Infection) at Institut de Biologie de Lille. Also, I wish thank to Dr. Sébastien Janel for providing me a technical training of AFM. During AFM experiments, they always helped a lot and gave me useful advice and comments.

I would like to express my gratitude to Dr. Samuel Meignan. When I asked many things what I needed in the experiment at IRCL, everything was arranged by him.

My thanks to all member who works in IRCL, especially technicians at Centre Oscar Lambret, Mélanie Arcicasa, Christine Bal and Nicole Lemahieu. Without their supports and kindness helps, my work could not exist.

I am also grateful to Dr. Nathalie Jouy for handling the Cellsorter to sort cancer cells and providing her techniques of the sorting machine at IRCL.

I am grateful for what I have received from every members of the laboratory of LIMMS in Japan and INSERM U908 in France.

I wish to thank all Fujita-lab members, especially Dr. Takaaki Sato, Dr. Matthieu Denoual (CNRS) and Mr. Hiroyuki Mitsuya (SAGINOMIYS SEISAKUSYO, Inc.) for their supports and fruitful discussions.

Also, special thanks to my all friends in IIS side, especially Shunsuke Yamada (Toshiyoshi-lab), Vivek Menon (Toshiyoshi-lab), Chikako Sano (Toshiyoshi-lab), Saeko Tachikawa (Nomura-lab), Nicolas Lobato-Dauzier (Fujii-lab), Ryohei Yagi (Okabe-lab) and Ryo Usuba (Matsunaga-lab), Stephany Mai Nishikawa (Fujii-lab), Chi Je Park (Fujii-lab), Shu Okumura (Fujii-lab) and Mingyue Sun (Fujii-lab) for their endless friendship and the pleasure time spent together.

I have friends in French side as well. I wish to thank Justine Bailleul (Lagadec-lab), Nadège Bidan (Lagadec-lab) and Quentin Bailleul (Meignan-lab). Thanks to their kindness support when I staying in France, I was able to have fun with them while that period. They have been great friends who gave me with courage to move forward.

I would like to thank many administrative staffs who during my work, give me many helps and kindness supports. In a random order, Mrs. Yumi Hirano (CNRS), Mrs. Véronique Labbé (SMMiL-E), Mrs. Minako Makino (Fujita-lab), Mrs. Yoshiko Iwamoto (Fujii-lab) and all LIMMS secretaries.

The financial support provided by SIRIC ONCOLille - Site de Recherche Intégrée sur le Cancer was indispensable and I am grateful.

And Finally and the most important, I would like to thank my family Youji Takayama, Teiko Takayama and Hayato Takayama, and also my husband Masakazu Kondo for their unconditional love and encouragement that lead me the highest degree in the world. I made a lot of worries for my research life which come back and forth between France and Japan. Thank you for supporting me through three years.

# Table of contents

<b>List of figures</b>	<b>xv</b>
<b>List of tables</b>	<b>xxii</b>
<b>Symbols</b>	<b>xxiii</b>
<b>1 Introduction to BioMEMS</b>	<b>1</b>
1.1 Introduction . . . . .	1
1.1.1 Cancer and cell biomechanics . . . . .	1
1.1.2 Previous research on cells characterisation . . . . .	3
1.1.3 Advancement of MEMS . . . . .	7
1.1.4 Bio-medical applications of MEMS . . . . .	7
1.2 Purpose and significance of this study . . . . .	9
1.3 Organization of thesis . . . . .	12
<b>2 A proof of concept for MEMS based single cell biophysical characterization</b>	<b>15</b>
2.1 Introduction . . . . .	15
2.2 Applied AFM as the conventional method to floating cells measurements . . . . .	16
2.2.1 Background of AFM measurements . . . . .	16
2.2.2 Adapting AFM experiments to non-adherent cells . . . . .	16
2.2.2.1 Concept of PDMS wells . . . . .	16
2.2.2.2 Cell size measurement . . . . .	17
2.2.2.3 Preparation of cells . . . . .	19
2.2.3 Cell biomechanical properties measurements by AFM . . . . .	20
2.2.4 Data analysis . . . . .	22
2.2.5 Conclusions . . . . .	25

---

2.3	Using Silicon NanoTweezers technology to examine non-adherent cells . . . . .	27
2.3.1	Background of SNT . . . . .	27
2.3.2	Adapting the SNT design for single cancer cell measurements . . . . .	29
2.3.2.1	Gap distances . . . . .	30
2.3.2.2	Mechanical suspensions . . . . .	32
2.3.2.3	Electrostatic force . . . . .	34
2.3.2.4	Instability of comb drive . . . . .	35
2.3.3	Fabrication process . . . . .	36
2.3.4	Experimental process . . . . .	38
2.3.4.1	Device preparation . . . . .	38
2.3.4.2	Setup . . . . .	39
2.3.4.3	Cell preparation . . . . .	40
2.3.4.4	SNT experiment protocol . . . . .	40
2.3.5	Single cell characterization . . . . .	42
2.3.6	Data analysis . . . . .	47
2.3.6.1	Comparison between fixed and live SUM159PT cells . . . . .	49
2.3.6.2	Comparison between live SUM159PT and T47D cells . . . . .	49
2.3.7	Conclusions . . . . .	50
2.4	Conclusions . . . . .	52
<b>3</b>	<b>Development of a built-in channel device for single cell biophysical characteriza-</b>	
	<b>tion</b>	<b>53</b>
3.1	Introduction . . . . .	53
3.2	Working principle and design . . . . .	54
3.2.1	Principle . . . . .	54
3.2.2	Design description . . . . .	56
3.3	Fabrication . . . . .	66
3.4	Experimental setup . . . . .	68
3.4.1	Setup . . . . .	68
3.4.1.1	Liquid Handling . . . . .	70
3.4.1.2	Mechanical detection method . . . . .	72
3.4.1.3	Electrical detection method . . . . .	73

---

3.5	Device evaluation . . . . .	73
3.5.1	Frequency response and real time analysis . . . . .	73
3.5.2	Mechanical measurements . . . . .	75
3.5.3	Electrical measurement . . . . .	78
3.6	Conclusions . . . . .	81
<b>4</b>	<b>Cell biophysical characterization with a built-in channel device</b>	<b>82</b>
4.1	Introduction . . . . .	82
4.2	Single cell capturing procedure . . . . .	83
4.3	Results . . . . .	85
4.3.1	SUM159PT (fixed) . . . . .	85
4.3.2	Correction of data acquisition time lagging . . . . .	90
4.3.3	MCF7 (fixed) . . . . .	93
4.3.4	Electrical measurement . . . . .	96
4.4	Discussions . . . . .	96
4.4.1	Comparison between fixed SUM159PT and MCF7 . . . . .	96
4.4.2	Comparison between SNT and the developed MEMS device . . . . .	98
4.5	Conclusions . . . . .	99
<b>5</b>	<b>Conclusions and future work</b>	<b>101</b>
5.1	Conclusions . . . . .	101
5.2	Recommendations for further research . . . . .	104
	<b>References</b>	<b>108</b>
	<b>Appendix A PDMS microwell fabrication</b>	<b>118</b>
	<b>Appendix B CSC staining</b>	<b>120</b>
	<b>Appendix C Working principle</b>	<b>121</b>
	<b>Appendix D SNT fabrication process</b>	<b>123</b>
	<b>Appendix E A built-in channel MEMS device fabrication process</b>	<b>130</b>

# List of figures

1.1	Schematic images of the biomechanics techniques used to probe subcellular regions are given in <b>(a)-(c)</b> . Techniques used to probe the deformation of single cells are given in <b>(d)-(g)</b> . Techniques used to infer cytoadherence, deformation and mobility characteristics of populations of cells are schematically sketched in <b>(h)</b> and <b>(i)</b> . [10] . . . . .	4
1.2	MEMS and sensors market revenue from 2018 to 2023 (y-axis is USB\$) [59]. .	8
1.3	Measuring cell mechanics [73]. <b>(A)</b> An apparently exponential increase in cell mechanics publications over the past two decades, sorted by measurement technique. DC falls under the category of hydrodynamic deformation, or HD. <b>(B)</b> Image of the HD technique applied by Tse et al. [43]. <b>(C)</b> Schematic image of the trade-off between cell-sampling rate and information content of the different techniques. <b>(D)</b> Schematic image of the trade-off between cells measured and information content of the different techniques. . . . .	10
1.4	Overview of the on-chip measurement system for cellular mechanical characteristics [88]. . . . .	12
2.1	Using AFM for single cell analysis. <b>(a)</b> The conventional AFM indentation test with the adherent cell. <b>(b)</b> AFM faces certain difficulties when applied on floating cells. <b>(c)</b> Using PDMS wells for cell capturing during AFM indentation test. <b>(d)</b> PDMS wells installed inside a petri dish prior to AFM measurements.	17
2.2	Measurement of cancer cells size on different cell lines. Prepared cell lines were as follow: <b>(a)</b> SUM159PT, <b>(b)</b> 4T1, <b>(c)</b> MCF7 and <b>(d)</b> MDA-MB-231. . . . .	18
2.3	Microscope images of the fabricated PDMS microwells. <b>(a)</b> The aligned PDMS holes (at low magnification). <b>(b)</b> Tilted image of PDMS holes. . . . .	19



2.4	PDMS microwells, the cantilever with a sphere tip and the captured floating cell seen under the microscope of AFM. . . . .	21
2.5	Typical force-distance curve of the cell by sphere tip. This curve was taken from non-CSC group. The extend curve is black and the retract curve is red. . . . .	22
2.6	Geometric interaction between sphere tip and surface of the object. . . . .	23
2.7	Histogram of analyzed Young's modulus between non-CSC and CSC1, CSC2, and CSC3. . . . .	24
2.8	Yount's modulus per day. . . . .	24
2.9	AFM images of cantilever, PDMS microwells and the captured cell. <b>(a)</b> , <b>(c)</b> , <b>(e)</b> , <b>(g)</b> , <b>(i)</b> , and <b>(k)</b> are images of before pushing by the AFM cantilever and <b>(b)</b> , <b>(d)</b> , <b>(f)</b> , <b>(h)</b> , <b>(j)</b> , and <b>(l)</b> are images of after pushing. . . . .	26
2.10	Illustration of 3D schematic image of the simplest model of the SNT with single arm actuation. [74] . . . . .	28
2.11	Illustration of 3D schematic image of SNT. . . . .	30
2.12	Adjusted designs for cell measurement. . . . .	31
2.13	Schematic image of the comb teeth. . . . .	34
2.14	Distribution of the force at comb teeth. . . . .	36
2.15	SEM images of fabricated device. . . . .	37
2.16	Microfluidic device. <b>(a)</b> SNT tips are inserted to the channel from side opening. <b>(b)</b> Top view of fabricated microfluidic device. . . . .	38
2.17	<b>(a)</b> The channel was filled with a solution, e.g., PBS. <b>(b)</b> Then, tips were inserted via side opening. <b>(c)</b> After injection, a cell was captured and analyzed. . . . .	41
2.18	Microscope image of the captured cell by two SNT tips during the experiment. . . . .	42
2.19	The captured cancer cell. <b>(a)</b> The initial gap before compressing the cell and <b>(b)</b> the compressed state of the cell. . . . .	43
2.20	Given signal and responses during compression. <b>(a)</b> A linear displacement applied to the captured cell repeatedly (100 seconds periods). SNT were capable of detecting <b>(b)</b> resonance frequency and <b>(c)</b> sensor amplitude in real-time. . . . .	44
2.21	Applied compression cycle resulted in smaller response frequency changes for live SUM159PT cells (red) compared to fixed SUM159PT cells (green). A cell response deviated from no cell (blue) control result when the cells started to be compressed. . . . .	45

---

2.22	Detection of the diameter of the analyzed cell. . . . .	46
2.23	The difference of resonance frequency shift and normalized amplitude by changing the compression level. . . . .	47
2.24	Equivalent dynamic model of the SNT with the cell. . . . .	48
2.25	Measured stiffness at 10% compression was significantly different ( $p < 0.001$ ) between live (green) and fixed cells (red). No-cell condition as control experiments are also shown in same graph (blue). . . . .	49
2.26	Extracted <b>(a)</b> stiffness and <b>(b)</b> viscous losses from resonance characteristics in two different human breast cancer cell lines. . . . .	50
3.1	Schematic image of the proposed device with embedded microfluidic channel. .	54
3.2	Schematic view of a close-up view of the tips at the characterization part. <b>(a)</b> Placing a cell between tips by flow control. <b>(b)</b> Applying compression cycles to the captured cell by moving the tip. . . . .	56
3.3	Schematic view of the channel integrated MEMS device and polydimethylsiloxane (PDMS) cover alignment. . . . .	57
3.4	Schematic image of two different spring geometry. <b>(a)</b> U-shaped spring. <b>(b)</b> Double folded beam (DFB) spring. . . . .	58
3.5	Design of comb drive teeth. <b>(a)</b> Design for an U-shaped spring device. <b>(b)</b> Design for DFB (with long displacement) device. . . . .	59
3.6	Characteristics of actuation on various spring designs. . . . .	59
3.7	Differential capacitive sensor. The schematic image illustrates displacement sensing through $C_1$ and $C_2$ variation. . . . .	64
3.8	Scanning electron microscope (SEM) image of the <b>(a)</b> microfluidic channel around characterization part, and <b>(b)</b> embedded compression and sensing tips. . . . .	65
3.9	A close-up view of the microfluidic channel schematic image around characterization area. <b>(a)</b> Top view shows the attachment area between the PDMS cover and the MEMS device surface (in green). <b>(b)</b> The side view shows two different cross-sections: (i) Formed channel between the MEMS device and the PDMS cover is completely closed apart from (ii) the characterization area where removal of $\text{SiO}_2$ layer and the higher PDMS bottom surface allow movable parts of MEMS device to move freely. . . . .	66

3.10	SEM images of the fabricated device. <b>(a)</b> An overview of the device. <b>(b)</b> Displacement sensor based on differential capacitors. <b>(c)</b> Opposing tips accessing the characterization part. <b>(d)</b> Electrostatic comb drive actuators. <b>(e)</b> A close-up view of combs. . . . .	67
3.11	Photograph of experimental setup. . . . .	68
3.12	A close-up photograph of the channel integrated MEMS device and PDMS cover assembled on a printed circuit board (PCB) and installed in the setup. . . . .	69
3.13	Schematic view illustrating electrical connections of the device. . . . .	69
3.14	The channel filling protocol with liquid until tips part. <b>(a)</b> After assembling the PDMS cover on the MEMS device, the channel is formed. <b>(b) and (c)</b> The liquid is injected from the inlet and <b>(d)</b> adjusted the pressure with the pump, the liquid filled the channel. <b>(e)</b> The liquid reaches the opposing tips. . . . .	71
3.15	The channel filling protocol. <b>(a)</b> The liquid reaching the opposing tips and <b>(b)</b> going through the characterization part. <b>(c)</b> The channel completely filled with liquid. <b>(d)-(f)</b> Focus on tips. . . . .	71
3.16	The liquid exchange capability of the silicon device with water and a blue dye solution. <b>(a)</b> While the channel is filled with water, <b>(b) and (c)</b> a blue dye solution is injected from the inlet and within seconds <b>(d)</b> the liquid in the channel is completely replaced. . . . .	72
3.17	Frequency response of the device in different conditions showing the amplitude shift of the sensor readouts. . . . .	74
3.18	Frequency response of the device in different conditions showing the phase shift of the sensor readouts. . . . .	74
3.19	Real-time measurement of the device to examine the detection stability. Resonance frequency of the sensor readouts in 5 min. . . . .	75
3.20	Real-time measurement of the device to examine the detection stability. Amplitude shift of the sensor readouts in 5 min. . . . .	75
3.21	Resonance frequency of the system increased with increasing glucose concentration. . . . .	76
3.22	The amplitude of the system decreased with increasing glucose concentration. . . . .	77
3.23	Mechanical characteristics of glucose solutions with different concentrations in real-time. Resonance frequency increased with increasing glucose concentration. . . . .	77

3.24	Mechanical characteristics of glucose solutions with different concentrations in real-time. The amplitude decreased with increasing glucose concentration. . . .	78
3.25	The amplitude of the signal at 4 kHz in different conditions. . . . .	79
3.26	The amplitude of the signal during sweeping the frequency in different conditions.	79
3.27	The real-time measurements were performed at 1 kHz. Higher NaCl concentration resulted in a higher current which is detected as higher amplitude. . . . .	80
3.28	Average value of the real-time measurements show the relation between the NaCl concentration and the amplitude. . . . .	80
3.29	Sweeping the frequency provided the frequency response of the system. Note that the electrical measurements detected a small noise due to the mechanical measurements at around 600 Hz. The target frequency for the electrical measurements and the mechanical resonance frequency of the MEMS device should be designed carefully. . . . .	81
4.1	Low magnification image of the channel and the characterization area <b>(a)</b> , and sequential photos demonstrate single cell capturing <b>(b)-(e)</b> . <b>(a)</b> The channel and the characterization area. Only the channel part except around tips is closed with the PDMS cover. <b>(b)</b> Applying a potential difference between the compressing actuator electrodes narrows the gap between the tips. <b>(c)</b> The solution is kept flowing until a cell arrives at the handling area. <b>(d)</b> Then, the flow rate and the potential difference between the compressing actuator electrodes are decreased until the cell is positioned between the tips. <b>(e)</b> Finally, the flow is completely stopped and cell compression is performed. . . . .	84
4.2	The cell compression cycles. <b>(a)</b> Voltage cycles applies to electrostatic combs in the compression side for compressing the captured cell, and <b>(b)</b> Displacement of the compression tip. The tip moves over 7 $\mu\text{m}$ with applied voltage of 85 V. . .	85
4.3	Frequency response in real-time. <b>(a)</b> Applied compression cycles resulted in resonance frequency changes (in red). No cell control (in blue) was also shown in same graph, and <b>(b)</b> Applied compression cycles resulted in amplitude shift (in red). . . . .	86
4.4	Real-time responses of the cell. <b>(a)</b> Stiffness, and <b>(b)</b> Viscous losses of the captured cell. . . . .	86

---

4.5	Presented compression cycles using the cell compression level. <b>(a)</b> Resonance frequency shift, and <b>(b)</b> Signal amplitude shift. . . . .	87
4.6	Mechanical properties of seven different SUM159PT cells during the compression. <b>(a)</b> Resonance frequency, <b>(b)</b> Signal amplitude shift, <b>(c)</b> Stiffness, and <b>(d)</b> Viscous losses. . . . .	88
4.7	Delay in the data acquisition. Resonance frequency shift (in red) and displacement of compression tip (in black) were shown. . . . .	90
4.8	<b>(a)</b> Square root voltage cycles applies to comb drive actuator on compression side, and <b>(b)</b> Displacement of the compression tip. . . . .	91
4.9	Cell responses of the captured cell in real-time while applying cell compression cycles. <b>(a)</b> Resonance frequency shift, and <b>(b)</b> Signal amplitude shift. . . . .	91
4.10	After correction of data acquisition time. Resonance frequency shift (in red) and displacement of compression tip (in black) were shown. . . . .	92
4.11	Compared two different duration time (10s: in purple, 30s: in pink) by the compression level. <b>(a)</b> Resonance frequency shift, and <b>(b)</b> Signal amplitude shift. . . . .	92
4.12	Mechanical properties of the captured cell compared two different duration time (10 seconds: in purple, 30 seconds: in pink). <b>(a)</b> Stiffness, and <b>(b)</b> Viscous losses. . . . .	93
4.13	Mechanical properties of seven different MCF7 cells during the compression in real-time. <b>(a)</b> Resonance frequency shift, <b>(b)</b> Amplitude shift, <b>(c)</b> Stiffness, and <b>(d)</b> Viscous losses. . . . .	94
4.14	Electrical measurements performed on a cell in PBS solution (red line) and control (no cell in PBS, blue line). Electrical characteristics of the setup (in air) are shown in grey line. . . . .	96
4.15	Comparison between fixed SUM159PT and MCF7 cells extracted at 10 % of the cell compression level. <b>(a)</b> Stiffness, and <b>(b)</b> Viscous losses of the analyzed cell. . . . .	97
4.16	Comparison the extracted stiffness of fixed SUM159PT cells from 10 % of the cell compression level between <b>(a)</b> SNT, and <b>(b)</b> the channel integrated MEMS device. . . . .	98
5.1	Fabricated the L-shaped compression tip for easier capturing the cell. . . . .	106

---

A.1 Schematic diagram of PDMS microwell fabrication process using SU-8 mold. <b>(a)</b> Cleaning of Si wafer. <b>(b)</b> Spin coating SU-8 photoresist. <b>(c)</b> UV-light exposure through the photomask. <b>(d)</b> Developing the SU-8 to make needed patterns. <b>(e)</b> Pouring PDMS and curing on a hotplate. <b>(f)</b> Peeling off the PDMS from the SU-8 mould. . . . .	119
--	-----

# List of tables

2.1	Design of mechanical suspensions . . . . .	33
2.2	Mass calculation of SNT movable part . . . . .	48
3.1	Main parameters of device designs . . . . .	58
3.2	Details of folded beam spring in sensing part . . . . .	62
3.3	Dimension of the capacitive sensor . . . . .	63
4.1	Cell compression conditions applied to seven different SUM159PT cells . . . . .	88
4.2	Measured cell size of SUM159PT . . . . .	89
4.3	Conditions of the cell compression for providing seven different MCF7 cells . . . . .	95
4.4	Measured cell size of MCF7 . . . . .	95
D.1	Fabrication process of SNT (No.1) . . . . .	126
D.2	Fabrication process of SNT (No.2) . . . . .	127
D.3	Fabrication process of SNT (No.3) . . . . .	128
D.4	Fabrication process of SNT (No.4) . . . . .	129
E.1	Fabrication process of the channel integrated MEMS device (No.1) . . . . .	133
E.2	Fabrication process of the channel integrated MEMS device (No.2) . . . . .	134
E.3	Fabrication process of the channel integrated MEMS device (No.3) . . . . .	135
E.4	Fabrication process of the channel integrated MEMS device (No.4) . . . . .	136
E.5	Fabrication process of PDMS cover . . . . .	138

# Symbols

## Roman Symbols

$a$	radius of contact circle
$C_0$	center electrode of capacitive sensor of SNT
$C_1, C_2$	capacitive sensor electrodes of SNT
$C_{\text{total}}$	capacitance of movable electrode
$F$	tip load
$E$	apparent Young's modulus
$f_R$	resonance frequency
$F_x$	actuation force in $x$ -direction
$g$	gap between the opposite combs teeth
$k_{\text{cell}}$	stiffness of the cell
$k_L$	total spring stiffness in compression side
$k_l$	one beam of spring stiffness in compression side
$k_R$	total spring stiffness in sensing side
$k_r$	one beam of spring stiffness in sensing side
$L$	length
$M$	total mass of movable part



---

$n$	total number of comb teeth
$Q$	quality factor
$R_s$	radius of sphere mounted on AFM cantilever
$t$	thickness of wafer
$V$	potential difference, applied voltage
$w$	width

**Greek Symbols**

$\delta$	cantilever indentation
$\Delta C$	difference between $C_1$ and $C_2$
$\Delta x$	displacement of compression tip
$\epsilon_0$	vacuum permittivity: $8.854 \times 10^{-12}$ [F/m]
$\eta_{cell}$	viscous losses of the cell
$\nu$	Poisson's ratio

**Acronyms / Abbreviations**

AC	Alternating Current
AFM	Atomic Force Microscopy
Al	Aluminium
ALDH	Aldehyde dehydrogenase
BioMEMS	Bio-medical MEMS
BOX	Buried Oxide
CAGR	Compound Annual Growth Rate
CCD camera	Charged Coupled Device camera

---

CSC	Cancer Stem Cells
CTC	Circulating Tumour Cells
DC	Deformability Cytometry
DC	Direct Current
DEAB	Diethylaminobenzaldehyde
DFB	Double Folded Beam
DFB-L	Double Folded Beam with long teeth
DNA	Deoxyribonucleic Acid
DRIE	Deep Reactive Ion Etching
HF	Hydrofluoric Acid
IC	Integrated Circuit
MA	Micropipette Aspiration
MEMS	Micro Electro Mechanical Systems
micro-TAS	Micro-Total-Analysis Systems
MS	Microplate Stretch
MTC	Magnetic Twisting Cytometry
non-CSC	non Cancer Stem Cells
OT	Optical Tweezers
PBS	Phosphate-Buffered Saline
PCB	Printed Circuit Board
PDMS	Polydimethylsiloxane
PFA	Paraformaldehyde

PLL Phase Lock Loop

RF Radio Frequency

SEM Scanning Electron Microscopy

SiO<sub>2</sub> silicon dioxide

Si Silicon

SNT Silicon NanoTweezers

SOI Silicon on Insulator

# Chapter 1

## Introduction to BioMEMS

### 1.1 Introduction

The purpose of this study is to develop and realize a MEMS device with integrated microfluidic channel for the measurement of various biophysical parameters of single cells in suspended state. With this device, the biophysical characteristics of a cell can be used to identify cancer cells from other populations in a sample solution.

#### 1.1.1 Cancer and cell biomechanics

Taking globally, cancers cause the greatest number of deaths in the world. The total mortality rate of cancer has increased all over the world [1],[2]. It was estimated that the number of cancer deaths in 2012 had reached 8.2 million [1]. In 2018, total number of cancer deaths in the EU alone are predicted to reach approximately 1.4 million [2]. However, behind the word "**Cancer**" are hidden an increasing number of sub-diseases and not a single one. Interestingly, early diagnosis and treatment, the prognosis for cancer patients can be significantly improved independently of cancer subtype. When cancer remains localised at the point of tumorigenesis, without invading the original organ, so called "*in situ* tumors", patients have a higher chance of survival using surgery and other complementary techniques such as chemotherapy or radiotherapy. The main cause of cancer death is due to primary tumor undergoing tissue invasion and *in fine* "**metastasis**" wherein cancer cells spread through the organism and find niches to grow into distant tissues and organs beyond where the tumor originated. The formation of these new tumors (secondary and tertiary foci) results in the death of 90 % of patients with cancer. So, understanding metastatic development from circulating tumor cells is a critical area of cancer research.

Cancers are complex diseases. Most of them rise from abnormal disequilibrium between cell growth and cell death. Nowadays, cancers are known to develop from DNA mutations and/or epigenetic modifications happening through the life of the cells. DNA carries gene information unbending code from nucleotides sequences (A: Adenosine, T: Thymine, G: Guanine, C: Cytosine) which through transcription and translation allow the production of functional elements of the cells: the proteins. Some of these proteins are enzymes (ATPase, Pyruvate Dehydrogenase), cell signalling proteins (ERK, AKT, PTEN), structural proteins (Actin, Tubulin) or growth factors (EGF, HGF). Interestingly, most of DNA mutation involved in cancer development have been identified to be involved in cell growth control, as p53, PTEN, RAS... etc... The modifications of cell signalling induce a global disequilibrium pushing forward to an intensive cell growth. Accumulation of these mutations could come from random errors induced by miss function of DNA replicative machinery or extrinsic factors as tobacco, ultraviolet rays, radiation or other carcinogens. It is usually a combination of these abnormalities that leads to a cancerous cell.

There are many differences between cancer cells and their normal counterpart cells. Some of the differences are well known, whereas others are less understood and have been discovered only recently. Such distinction could lay the foundation for the development of treatments designed to rid the body of cancer cells with little if not damages to normal tissues. As an example, some breast cancer sub-type overexpress the membrane receptor HER. Interestingly, this overexpression has been used as an opportunity to target specifically cancer cells. For this research was developed an humanised antibody which is now prescribed routinely in clinic: Herceptin.

To our concern, the major factor shaping the metastatic character of cancer cells lies in their motility. The development and progression of cell motility is orchestrated by a sequence of specific biophysical, interdependent processes involving cytoskeletal modifications, changes in cell-substrate adhesive properties and alterations in the extracellular matrix. Loss of epithelial characteristics and gain of a migratory phenotype such as mesenchymal phenotype provides one of the major characteristics of disease step. As mesenchymal-like cells which has morphology of elongated migrating cells, epithelial cancer cells can acquire mesenchymal traits with increased motility/migration and invasive capacity which makes them more likely to generate Circulating Tumour Cells (CTC) which defined as the cell that has shed from a primary tumour or metastatic tumour into the blood vasculature or lymphatics, to cause cancer spreading and grow distant metastasis. This phenomenon in which epithelial cells acquire mesenchymal traits is so called

the Epithelial-to-Mesenchymal Transition (EMT) [3]. Interestingly the process of EMT can be reverted through MET (Mesenchymal-to-Epithelial (re-)Transition) [4], which could be involved in metastasis take-off. Specific pathway involved in this transition have been identified, as SNAIL and SLUG, and associated with metastasis development and poor patient outcome [5],[6].

Among these genes, genes coding proteins building the cytoskeleton are crucial to acquire migration features. The cytoskeleton forms the structural framework of the cell. It is a complex structure, highly ordered intricate polymers network. It is composed of filamentous structures such as actin fibers, microtubules and intermediate filaments. The cytoskeleton mainly determines the shape of the cell by providing mechanical rigidity (reversible deformability of the cell), but it is also involved in many cell processes and functions as vesicle translocations. More importantly, cytoskeleton is required for cell adhesion and cell motility involving the movement of cells from one location to another during embryonic development, inflammation or metastasis, as well as separation of a cell into two daughter cells during cell division. Also, the specific characteristics of the cytoskeleton serve to enable various functionalities in differentiated cell types, as long vesicle transportation along neural axon or tight junction in intestinal epithelium. As consequently, diseases affecting cellular processes as carcinogenesis and more specifically EMT induce intracellular network changes and are reflected in the cytoskeleton.

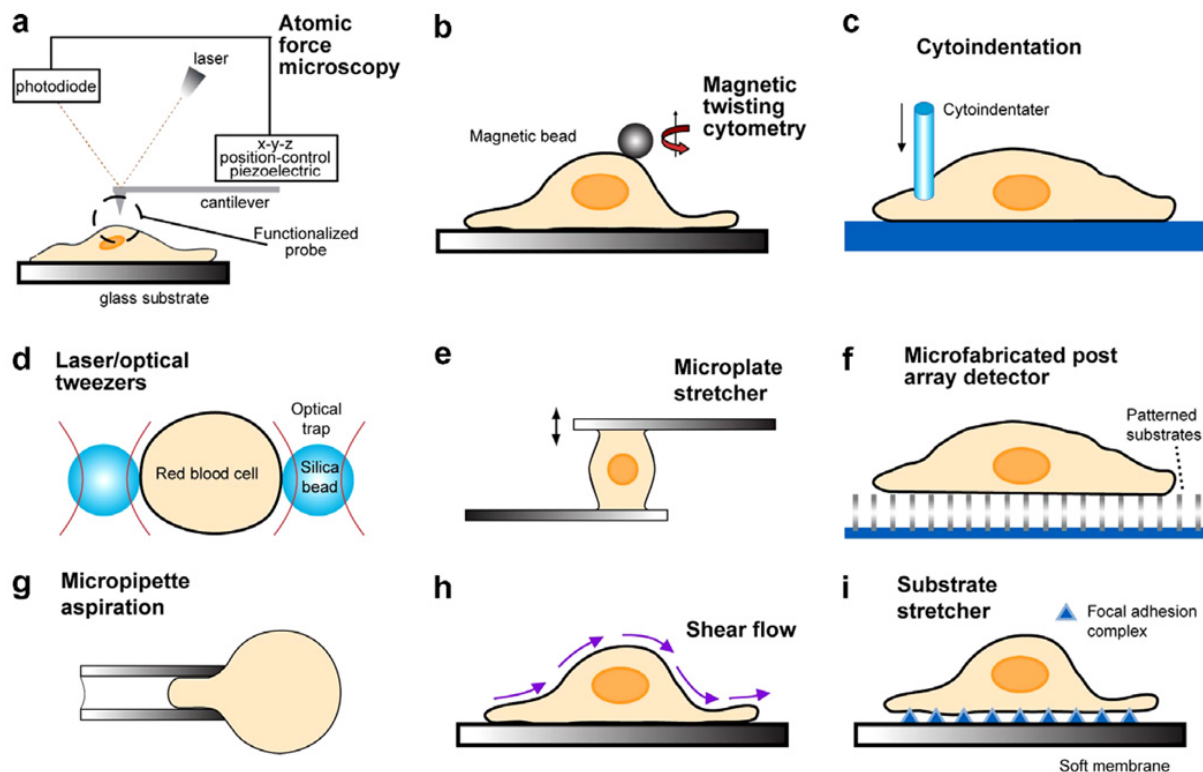
When cancer cells escape the primary tumor, three primary routes are possible: - locally (regionally), - through the bloodstream, - through the lymphatic system. cancer cells can pass through narrow spaces like the endothelial walls of blood vessel which can be as small as 1  $\mu\text{m}$  [7]. EMT leads to a change in intracellular structures that allow cells to adapt to acquire this potential. In other words, the deformability of the cell can reveal important information due to the change in the cell network and this can be used as an important biomarker of its metastatic potential. Deformability of the cell which is the stiffness of the cell can be also indicate the cell type. This offers new predictive opportunities for the metastatic potential of the cell and can serve as a new target for diagnosis. Understanding cell behaviour during metastasis would be a major breakthrough to identify and prevent metastasis development.

### **1.1.2 Previous research on cells characterisation**

Given that diseased and healthy cells often exhibit differences in their cellular structures, it has been proposed that an analysis of that structure could be used to identify and differentiate those

cell types [8],[9]. In other words, testing the deformability of cells can potentially be used to diagnose the presence of diseased cells within a population.

There are various techniques that have been used to characterise cancer cells. Some examples of single cell measurement techniques are shown in **Fig. 1.1** [10] and also briefly described below.



**Fig. 1.1** Schematic images of the biomechanics techniques used to probe subcellular regions are given in (a)-(c). Techniques used to probe the deformation of single cells are given in (d)-(g). Techniques used to infer cytoadherence, deformation and mobility characteristics of populations of cells are schematically sketched in (h) and (i). [10]

### (1) Micropipette Aspiration

Micropipette Aspiration (MA) is a widely applied method for studying cortical tension and deformability. Based on simple hydrostatic principles, this assay allows the application of a specific magnitude of mechanical stress to the cell surface. A small diameter glass pipette is brought into contact with cells and a known suction pressure is then applied within the pipette. This causes the aspiration of cells into the glass pipette while tracking

the leading edge of its surface. This method have revealed insights about cell mechanics and mechanosensing and compared many types of cells.

The elasticity of malignantly transformed fibroblasts was reduced about 50 % compared with the normal counterpart [11]–[16].

### (2) **Atomic Force Microscopy**

Atomic Force Microscopy (AFM) [17], a commercially available scanning probe microscopy technique, is the most established method with a super high resolution in the order of nanometer scale and can measure a force spectroscopy and a topography of a sample surface. It does not suffer from a limitation in spatial resolution because the AFM bases on measurements of a laser deflection from a micron scale probe fixed to the cantilever. The probe is made of silicon or silicon nitride, with a tip radius of curvature on the order of nanometers. AFM can measure living cells without special staining steps or fixation but samples have to adhere to a substrate. The AFM cantilever moves at constant velocity and senses forces acting between the cantilever tip and the sample surface. For the measurements of the mechanical properties (cell rigidity) [18]-[40], the cantilever indents the sample surface at a given position. The force produced by the AFM, which is in the order of piconewtons (pN) to micronewtons ( $\mu\text{N}$ ), is applied to the sample surface and the recorded cantilever deflection contains the information on the sample stiffness.

Normal human bladder endothelial cell lines and complimentary cancerous cell lines were compared and found that they were different by an order of magnitude in rigidity[29]. Also, within the same sample, the stiffness of metastatic cancer cells from breast cancer patients was shown to be more than 70 % softer (deformable) than the benign cells that line the body cavity [23].

### (3) **Deformability Cytometry**

Deformability Cytometry (DC) is one of the important hydrodynamic approaches and it uses the technique of the cell deformation by deceleration at the stagnation point of fast extensional flow [41]. A cell is brought to the point by flow and its deformation is recorded with a high-speed camera. DC enables rapid mechanical phenotyping of single suspended cells at sampling rates of  $\sim 1,000$  cells/sec with throughput that is comparable to conventional fluorescence-based flow cytometry [42]. Please note that other general



techniques including AFM have throughput rates of 10-100 cells/h is far too low for biology applications.

However, owing to the massive amount of data generated, the total number of cells analyzed is limited to a few thousand.

Over 3,000 single cell biophysical measurements per specimen were obtained from benign or malignant pleural effusions in 119 patients. Metastatic cancer cells showed to exhibit lower resistance to deformation [43].

Additionally, techniques include Magnetic Twisting Cytometry (MTC) [44], microneedle probe [45], mechanical Microplate Stretch (MS) [46], and manipulation of beads attached to cells using laser/Optical Tweezers (OT) [47]-[49], and so on. In addition to the above methods, a wide variety of methods have been used to assess mechanical deformability of biological cells.

However, there are some restrictions of those method. For example: (1) The requirements of samples attachment techniques in each method are different, especially, DC requires to detach cells for making suspension state, (2) Many of them are time-dependent and operate in different systems of spatial resolution, (3) They also involve diverse levels of complexity requiring high operation skills to use the instrument, and (4) The cell sampling rates (throughput) are too low to screen relevant populations compared with biological or medical fields (over 10,000 cells). Ideal techniques should match to this requirements of a target biological sample.

However, from these studies, it was found that metastatic cancer cells are either flexible or less viscous (less resistant to flow) to applied stress in the experiment, reflecting the request for metastatic cancer cells to squeeze through the degraded matrix of the surrounding tissues and enter the circulating system to establish a distant tumor site [50]-[55]. Based on these observations, we made the hypothesis that cell mechanical characteristics has a potential to be used as a biomarker to identify cancer cell with high metastatic potential, without using any special staining steps (label-free biomarker) . Thus, measuring mechanical properties of single cancer cells without a high throughput device is crucial.

Micro Electro Mechanical Systems has been introduced as a new technique to study the biomechanics of the cell. Using the benefits of microtechnologies, a MEMS-based method can lead to early diagnosis and also to understand the underlying mechanism of metastasis.

### 1.1.3 Advancement of MEMS

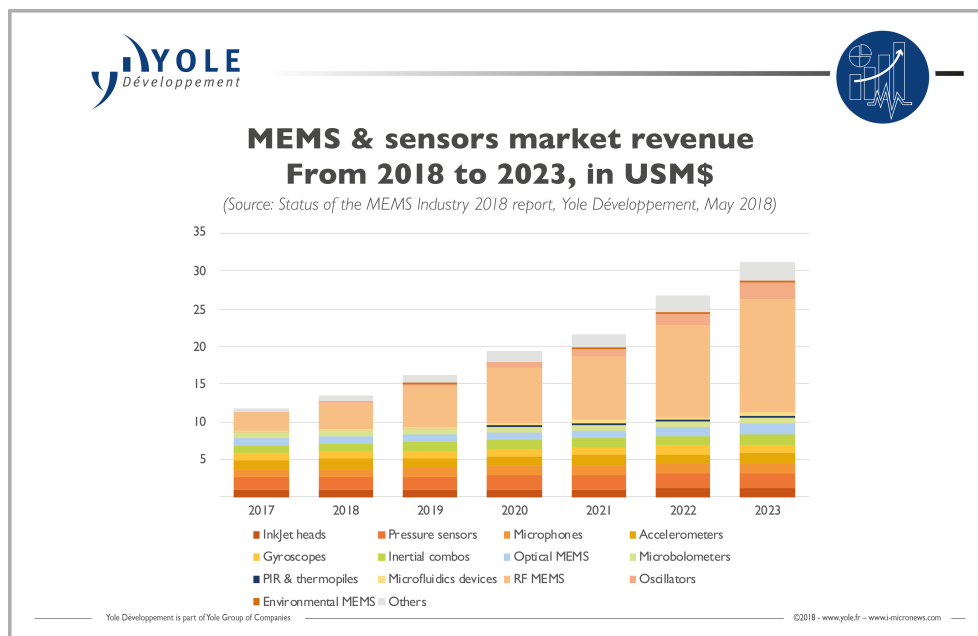
In recent years, micromechatronics has attracted a lot of attention [56]. It is a field which has been existing for more than 50 years, with several applications achieving commercial and/or scientific success. Microsystems with sub-micrometer dimensions can perform minute movements and operations on the order of nanometers to micrometers and can handle small or similarly-sized objects. Microsystems fabrication methods include conventional machining techniques and specialised micro-machining techniques, however, it is difficult to mass-produce, fabricate and assemble complicated structures with conventional machining techniques [57]. Since a few years, fabricating microsystems with a size of tens of micrometers on a silicon substrate became more efficient using micromachining techniques based-on semiconductor microfabrication technology, and so Micro Electro Mechanical Systems (MEMS) have been rapidly developed [58]. Furthermore, MEMS can combine multiple distinct functionalities into a single device. Examples of these more advanced microsystems include digital-micromirror-devices which are commonly used in projectors as well as biological micro-total-analysis systems (micro-TAS) devices incorporating the various capabilities of a laboratory onto a single chip (lab-on-a-chip). Using semiconductor microfabrication technology, microstructures can be fabricated with submicron accuracy and in massive numbers.

MEMS techniques were originally developed in the microelectronics industry. Traditionally, MEMS have been used to produce functional devices at the micrometer scale such as sensors, actuators, switches, filters, accelerometers, and gears. Such devices are primarily made from silicon, the dominant material used throughout the integrated circuit (IC) industry. MEMS are currently used in automobiles, aerospace technology, biomedical applications, ink jet printers, wireless and optical communications in our daily lives. New applications are emerging every day and improving the performance of individual MEMS devices makes dramatic progress every year.

### 1.1.4 Bio-medical applications of MEMS

MEMS market will experience a 17.5 % growth in value at Compound Annual Growth Rate (CAGR) between 2018 and 2023, to reach US\$ 31 billion at the end of the period [59]. The Radio Frequency (RF) industry plays a key role in the MEMS industry development, as shown in **Fig. 1.2**. RF filters in 4G/5G are making RF MEMS (mainly Bulk Acoustic Wave filters)

the largest-growing MEMS segment. **Bio-medical MEMS (BioMEMS)** refers to MEMS in bio related fields including MEMS devices for applications in medical micro devices and biomedical research such as an inspection kit for body fluid/ odour sensors for diagnostic and preventive medical treatment at home. Similarly, development of inspection and evaluation techniques using MEMS for physical manipulation of small objects such as cell or biomolecules is accelerating of the bionanotechnology research. It offers various benefits such as improvements in medical device performance for patients. Based on these factors, the market size of BioMEMS has been increased. In 2014, a value of US\$ 2.5 billion was estimated and a growth at CAGR of over 25 % is anticipated from 2016 to 2023 [60].



**Fig. 1.2** MEMS and sensors market revenue from 2018 to 2023 (y-axis is USB\$) [59].

MEMS in bionanotechnology fields have various benefits:

### (1) **Integration**

Integration of devices with various functions can be realized. Complex structures such as electrical circuits, sensors, microfluidic channels and reaction vessels can be integrated on one substrate. It is possible to obtain multiple functions and high-level performances that cannot be attained on a single device using conventional approach. This leads to faster interaction with biological samples providing various characterization functions in a much smaller space.

### (2) **Miniaturization**

Systems with micron scale dimensions can be realized. The miniaturization is a key feature for cellular biology to provide devices matching the size of a cell. When measuring physical or chemical quantities, smaller dimensions provide information with higher accuracy and sensitivity. Moreover, only a small amount of sample is required in a chemical reaction.

### (3) **Mass production**

Using the semiconductor process, a large number of devices can be fabricated at once. A small amount of force/energy are used compared to macro scale.

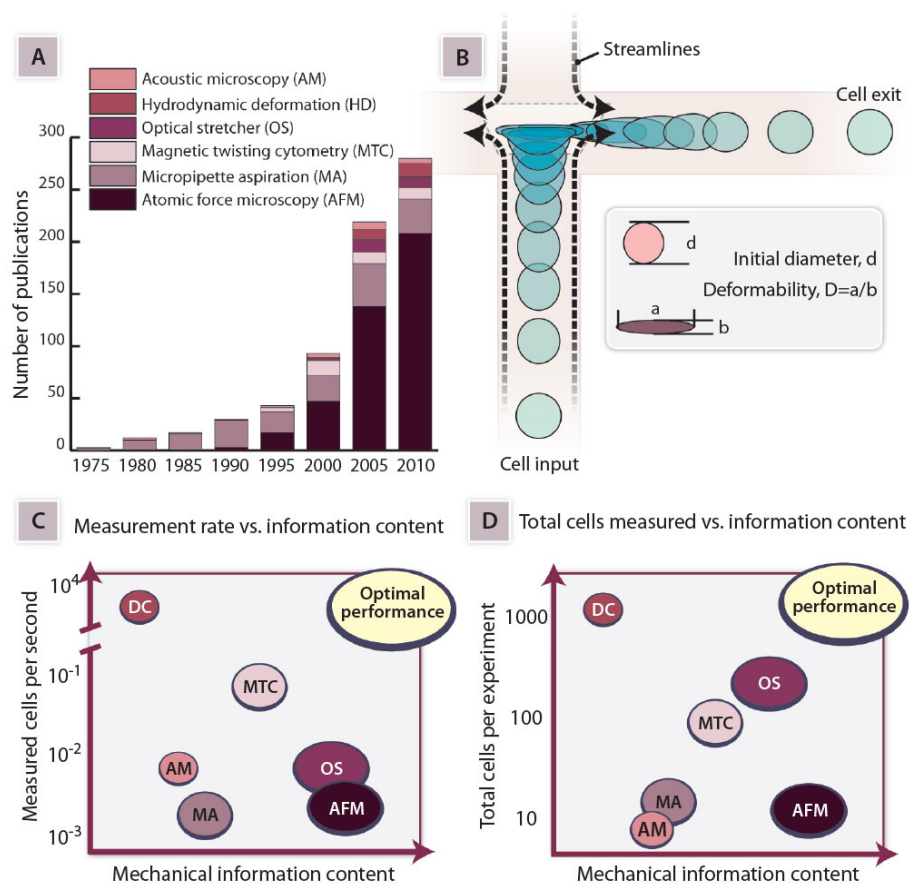
For the above reasons, MEMS is suitable for the biotechnology field. Complex MEMS tools become easily accessible by many researchers and enable them to obtain multiple parameters simultaneously from individual cells.

The ability of MEMS to design and control experiments at the micrometer scale has attracted the interest of biologists, who have started devising fundamental studies using this technology [61]. MEMS technology has been applied to the successful development of a variety of health care related products and has enabled the development of miniaturized diagnostic tools and high throughput screening assays for drug discovery and tissue engineering [62],[63]. Moreover, research on BioMEMS, particularly in diagnostics, has rapidly expanded in recent years, such as the fields of oral drug delivery systems [64], microneedle systems [65], organ-on-a-chip [66],[67] and body-on-a-chip [68] for physiologically relevant three-dimensional (3D) in vitro modeling.

## **1.2 Purpose and significance of this study**

It is crucial to characterise cells at the single cell level and MEMS technology allows getting important information about conditions of cells such as being benign/malignant with their metastatic potential and identify/sort a type of the single living cell population. The commonly used methods described in **Subsubsection 1.1.2** all suffer from various restrictions. For example, AFM can be applied to study adherent cells but not suitable for analysing non-adherent cells (cells in suspension, e.g., CTC) because cells must be immobilized during measurements. Also, AFM enables measurements with high spatial resolution at nanometers scale but it suffers from low throughput due to the necessary time for force measurements, calibration steps, and sample preparation/handling. The measurement speed is the key factor as more parameters have to

be characterised for a massive number of cells. In contrast to AFM, the microfluidic-based method, such as DC, suits better for characterising the mechanical properties of suspended cells and provides rapid measurements over 1,000 cells/sec similar to the conventional fluorescence-assisted cell sorting. However, the information contents obtained with DC measurements is limited to only one parameter, (e.g., deformability) due to the resolution of the optical detection [41]-[43],[69]-[72]. Thus, there is a trade-off between throughput and obtained information content, as shown in **Fig. 1.3** [73].



**Fig. 1.3** Measuring cell mechanics [73]. **(A)** An apparently exponential increase in cell mechanics publications over the past two decades, sorted by measurement technique. DC falls under the category of hydrodynamic deformation, or HD. **(B)** Image of the HD technique applied by Tse et al. [43]. **(C)** Schematic image of the trade-off between cell-sampling rate and information content of the different techniques. **(D)** Schematic image of the trade-off between cells measured and information content of the different techniques.

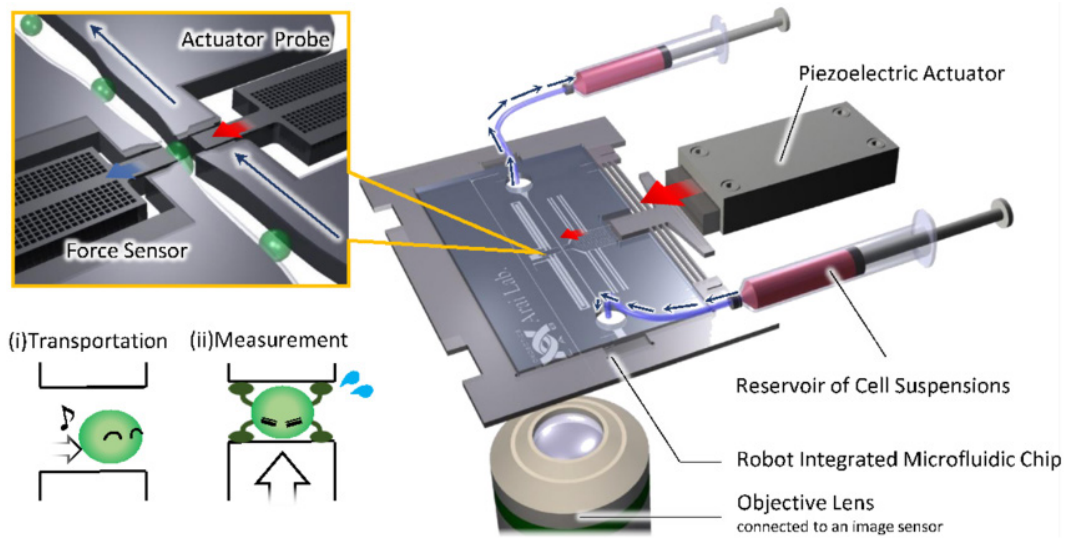
Using biophysical properties to identify cells in a sample solution for practical routine tests require high performance in both aspects: **high-throughput (sampling rates)** and **high information content (multi-parameter measurements with high detection sensitivity)**. BioMEMS

technology is the key to measure and characterize multiple-parameters of cells. In order to increase the throughput combining MEMS technology with microfluidics may pave the way to the development the technique to characterise biophysical properties of cells by overcoming the challenging trade-off.

Silicon NanoTweezer (SNT) [74]-[75], developed in Prof. Hiroyuki Fujita's laboratory, Institute of Industrial Science (IIS), The University of Tokyo [78], is an example of MEMS devices integrated with a microfluidic chip. It can perform continuous measurements of a cell's response in real-time. Owing to a flow in the microfluidic chip, suspended single cells are brought to the characterisation area of the SNT. The SNT can handle and/or characterise biological samples such as microtubules [76], DNA [77]-[79], and cells [82]-[84], even for clinical purposes [85],[86]. However, single cell characterisation with the SNT requires alignment of the MEMS device with the microfluidic chip; tips of the tweezers are positioned at the sub-mm-size opening in a microfluidic channel and inserted in the water meniscus for a few tens of micrometers. Therefore, demonstrated lateral direction approach of an SNT to the microfluidic channel side-entrance [76],[77] does not provide a very high cell trapping efficiency.

A similar system for cell characterization based on microfluidics integrated with a single cell detection device has been demonstrated recently (**Fig. 1.4**) [88]-[92]. Even though this system successfully implemented the phase detection of moiré fringe as a high resolution displacement sensing which has a resolution of tens nanometers scale while acquiring the benefit of microfluidics, it requires an external actuation unit (a piezoelectric actuator) and the optical detection (CCD camera attached to the microscopy) that may prevent it from routine tests. According to this proposed measurement method, the mechanical properties of cells in suspended state could be measured. However, the throughput and measurement performance still need to be improved. The way to transport the cell is not reached enough with required levels to obtain statistically significant amount of data in a short time. They used the liquid flow [88] or an external optical tweezers [92] for bringing the cell to the characterization area. It is necessary to develop an automated system, including accurate flow control.

Due to the aforementioned points, the purpose of the study is to develop and realise a novel MEMS device with integrated microfluidics for multi-parameter measurements of single cells in suspended state. The aims to develop a novel MEMS device for single cell characterization



**Fig. 1.4** Overview of the on-chip measurement system for cellular mechanical characteristics [88].

and MEMS can integrate various functions on chip to measure multiple parameters. This thesis investigate possible parameters suitable for distinguishing cells for a label-free detection method.

According to the proposed method, suspended cells will be flowing in the microfluidic channel embedded in the MEMS device to reach the characterization area. Two tips, inserted in to the channel from both sides of the channel, will be used for capturing and characterizing single cells. One of the tips will be compressing a cell while the other one performs mechanical and electrical measurements in real-time.

To sum up, the main goal of this study is to develop a practical high-throughput method for single cell biophysical characterisation to distinguish circulating cancer cells in a label-free format.

## 1.3 Organization of thesis

This thesis is divided into 5 chapters. After a brief introduction of **Chapter 1: Introduction to BioMEMS**, presented here, each chapter follows as summarized below:

## **Chapter 2: A proof of concept for MEMS based single cell biophysical characterization**

In order to identify the cell state such as cancerous or healthy by cell mechanical properties, the gold standard (reference standard) is using AFM as a well established and commonly used method. Since AFM corresponds to adherent cells spread on the substrate, the AFM measuring system has to be modified to measure the floating cells targeted in this study. PDMS microwells were used to hold floating cells during the AFM cantilever indentation. Also, similar mechanical measurements were performed by the SNT combined with microfluidic devices. To find possible parameters that can be used as a biomarker for identifying cells and also to test the required detection sensitivity, mechanical measurements of single suspended cells was first done with SNT. The results were used for the developed device described in the following chapter.

## **Chapter 3: Development of a built-in channel device for single cell biophysical characterisation**

A novel MEMS device with integrated microfluidic channel was proposed for the high-throughput measurement of various parameters of single suspended cells. All necessary components such as electrostatic combs actuators, differential capacitive sensor, cell handling tips and microfluidic channel were integrated in one unit. The built-in channel device applied optimal parameters obtained by SNT in previous chapter. A PDMS layer on top was used for covering the entire device. The device was tested for several tasks: liquid replacement test for confirming the flow inside the microfluidic channel, glucose solution titration test to investigate mechanical viscosity detection and NaCl solution titration test to examine the electrical conductivity detection.

## **Chapter 4: Cell biophysical characterisation with a built-in channel device**

In this chapter, actual suspended single cells experiments were carried out using the proposed device. Two different breast cancer cell lines, SUM159PT and MCF7, were prepared for the experiment. They were fixed by Paraformaldehyde (PFA) to keep stable conditions for long time. Each cell line has different characteristics based on their metastatic properties. A capturing protocol for handling and characterising single suspended cells at the cell characterisation area was established. Stiffness and viscous losses of the captured cell were compared between two



cell lines. The electrical characterization of a cell line was also demonstrated by comparing the conditions of in the air and in the PBS solution.

The last **Chapter 5: Conclusions and future work** gives the conclusions and draws some recommendations of future work with especially the device characterization.

Moreover, **Appendices** of this work include some supplementations about the microfabrication of the MEMS device (Silicon NanoTweezers and a built-in channel MEMS).

# Chapter 2

## A proof of concept for MEMS based single cell biophysical characterization

### 2.1 Introduction

As previously described, cell heterogeneity could be distinguished based on their physical characteristics. The main goal of this chapter is to find appropriate properties of cancer cells for distinguishing non cancer stem cells (non-CSC) from cancer stem cells (CSC), or circulating tumour cells (CTC) from healthy blood cells. Distinguishing the last population will be the highest challenge due to their frequency, as low as a few cells per millions of blood cells. At first, AFM measurements will be used as the gold standard (reference standard) of the field to analysis non-CSC and CSC physical properties (In **Section 2.2**). AFM is a well-established technology to measure physical properties of cells (elasticity of the sample and topography imaging). From this point of view, it is used to validate the concept of using physical characteristics to classify cancer cells. However, using AFM protocol requires extensive adaptation to fit with circulating cell conditions. The main limitation of the AFM technology is it's laborious and time-consuming process. In order to increase analysis efficiency, another approach is taken: applying MEMS device for mechanical characterization of cells and ultimately combining such MEMS with a microfluidic device. In **Section 2.3**, the application of a Silicon NanoTweezers (SNT) to measure mechanical and electrical properties of cells in suspension is described.

## **2.2 Applied AFM as the conventional method to floating cells measurements**

### **2.2.1 Background of AFM measurements**

It is known that the physical properties of cells change in common human diseases such as cancer, asthma, malaria, and cardiovascular disorders [9],[96],[97]. Alternations of physical (mechanical and/or electrical) properties of cells can be effectively utilized for early detection, drug discovery, and drug efficiency tests [98]. To measure the mechanical properties of cells, many techniques have been developed including micro-pipette aspiration [11]-[16], magnetic bead rheometry [44], optical tweezers [47]-[49] and atomic force microscopy (AFM) [18]-[40]. Many of these techniques require the direct contact between cells and probes, and/or adhesion of cells to a substrate. Also, these measurement operations are manually performed, and artificial factors lead to an increase in variation of measurement and a decrease in reproducibility.

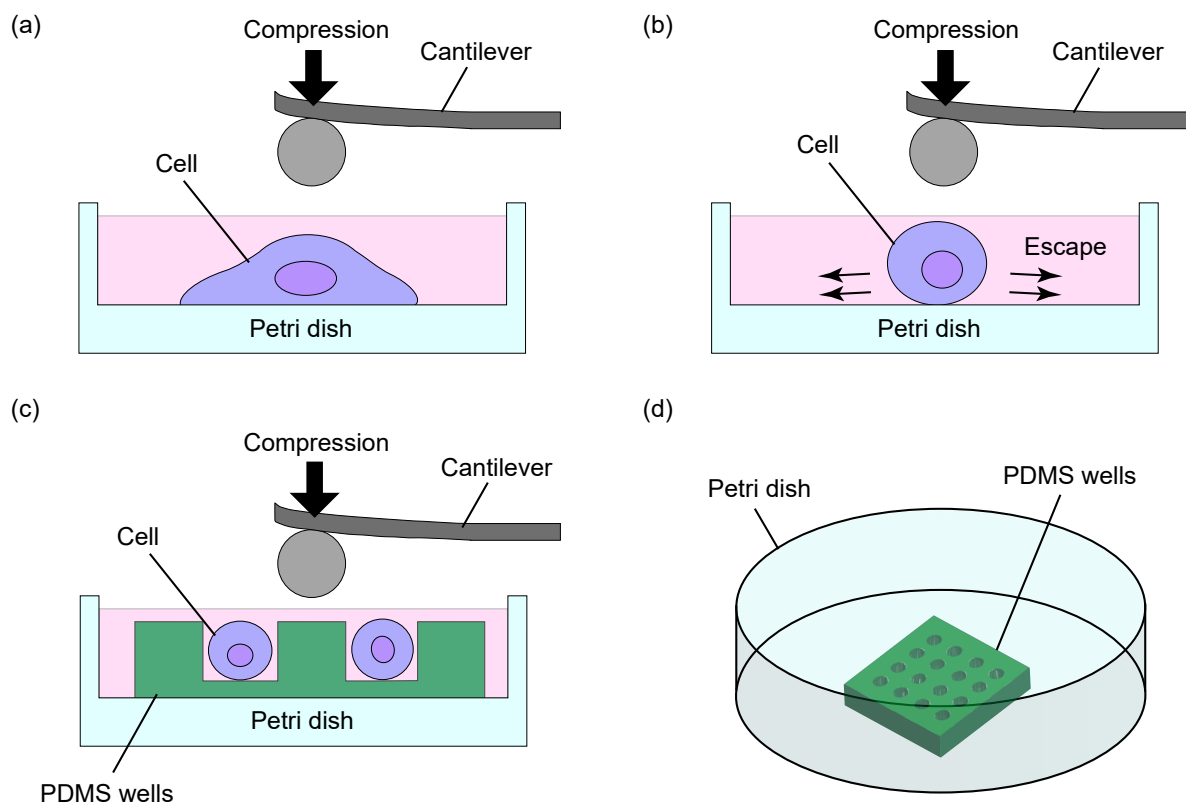
AFM is widely used to measure physical properties of cells for studying single cell biomechanics. It has been established as a general tool for imaging and measuring elastic properties of living cells. The mechanical properties of adherent cells can be tested in different geometries by following cell adhesion using AFM. The previous AFM studies investigated the mechanical properties of cancer cells obtained from cancer patients. The comparison was performed between the elasticity of normal human cells and cancerous ones by applying AFM indentation to the cell. From these results, normal cells were found to be much stiffer than cancer cells. However, these traditional techniques suffer from low measurement throughput of 10 ~100 cells/day.

### **2.2.2 Adapting AFM experiments to non-adherent cells**

#### **2.2.2.1 Concept of PDMS wells**

For this part of the project, CSC and non-CSC has to be distinguished through their biomechanical properties. This requires analyzing them separately. To do so, a possible option is to sort them based on cancer stem cell marker. In the case of breast cancer cells, it has been shown that CSC could be distinguished with  $CD44^{high}/CD24^{-/low}$  phenotype or through their high aldehyde dehydrogenase (ALDH) activity [93]-[95]. Unfortunately, sorted CSC go through a rapid differentiation when isolated and put back in culture (50 % of differentiation after 24 h). Thus, the analysis of cell properties had to be performed just after sorting them when cells were still in

suspension. As mentioned above, conventional AFM protocols require the adhesion of cells to a substrate (**Fig. 2.1 (a)**). Thus, AFM is not suitable for the measurement of non-adherent cells in suspension (**Fig. 2.1 (b)**). To investigate the physical properties of the sorted cells in suspension by AFM, cells must stay in position during cantilever indentation test. Therefore, I prepared a microwell device to individually isolate cells and to keep them in defined position (**Fig. 2.1 (c)**, **(d)**). This device was designed based on the dimension of targeted cells.



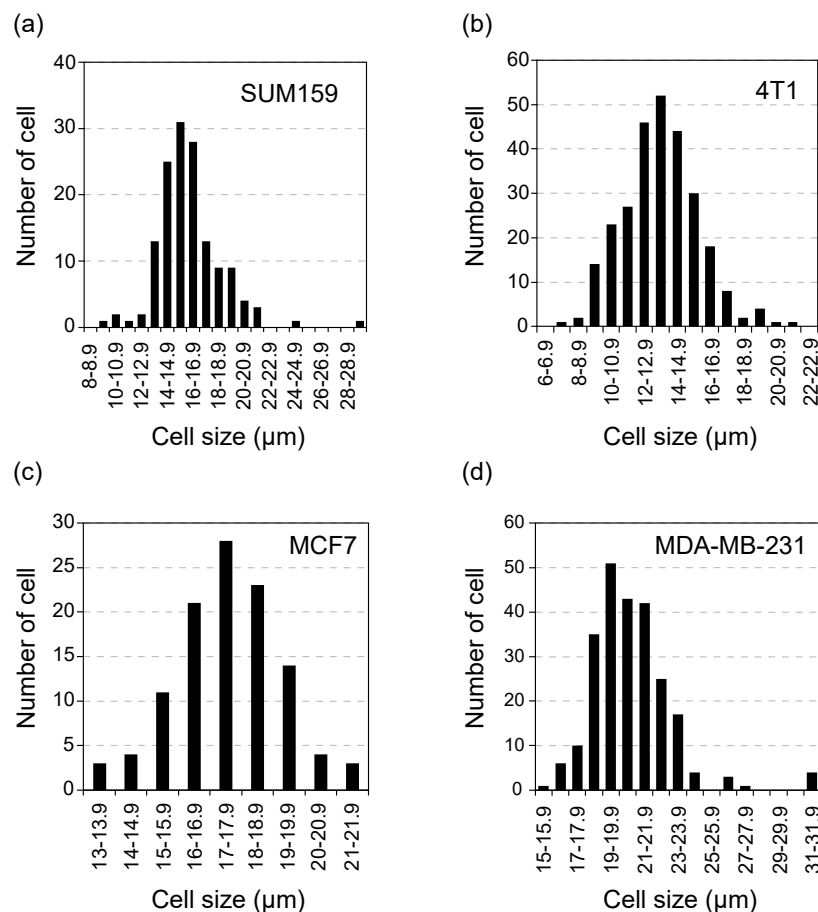
**Fig. 2.1** Using AFM for single cell analysis. **(a)** The conventional AFM indentation test with the adherent cell. **(b)** AFM faces certain difficulties when applied on floating cells. **(c)** Using PDMS wells for cell capturing during AFM indentation test. **(d)** PDMS wells installed inside a petri dish prior to AFM measurements.

### 2.2.2.2 Cell size measurement

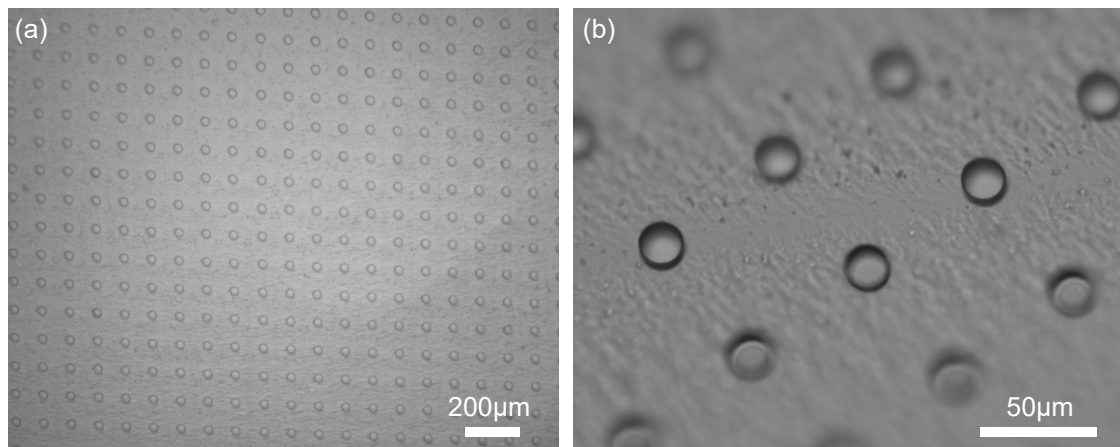
To design an appropriate microwell device, a preliminary test was performed using different cell lines. Cells used in this experiment, SUM159PT, MCF7 and MDA-MB-231, are human breast cancer cell lines, and 4T1 is malignant neoplasms of the mouse mammary gland. Cells were first detached from the flask with 1 mL of trypsin and put on a glass plate (Malassez slide).

On an inverted microscope stage, one hundred cells have been measured to obtain their average diameter using a calibrated NIS software (Nikon). As a result, the size of cancer cells were ranging between 13  $\mu\text{m}$  and 22  $\mu\text{m}$ , as shown in **Fig. 2.2**. To maximize the number of cells captured in a microwell device, devices were designed to have wells with 10  $\mu\text{m}$ , 15  $\mu\text{m}$ , 20  $\mu\text{m}$ , 22  $\mu\text{m}$ , 25  $\mu\text{m}$  and 30  $\mu\text{m}$  in diameter.

Microwells were molded in Polydimethylsiloxane (PDMS, Dow Corning) by performing simple microfabrication techniques. A negative photo resist, SU-8 3010 (Negative Epoxy Resists, MicroChem), was patterned to obtain microwells for repeated molding process, as shown in **Fig. A.1** in **Appendix A** and **Fig. 2.3**. Since PDMS is a bio-compatible and transparent material, it is suitable for cell AFM measurements.



**Fig. 2.2** Measurement of cancer cells size on different cell lines. Prepared cell lines were as follow: (a) SUM159PT, (b) 4T1, (c) MCF7 and (d) MDA-MB-231.



**Fig. 2.3** Microscope images of the fabricated PDMS microwells. **(a)** The aligned PDMS holes (at low magnification). **(b)** Tilted image of PDMS holes.

### 2.2.2.3 Preparation of cells

Triple negative human breast cancer cell line, SUM159PT (BioIVT, Westbury, USA), was used for AFM measurements. This cell line has been selected for its high stem cell frequency with 2 to 4 % of total population. Aldehyde dehydrogenase (ALDH)'s have been identified as possible biomarkers for numerous CSC. Breast cancer stem cells have a high activity of ALDH [93]-[95]. An inhibitor of ALDH activity, N,N-diethylaminobenzaldehyde (DEAB), is supplied as a negative control for this assay. The negative control DEAB was used for identifying ALDH positive of CSC.

A commonly used method to identify and isolate stem cells was via the ALDEFLUOR Assay (StemCell Technology, Inc., Durham, NC) that measures ALDH activity in live cells. At subconfluence of monolayer culture, SUM159PT was labeled using that kit, see **Appendix B** for details.

Then, non-CSC and CSC were separated using Cell Sorter (BD FACSAria III, BD Biosciences) at Cytometry facility BICEL (Bio Imaging Center Lille) in IRCL (Institut pour la Recherche Contre le Cancer). The 30 % of more negative cells were isolated as non-CSC and CSC were collected into tubes containing the F12 culture medium. The procedure for placing the collected cells on the petri dish for AFM measurement is shown below.

1. 24 h before plating the cells, an AFM petri dish on which PDMS microwells were placed and filled with 2.5 mL of culture medium or phosphate-buffered saline (PBS, 8.475 g NaCl,

- 1.093 g  $\text{Na}_2\text{HPO}_4$ , and 0.276 g  $\text{NaH}_2\text{PO}_4$  in 1 L DI water; pH 7.4) beforehand, was kept overnight at 4 °C, allowing the air contained in the microwell to dissolved in the media.
2. After cell sorting, cell solutions were centrifuged at 1000 rpm for 5 min and the supernatant was discarded.
  3. Cell pellet was homogenized with 2 mL of the culture medium.
  4. The AFM dish was rinsed with media and filled with 1 mL of F12 completed media and 1 mL of cells solution.
  5. Cells were then centrifuged at 1000 rpm for 3 min to allow cells to enter microwells. Visual verification of cells in wells were done under a microscope.
  6. The culture liquid in the AFM dish was changed twice for 1 mL each time.

The culture medium was exchanged again before setting the petri dish to AFM. The frequency of well occupation was about 10 % to avoid accumulation of several cells in a well, especially, in a larger one.

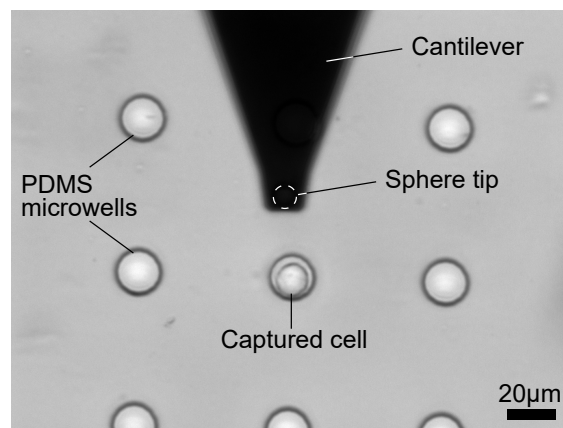
### 2.2.3 Cell biomechanical properties measurements by AFM

For this measurement, we selected a cantilever with a 10- $\mu\text{m}$  ( $\pm 10\%$  range) diameter spherical ball (CP-PNPL-BSG-B-5, sQube) made of borosilicate glass and with an average force constant  $k \sim 0.08$  N/m. AFM was calibrated to compress approximately 10 % of the cell height. A z-stage movement (Tip-sample separation) was 5  $\mu\text{m}$  and an indentation depth of 0.5  $\mu\text{m}$  with 1.0  $\mu\text{m/s}$  constant extend speed and with 0.5 s extend time. With this spherically tipped cantilever, 3 force curves were taken from each of the studied cells near its center. All tests were done using a 37 °C heater to keep the temperature uniform throughout the measurement time.

Using the above AFM setting, the indentation test with SUM159PT floating cancer cells was performed. The AFM indentation test took about 1 hour for staining cells,  $\sim 2.5$  hours for sorting cells with a cell sorter, 0.5 hours for the preparation of AFM dish and cells, 1~2 hours for calibrating AFM itself, then several hours for performing the actual measurements. This long procedure allows measurements on either CSC or non-CSC in a whole day.

First, cells were sorted into two groups presumed to be CSC or non-CSC from SUM159PT by the cell sorter, and then, were seeded in the AFM dish. Using the protocol explained above, the indentation test was performed once (1 day) on non-CSC and three times (on 3 different days) on CSC.

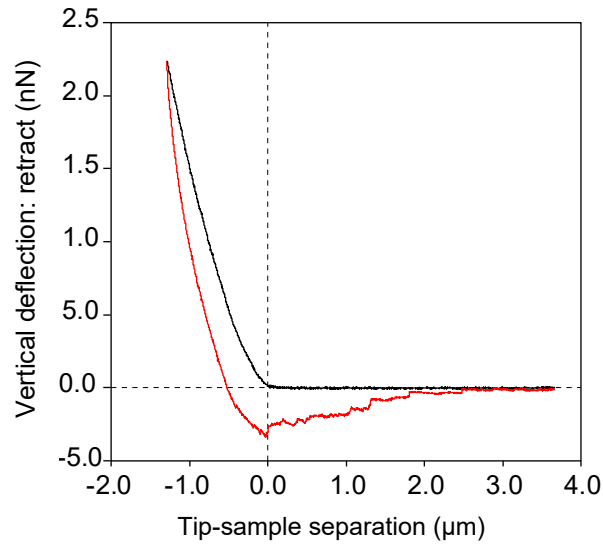
An image of a petri dish with PDMS microwells is shown in **Fig. 2.4**. The black object is the shadow of the cantilever with a 10- $\mu\text{m}$  sphere tip at the end (illustrated with a dashed circle in **Fig. 2.4**). A captured single cell can be seen inside a well. This is a typical view of the petri dish during an experiment monitored with an inverted microscope integrated with an AFM. During this experiment, only one of the wells in the observation area was occupied with a cell. A combination of 10- to 30- $\mu\text{m}$  wells were used to pick the appropriate cell-to-well correspondence as the cell size of SUM159PT was varying from 9  $\mu\text{m}$  to 29  $\mu\text{m}$  (**Fig. 2.2 (a)**). A small cell in a large well can lead to a double-occupancy or suffer from position shift of the cell during indentation. Only cells having single occupancy were selected and analyzed.



**Fig. 2.4** PDMS microwells, the cantilever with a sphere tip and the captured floating cell seen under the microscope of AFM.

The measurements were performed by aligning the sphere tip with the center of the cell manually under the microscope, and then compressing the cell about 10 % of its size. Force curves were obtained by performing cell indentation tests. An example result of the force curve from a non-CSC analysis is shown in **Fig. 2.5**. The curve includes the data on indentation (pushing) in black, withdraw (pulling) in red, deformation and adhesion force. A typical day of AFM experiments results in few tens of single cell measurements. Moreover, the data analysis has to be carried out in the following days using the obtained experimental results.





**Fig. 2.5** Typical force-distance curve of the cell by sphere tip. This curve was taken from non-CSC group. The extend curve is black and the retract curve is red.

### 2.2.4 Data analysis

Data analysis was performed applying the Hertz's model on the indentation curves using the JPK Data Processing Software. The Hertz model is the standard model used to analyze AFM force-distance curves and calculate the apparent Young's modulus (elastic modulus,  $E$ ) [18]-[40].

The Hertz model was several assumptions:

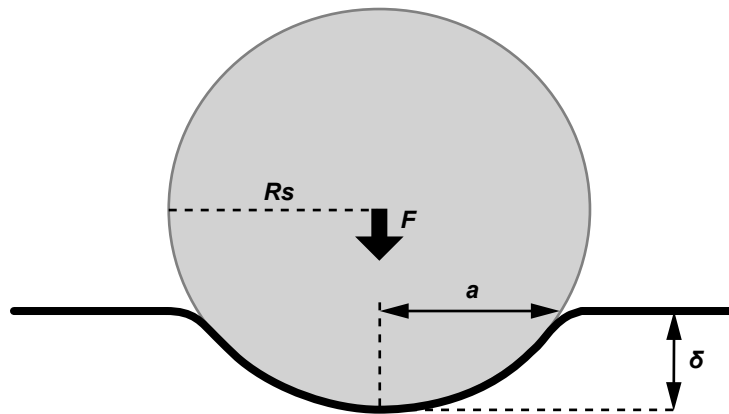
- (i) the material is homogeneous, isotropic, and semi infinite,
- (ii) the material is a linear-elastic solid, and
- (iii) the material undergoes infinitesimally small strains.

The original Hertz model is generally valid for a circular paraboloid, and as an approximation for very shallow contact between two spheres. The key parameter that is usually adapted is the radius of the contact region. For a sphere tip, indentation  $\delta$  is related to tip load  $F$  by

$$F = \frac{E}{1 - \nu^2} \left[ \frac{a^2 + R_s^2}{2} \ln \frac{R_s + a}{R_s - a} - aR_s \right] \quad (2.1)$$

$$\delta = \frac{a}{2} \ln \frac{R_s + a}{R_s - a} \quad (2.2)$$

where  $\nu$  is the Poisson's ratio which was assumed to be 0.5,  $a$  is the radius of the contact circle,  $R_s$  is the radius of the sphere,  $E$  is the apparent Young's modulus (**Fig. 2.6**). Using this Hertz's model, the Young's modulus of the cell can be obtained. As already mentioned, the indentation test was performed once (1 day) on non-CSC and three times (on 3 different days) on CSC. From these experiments, 30 non-CSC data and 29 CSC data was obtained. Each cell has 3 force curves.



**Fig. 2.6** Geometric interaction between sphere tip and surface of the object.

Histograms of the measured Young's modulus for non-CSC data and CSC data (sorted on different days) are shown in **Fig. 2.7**. Before sorting cells, the amount of CSC originally presented in the cell population was very small. Also, only 3 % of CSC were collected by the sorting. Accordingly, the number of CSC and condition of CSC itself changed depending on the day. It was expected non-CSC to have higher Young's modulus because of its lower metastatic potential, however there was no significant difference.

**Fig. 2.8** illustrates dot plots of the measured Young's modulus on different sorting days. The average cell stiffness values (mean  $\pm$  SD) obtained were  $650 \pm 145$  Pa for non-CSC, and  $850 \pm 145$  Pa,  $1100 \pm 370$  Pa and  $240 \pm 110$  Pa for CSC on different sorting days, CSC1, CSC2 and CSC3, respectively. The calculated probability between non-CSC and CSC was  $p = 0.012$ . Even within the same CSC population, the average Young's modulus varied depending on the sorting day. In CSC2, the Young's modulus was greatly varied and the maximum was 2300 Pa. CSC3 showed the lowest Young's modulus compared to all other data. If only compared between non-CSC and CSC3, the calculated probability was  $p = 6.44 \times 10^{-17}$ . From these results, it is doubtful to use AFM for floating cells.

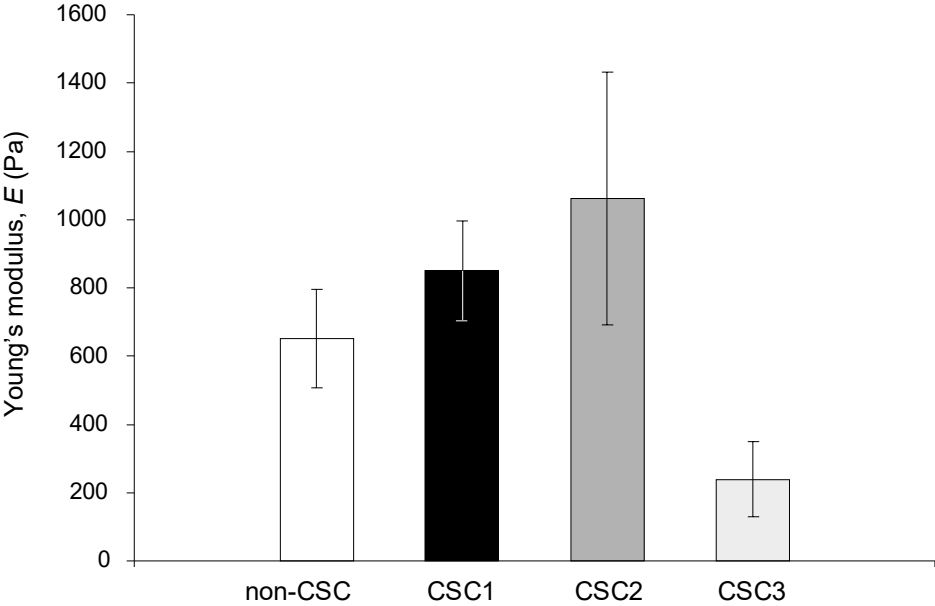


Fig. 2.7 Histogram of analyzed Young's modulus between non-CSC and CSC1, CSC2, and CSC3.

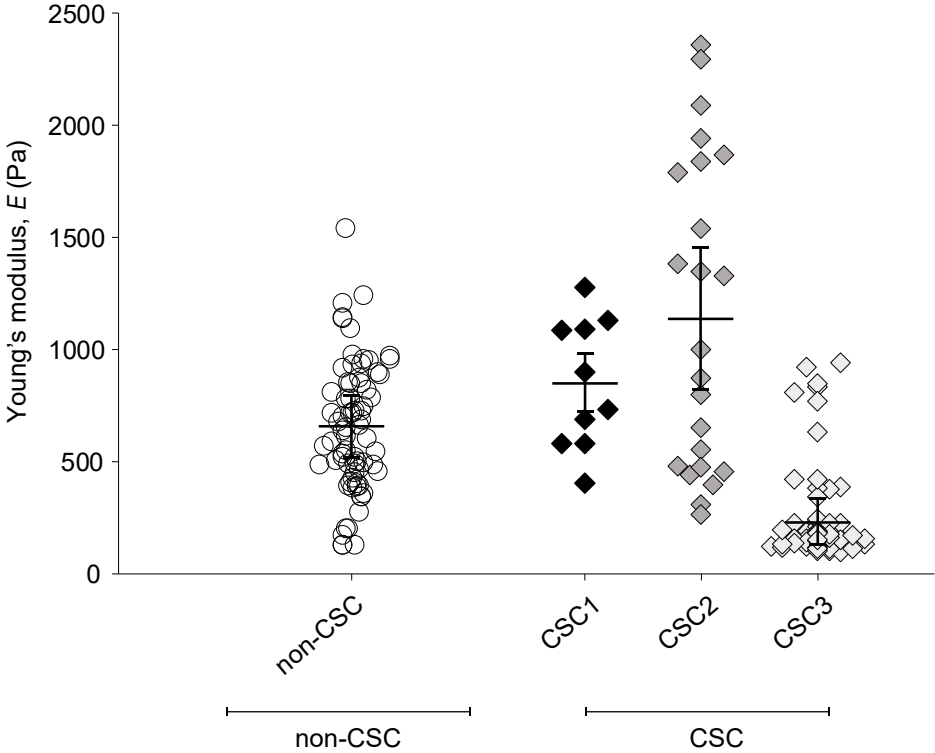


Fig. 2.8 Yount's modulus per day.

### 2.2.5 Conclusions

This part suggests that there may be some difference between the stiffness values of CSC and non-CSC. However, AFM technology appears not to be compatible with non-adherent cell analysis even with an adapted protocol. Indeed, low throughput screening of AFM forces the analysis of non-CSC and CSC in separated days although they were sorted on the same day. This adds high variability within measurements. Also, additional problems could lead to miss interpretation of the AFM data:

1. The ratio between the well size and captured cell size

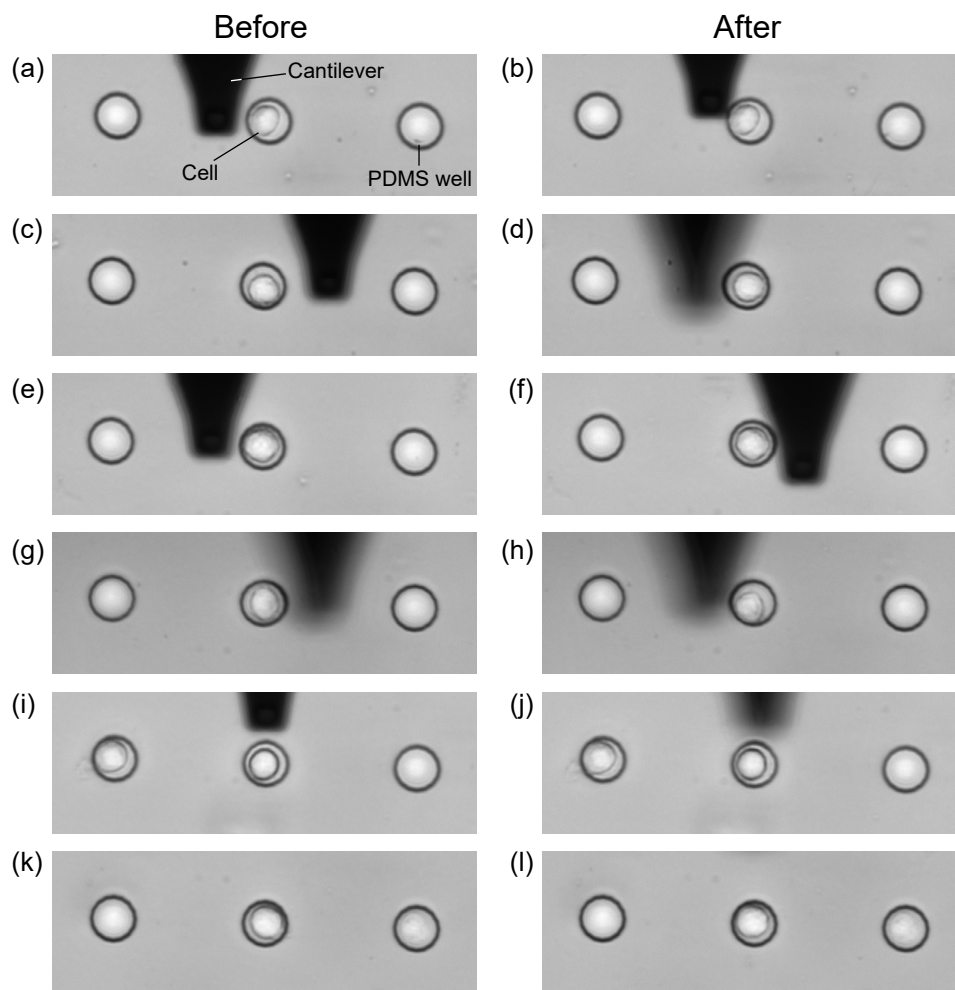
No matter how well designed, cells are always smaller than wells to enter. As a result, they may move inside the well during AFM measurements. Although this approach works much better than the conventional AFM measurements, it still results in some variability. Moreover, depending on the cell size to well size, the effect of the walls can be different, causing another source of variability.

2. Cells in suspension

Even if cells appear to be captured in the well, it is not guaranteed to have them at the bottom of the PDMS well, leaving liquid solution in between them and the PDMS surface. Centrifuging the plate at 500 rpm for 5 min might reduce this effect. However, observations clearly showed cells going down few micrometers during the indentation. Since the 10 % compression starts automatically when the cantilever senses the cells, the measurements often ends before the cell reaches to the bottom of the PDMS microwell. So, in some cases, it was impossible to quantify the compression, making cells difficult to be compared.

3. Unstable position of cells in the well

AFM has been developed for adherent cells. In our conditions, we tried to adapt the conventional protocol by isolating cells in the individual well corresponding to their size. However, for some cells, the position of cell moved slightly after indentation test, adding bias to our analysis as **Fig. 2.9** shows the position of cells before and after the indentation test. Also, sometimes a cell can have stuck on the cantilever sphere and move out from the well. So, we could not validate the uniformity of the compression through the indentation even if cantilevers with the sphere tip were used.



**Fig. 2.9** AFM images of cantilever, PDMS microwells and the captured cell. (a), (c), (e), (g), (i), and (k) are images of before pushing by the AFM cantilever and (b), (d), (f), (h), (j), and (l) are images of after pushing.

Due to these problems, quantitative measurement by AFM is difficult even when PDMS wells are used to capture the floating cell during the cantilever indentation.

For these reasons and already mentioned others (low throughput, compatibility difficulties with non-adherent cells, and issues on the microwell approach), the adapted protocol for AFM to analysis stiffness of cells might still not be sensitive enough to distinguish different populations of cells. Also, single mechanical property as stiffness might not be sufficient to segregate different population.

## 2.3 Using Silicon NanoTweezers technology to examine non-adherent cells

### 2.3.1 Background of SNT

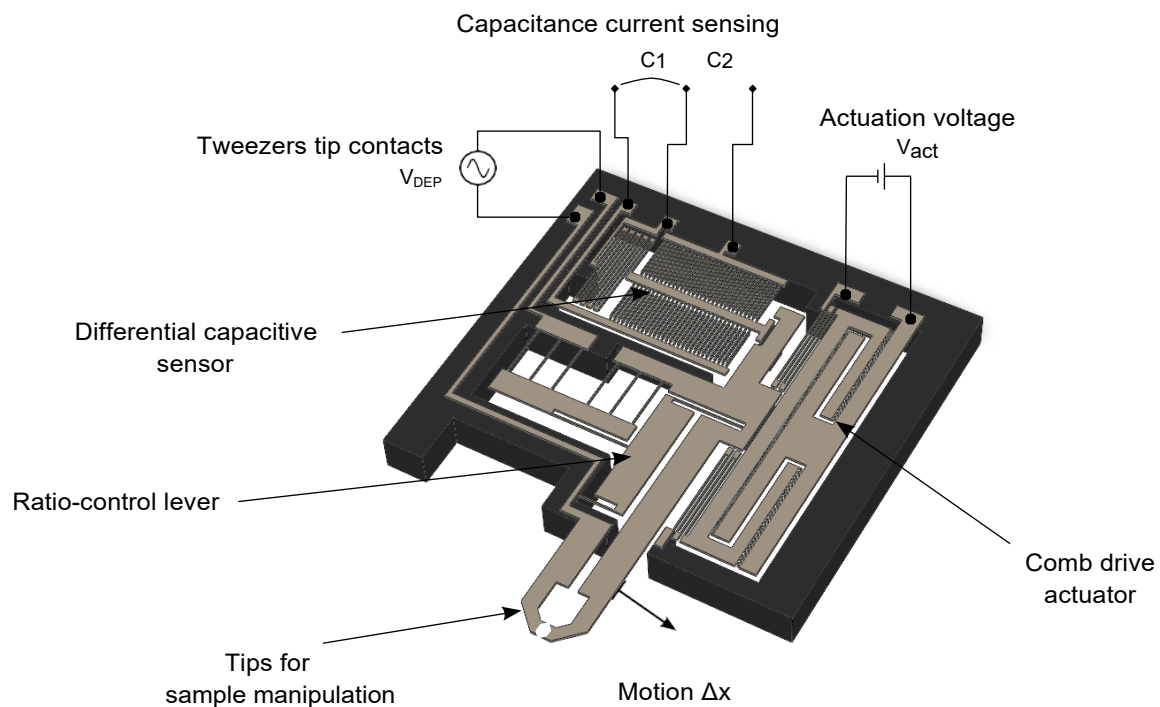
Dynamic manipulation at the single cell level has become possible with the development of micro/ nano technology and has contributed to the measurement of the mechanical properties of cells. In the system using the atomic force microscopy (AFM), it is possible to dynamically map the inside of a single cell since it has high sensitivity and high spatial resolution. It is difficult, however, to measure cells in a floating state with high throughput due to the scanning speed requiring time. In recent years, high throughput cell characteristics measurement using chips based on microfluidics has been proposed [88]-[92]. In this method, cell characteristics are measured by continuously introducing cells using a microchannel as a conveyance system. In addition to this, a method combining the microchannel with MEMS device as characteristics measurement system maintains high sensitivity like AFM and takes advantage of the features of a microchannel [79].

Microelectromechanical system (MEMS) are miniature devices comprised of integrated mechanical (levers, springs, deformable membranes, vibrating structures, etc.) and electrical (electrodes, wiring, resistors, capacitors, inductors, etc.) components designed to work in concert to sense and report on the physical properties of their immediate or local environment. This kind of MEMS application has become one of the major biological experimental tools, recently [74],[88]-[92]. Many MEMS devices are designed for investigating mechanical properties of cancer cells, such as a MEMS based piezoresistive microcantilever.

Silicon NanoTweezer (SNT), developed in Fujita laboratory, Institute of Industrial Science (IIS), The University of Tokyo [75],[77], is one of the MEMS devices that can perform continuous measurements while monitoring response in real-time. A 3D schematic image of the simplest model of the SNT with the single arm operation is shown in **Fig. 2.10** [77]. An SNT can directly manipulate and characterize biosamples, e.g.,  $\lambda$ -DNA, microtubules, and single cells. The SNT consists of three main parts as follows:

- (i) a pair of opposing tips to handle biosamples,
- (ii) an electrostatic microactuator to drive the SNT for static or harmonic measurements, and
- (iii) an integrated differential capacitive sensor to detect displacement of the tip; combined

analysis of displacement and applied force by the actuator allows to know biophysical changes in real-time.



**Fig. 2.10** Illustration of 3D schematic image of the simplest model of the SNT with single arm actuation. [74]

In the previous studies, SNT was used to perform static and dynamic mechanical characterizations on biosamples for different purposes:

1. Concerning radiotherapy, SNTs were used to examine the effect of irradiation on DNA structure for optimizing the treatment. To investigate DNA degradation mechanisms under ionizing radiation to improve treatment efficiency on tumour, the SNT captured a  $\lambda$ -DNA bundle in between the opposing tips and was used for real-time biomechanical characterization of  $\lambda$ -DNA degradation during irradiation. The SNT was placed under the radiation machine (Cyber Knife, Accuray), endured the harsh environment of the therapeutic radiation beams, and still retained molecular-level detection accuracy during exposure to radiation beams. The real-time  $\lambda$ -DNA degradation was observed in terms of biomechanical stiffness and viscosity reduction, both in air and in liquid [85],[86].

2. The captured  $\lambda$ -DNA was exposed to different types of solutions. Real-time observations allow investigating chemical reactions between the captured DNA and molecules in the solution [80][81].

Cells can regulate their mechanical properties in order to adapt their shape to perform particular tasks like migrating through tiny junctions. Therefore, cells' mechanical properties reflects the pathological behaviour. The SNT design optimization has to be validated for efficiently and quantitatively characterizing mechanical properties of cells. This section explains the operation principle and validates the characterization by performing cell deformation experiment.

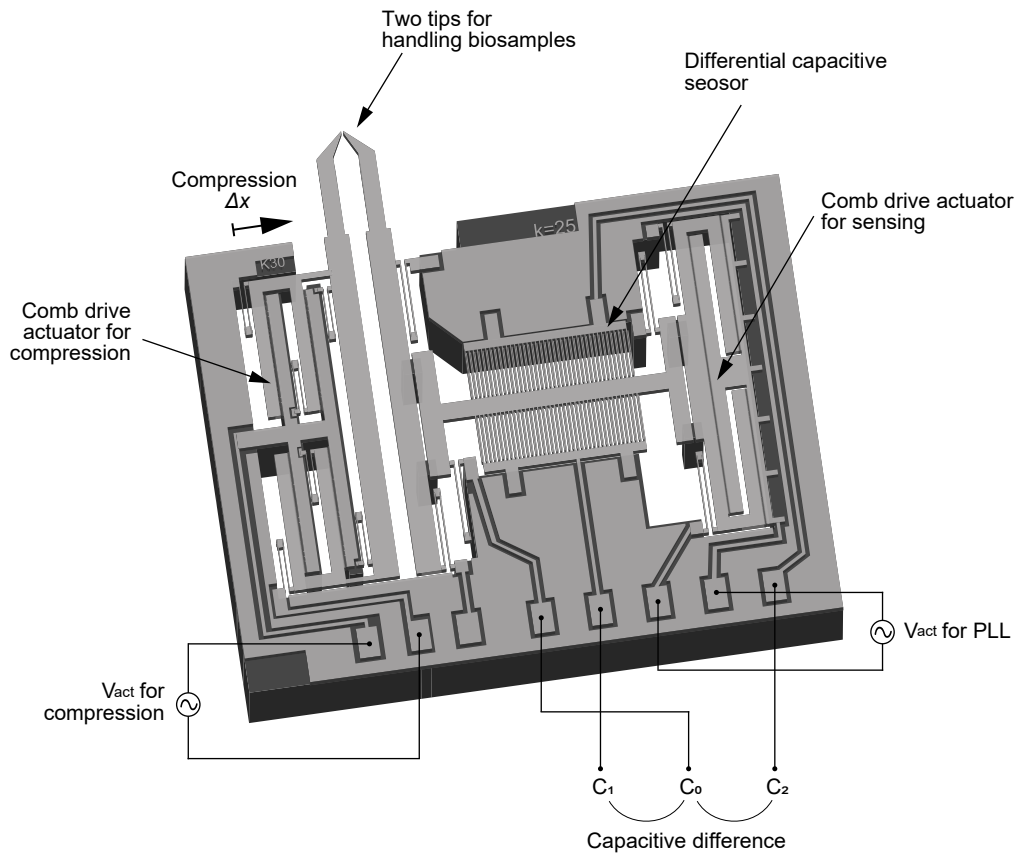
As mentioned above, SNT could handle biosamples and perform measurements on them. Design parameters of an SNT, such as a mechanical spring shape, a spring constant, and electrostatic actuators, can be adjusted easily to change the characteristics of the device, e.g., measurement sensitivity and actuation force. **In section 2.3.2**, I explain how to adapt SNT for floating cancer cell measurements and show actual experiments with a separated microfluidic channel device. Moreover, optimizing the parameters of non-adherent cancer cell measurements by SNT serves as a base to the new device described in the following chapter.

### 2.3.2 Adapting the SNT design for single cancer cell measurements

An adapted SNT is shown in **Fig. 2.11**. It consists of **two probes with flat tips** at their ends that can be actuated separately (**double arm actuation**) to handle biosamples between two tips during measurements. One side of tips moves toward an opposing tip by electrostatic force and is used for compressing biosamples. The other one is used for sensing the displacement ( $x$ -direction) using an **integrated capacitive sensor**. As mentioned above, an SNT consists of three main parts and these parts have to be adapted for single cell measurements.

An appropriate DC or AC voltage signal is applied at the compression side to perform a compression assay on a cell captured between the tips. During the assay, mechanical response of a cell is monitored in real-time using harmonic measurement by driving the electrostatic actuator of the sensing tip at resonance [74],[102]. The sensor, consists of a tri-plate configuration with transverse combs, is used to measure the displacement of the sensing tip during compression [99],[100]. A centre electrode  $C_0$ , mechanically connected to the sensing tip, moves between two fixed electrodes  $C_1$  and  $C_2$ . The differences between two capacitance,  $C_0-C_1$  and  $C_0-C_2$ , are related to the displacement  $\Delta x$  of  $C_0$ , the sensing tip and thus the cell under compression [74],[87]. A detailed description of the operational principle is available in **Appendix C**.



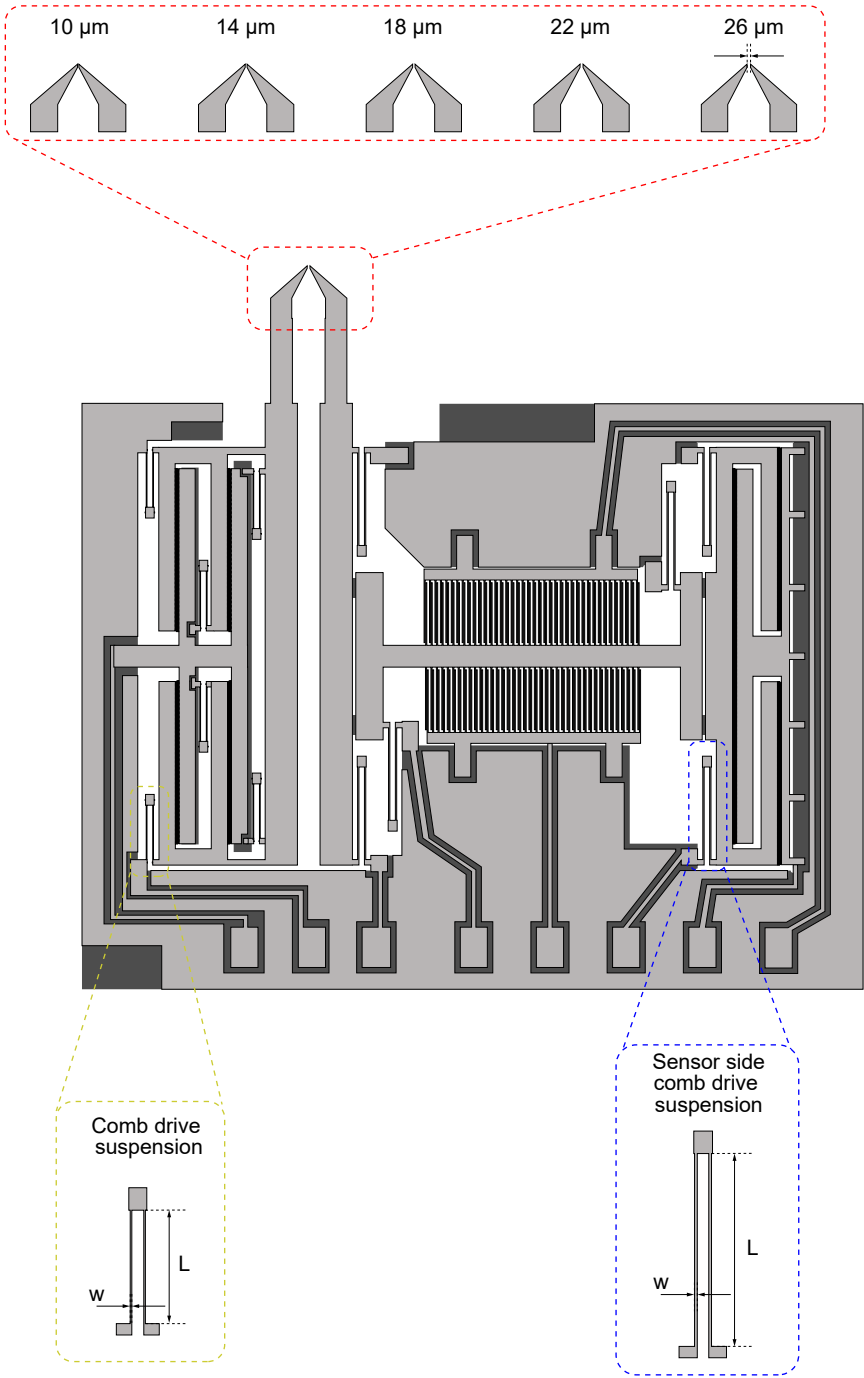


**Fig. 2.11** Illustration of 3D schematic image of SNT.

To achieve sensitive detection, the SNT parameters have to be optimized for measuring cancer cells having softer characteristics compared to their benign counterparts. The optimization parameters corresponding to the 3 main parts of the SNT structure, such as gap distance between tips to handle cells with the targeted size, the mechanical suspension stiffness of the sensing side to tune the detection sensitivity for a cancer cell, and the compression side to drive the comb drive actuator far enough to squeeze the cell at suitable voltage levels (**Fig. 2.12**).

### 2.3.2.1 Gap distances

As shown in **Fig. 2.2**, the measured cell size was not uniform even in the same cell line. The distance of the actuation (gap-closing) was depending on the mechanical design. In order to capture various size of cells with the same mechanical design, the gap between tips were designed as  $10\ \mu\text{m}$ ,  $14\ \mu\text{m}$ ,  $18\ \mu\text{m}$ ,  $22\ \mu\text{m}$  to  $26\ \mu\text{m}$  (see in **Fig. 2.12**). This allowed performing measurements on cells with different dimensions to make a better compression among the variety of cell types.



**Fig. 2.12** Adjusted designs for cell measurement.

### 2.3.2.2 Mechanical suspensions

The movable parts are suspended by flexible beams. Previously used in SNT, folded beam springs were adopted to reduce spaces in the system and enhance the displacement. In this double side actuation cell measuring SNT, six sets of mechanical suspensions are used in both compression and sensing sides to support movable structures as shown in **Fig. 2.12**. Also, electrical connections of device are provided through these suspensions.

Ideally, the SNT system is suitable for sensing whole cell mechanical response under compression. There are 3 factors limiting the stiffness characteristics of the system:

- (i) to survive during the fabrication,
- (ii) to be able to support the weight of movable part, and
- (iii) to prevent an attractive sticking between to comb fingers.

A mechanical stiffness of one spring  $k$  is given by the equation below:

$$k = \frac{1}{2} \times E \times t \times \left( \frac{w}{L} \right)^3 \quad (2.3)$$

where  $E$  is the Young's modulus of material (Si = 131 GPa) and  $L$ ,  $w$ , and  $t$  are length, width and thickness of the suspension beam, respectively. The thickness is 30  $\mu\text{m}$  which is the thickness of the frontside silicon layer of the SOI wafer.

Some dimensions of SNT, however, are very sensitive to variations in etching step such as undercutting and difficult exactly to fabricate as designed in the mask. Therefore,  $L$  and  $w$  have to be adjusted that can survive during the etching process. Assuming the suspension width as  $w = 7 \mu\text{m}$ , and the length as  $L = 500 \mu\text{m}$  and adopting 6 springs designed in both the compression side of spring  $k_l$  and the sensing side of spring  $k_r$ , the total stiffness of compression side  $k_L$  and sensing side  $k_R$  are defined by

$$k_L = 6 \times k_l \quad (2.4)$$

$$k_R = 6 \times k_r \quad (2.5)$$

The total stiffness of compression side is assumed  $k_L = 30$  N/m, the stiffness of one spring is calculated as below:

$$\begin{aligned} k_l &= \frac{1}{2} \times 131 \times 10^9 \times 30 \times 10^{-6} \times \left( \frac{7 \times 10^{-6}}{500 \times 10^{-6}} \right)^3 \\ &= 5.39... \text{ [N/m]} \end{aligned}$$

From above, the total stiffness of compression side is:

$$\begin{aligned} k_L &= 5.4 \times 6 \\ &= 32.4 \approx 30 \text{ [N/m]} \end{aligned}$$

Also, a softer stiffness of total spring in compression side was designed. The total spring constant was  $k_L = 15$  N/m for a larger displacement with lower voltage.

The stiffness of one spring in the sensing side,  $k_r$ , was also defined by **Equation (2.3)**. Two types of total stiffness in the sensing side,  $k_R$ , were designed, as 25 N/m and 5 N/m. The total stiffness of  $k_R = 25$  N/m was used previous SNT experiments [86]. The sensor was already demonstrated to measure differences in mechanical properties of biological samples in real-time. The total spring constant stiffness in the sensing side of  $k_R = 5$  N/m was designed to have higher sensitivity than  $k_R = 25$  N/m. However, since the beam width of the spring is narrower than other spring designed, the stability may be impaired by disturbance. In particular, the liquid flow may increase the noise during sensing. Details of dimensions and calculated values of SNT spring stiffness are shown in **Table. 2.1**.

**Table 2.1** Design of mechanical suspensions

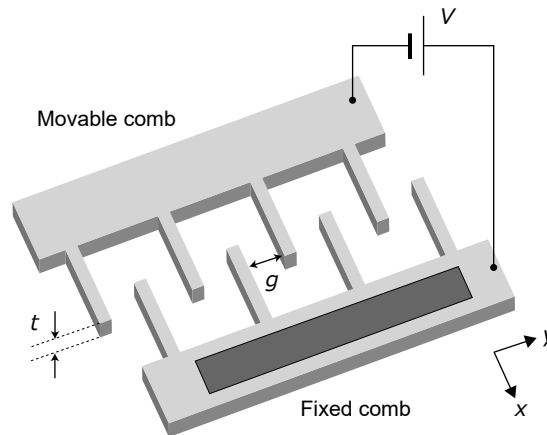
	Total stiffness (N/m)	Dimensions $L \times w \times t$ ( $\mu\text{m}$ )	Stiffness $k_l, k_r$ (N/m)
$k_L$	30	$500 \times 7 \times 30$	5.4
	15	$900 \times 9.8 \times 30$	2.5
$k_R$	25	$850 \times 11 \times 30$	4.2
	5	$900 \times 6.7 \times 30$	0.8

### 2.3.2.3 Electrostatic force

The local electrostatic force in  $x$ -direction,  $F_x$ , acting on the movable electrode of the capacitance  $C_{total}$  composed by comb drive fingers is given as below:

$$\begin{aligned} F_x &= \frac{\partial U}{\partial x} = \frac{1}{2} \frac{\partial C_{total}}{\partial x} V^2 \\ &= \frac{1}{2} \epsilon_0 t \frac{V^2}{g} \times n \end{aligned} \quad (2.6)$$

where the  $\epsilon_0 = 8.854 \times 10^{-12}$  F/m is the vacuum permittivity,  $t$  is the thickness of the wafer (teeth height),  $V$  is the potential difference between the electrodes as the actuation voltage,  $g$  is the gap between the opposite teeth, and  $n$  is the total number of teeth. The schematic image of the comb drive teeth is shown in **Fig. 2.13**.



**Fig. 2.13** Schematic image of the comb teeth.

The actuation force (driving force) is proportional to the square of the applied potential difference (applied voltage)  $V^2$  and the thickness of the wafer  $t$ . On the other hand, it is inversely proportional to the gap width of  $g$ . The total number of teeth in compression side is  $n = 1000$  (125 teeth-pairs in 4 groups). According to these parameters, the actuation force  $F_x$  is calculated as:

$$\begin{aligned}
F_x &= \frac{1}{2} \times 8.854 \times 10^{-12} \times 30 \times 10^{-6} \times \frac{V^2}{2 \times 10^{-6}} \times 1000 \\
&= 6.65405 \times 10^{-8} \times V^2 \\
&= 66.4 \times 10^{-9} \times V^2
\end{aligned} \tag{2.7}$$

if the actuation voltage  $V$  is 50 V,

$$\begin{aligned}
F_x &= 66.4 \times 10^{-9} \times 50^2 \\
&= 1.66125 \times 10^{-4} \text{ [N]} \\
&= 166 \text{ } [\mu\text{N}]
\end{aligned} \tag{2.8}$$

Applying the actuation force  $F_x$  shown above at the compression side, the displacement on the compression side when 50 V is applied as the actuation voltage is:

$$F_x = k \cdot x \tag{2.9}$$

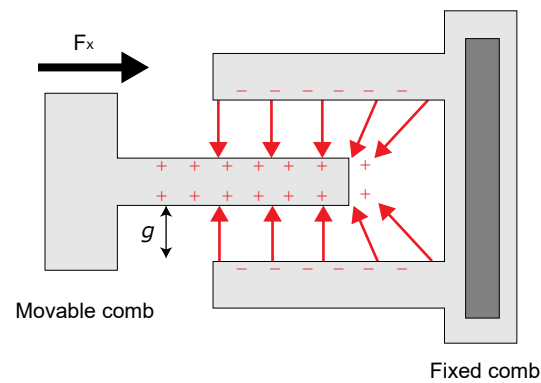
$$\begin{aligned}
x &= \frac{16.6 \times 10^{-5}}{30} \\
&\doteq 5.5 \times 10^{-6} = 5.5 \text{ } [\mu\text{m}]
\end{aligned} \tag{2.10}$$

This shows that the compression tip can be displaced about 5.5  $\mu\text{m}$  by applying 50 V.

#### 2.3.2.4 Instability of comb drive

In the gap-closing-type-parallel-plate actuator, the attracting force has a strong gap dependence. When the gap distance decreases to 1/3 from the initial gap, the occurrence of pull-in effect is inevitable. The comb drive actuator has no gap dependence and instability due to the pull-in effect can be avoided. In the comb drive electrode, the forces generated in  $\pm y$ -direction of the comb cancel each other, as shown in **Fig. 2.14**. Net force is only the force actuating at teeth edges in  $+x$ -direction. Suppose the movable tooth displaces to  $+y$ -direction slightly. The upper gap shortens and field strength increases, and vice versa. Consequently, the tooth is attracted

more to +  $y$ -direction. If the applied voltage is high enough, the force exceeds the restoring force of the suspension in  $y$ -direction and both teeth stick together. Therefore, the suspension stiffness in  $y$ -direction must be designed high enough to avoid this instability.



**Fig. 2.14** Distribution of the force at comb teeth.

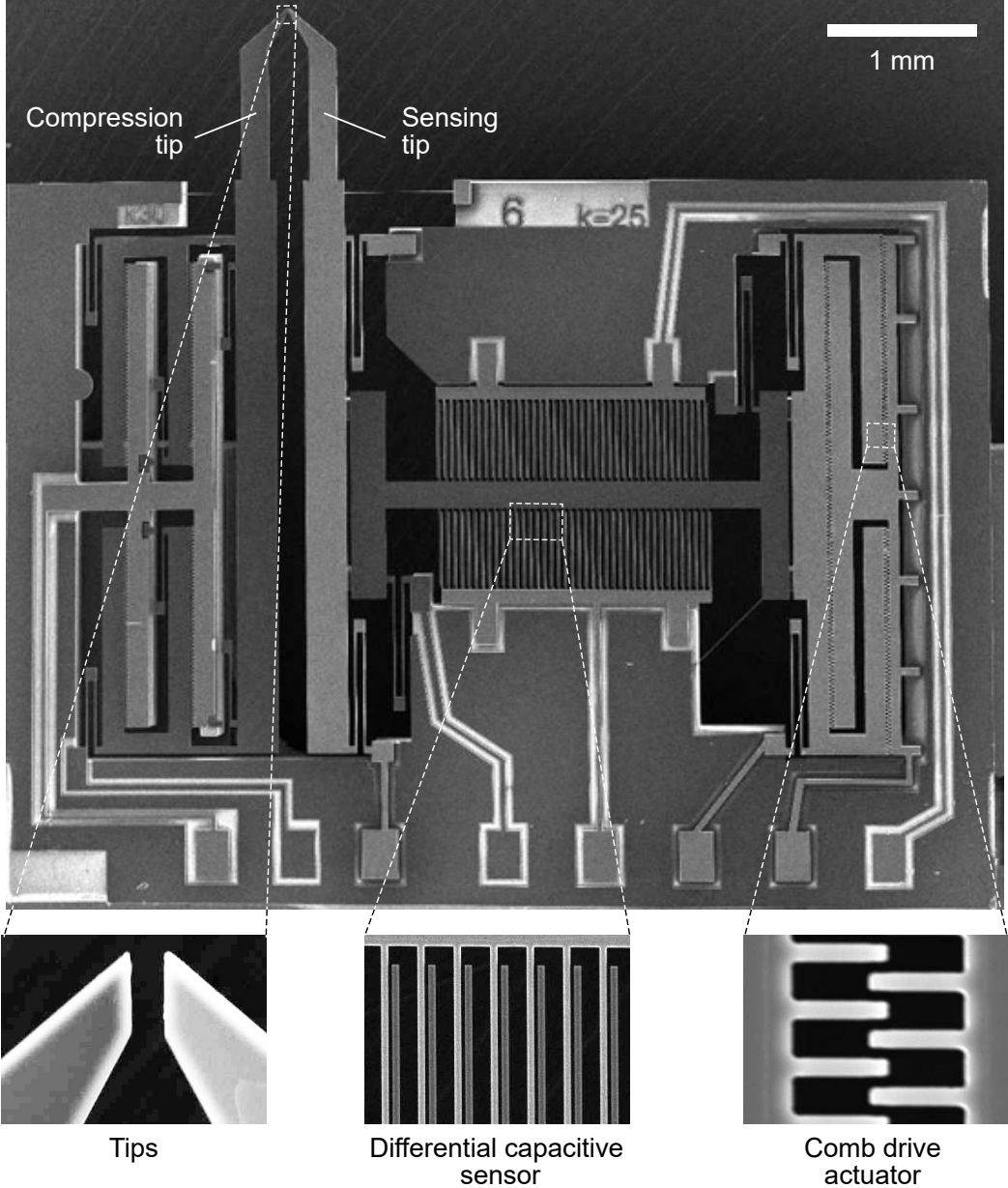
### 2.3.3 Fabrication process

#### SNTs

The SNT fabrication was based on a deep reactive ion etching (DRIE) process with two masks process. The substrate was an SOI wafer having 30  $\mu\text{m}$ -thick silicon device layer, 2  $\mu\text{m}$ -thick buried oxide (BOX:  $\text{SiO}_2$ ) insulator, and 350  $\mu\text{m}$ -thick silicon handling layer. Details of SNT fabrication was described in **Appendix D**. The SNT fabrication steps were summarized as follows.

1. A positive photoresist was spun on and patterned to form main components of device. The frontside Si layer is etched by DRIE.
2. Three protection layers ( $\text{SiO}_2/\text{Al}/\text{photoresist}$ ) protected etched structures during the backside fabrication steps.
3. The Al and positive photoresist layers were coated on the backside Si layer and formed as the etching mask. Then, the backside supporting structures were etched by DRIE.
4. The BOX layer was removed by HF.

A fabricated device was shown in **Fig. 2.15**.

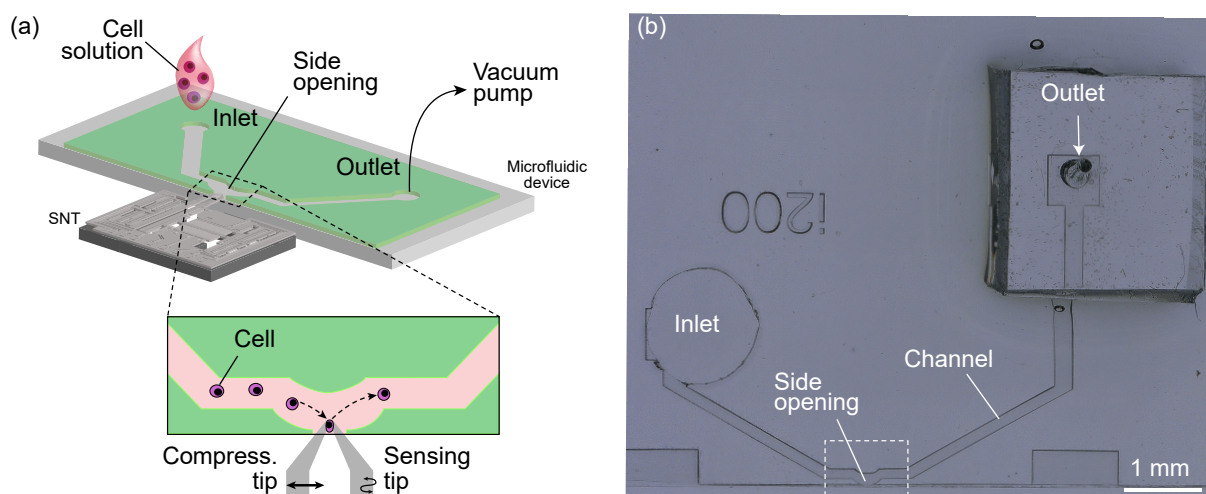


**Fig. 2.15** SEM images of fabricated device.



### Microfluidic channel

A microfluidic device for SNT was consisted of a microfluidic channel with a side opening and a glass cover slip. The microfluidic channel made of polydimethylsiloxane (PDMS, Dow Corning) slab was placed on a glass cover slip. For fabricating PDMS slab including the channel with the side opening, an SU-8 resist was formed and used as a mold for PDMS to transfer the channel with the side opening. The size of channel height and that opening area was about 80  $\mu\text{m}$  and the side opening of channel for inserting SNT tips was 100~200  $\mu\text{m}$  in width. That defined by the height of SU-8 structure in the mold fabrication process. In the PDMS slab, an inlet hole and an outlet hole were opened by a biopsy punch. The size of holes were 2 mm and 0.5 mm for inlet and outlet, respectively. The fabricated microfluidic device for SNT is shown in **Fig. 2.16**.



**Fig. 2.16** Microfluidic device. (a) SNT tips are inserted to the channel from side opening. (b) Top view of fabricated microfluidic device.

## 2.3.4 Experimental process

### 2.3.4.1 Device preparation

#### SNTs

SNTs were produced in 1/4 size of a 4-inch wafer. A total of 25 SNT devices could be fabricated in a single run. A chosen SNT was mounted on a printed circuit board (PCB) using a glue. Then, electrical connections between SNT and PCB were established by a bonding thin Al wires with 25  $\mu\text{m}\phi$ .

### Microfluidic device

After opening the inlet and outlet holes, the fabricated PDMS slab was placed on a glass cover slip. The sidewall of the PDMS microfluidic channel with side opening area was aligned with the edge of the glass cover slip manually. The presence of the side opening area at the edge of the glass cover slip allowed SNT tips to reach cells within the channel from there. The outlet hole was connected to a pressure controlled pump for applying a negative pressure to create a liquid flow in the channel.

#### 2.3.4.2 Setup

Both SNT and the microfluidic device were installed on a non-inverted microscope stage (VH-S30B, Keyence Corporation, Osaka, Japan) to monitor experiments in real-time. The microscope was placed on an anti-vibration stage (THORLABS, Inc., Newton, NJ, USA) to minimize possible ambient noise. SNT-mounted PCB was screwed to a fixed stage. Due to spring pins already installed and connected to peripheral electronics, screwing to the fixed stage not only positioned the SNT but also established the required electrical connections instantaneously. The microfluidic device was placed on an XYZ stage with the side opening facing to SNT tips. The outlet of microfluidic device was connected to the pressure-controlled pump (AF1, Elveflow, Paris, France).

Capacitive sensors electrodes ( $C_1$  and  $C_2$ ) of SNT were connected to a lock-in amplifier (Model 7230, AMETEK, Inc., Berwyn, PA, USA) *via* low noise preamplifiers (Model 5182, Signal Recovery, AMETEK, Inc., Berwyn, PA, USA).  $C_0$  was connected to a voltage source of a function generator for DC polarization (33500B, Keysight Technologies Inc., Santa Rosa, CA, USA). The lock-in amplifier output drove the sensing side actuator at the resonance frequency. The compression tip was connected to a second function generator (33500B, Keysight Technologies Inc., Santa Rosa, CA, USA) and a high voltage amplifier (WMA-100, Falco Systems BV, Katwijk aan Zee, The Netherlands) for applying compression cycles (AC or DC voltage).

All equipment including the SNT, the microfluidic device stage, the pressure-controlled pump, the lock-in amplifier and the function generator were connected to the computer and controlled with a modified LabVIEW program (version 16, National Instruments Corporation, Austin, TX, USA).

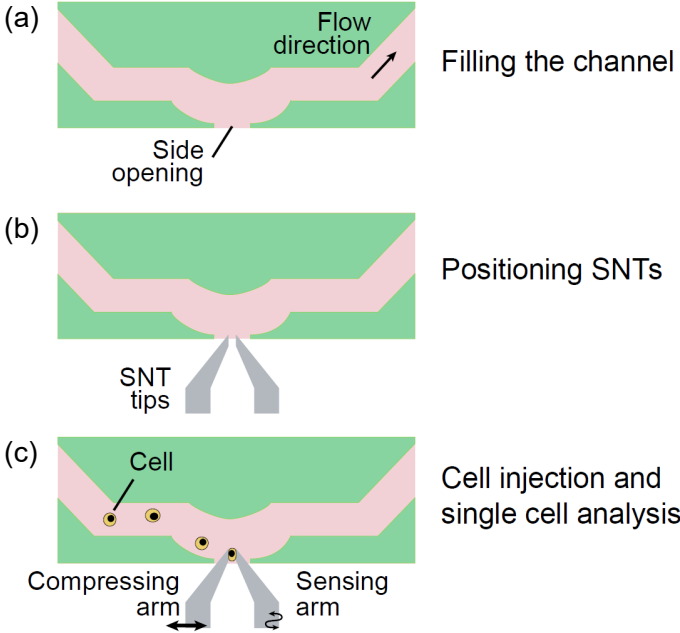
### 2.3.4.3 Cell preparation

Two breast cancer cell lines with different characteristics were prepared. T47D is a luminal breast cancer subtype with epithelial characteristics, estrogen receptor and progesterone receptor positive, while SUM159-PT is triple negative subtype with mesenchymal characteristics. Compared to non-metastatic T47D, SUM159-PT had very aggressive and highly metastatic properties. Subconfluent cells were detached from the flask by 0.05 % Trypsin. The tube that cells were gathered kept in the ice before injecting cells to the microfluidic channel.

### 2.3.4.4 SNT experiment protocol

After device and cell preparation, and equipment setup, the following experimental protocol was performed (**Fig. 2.17**).

1. Microfluidic device (including the connection tubes) was filled with PBS or culture liquid.
2. The first SNT calibration was done in the air.
3. SNT tips were inserted from the side opening of the microfluidic channel.
4. Second SNT calibration was done in the liquid.
5. Cells were injected *via* the inlet and a flow was created inside the channel by the pump to move cells towards the characterization area.
6. When cells reached the characterization area, the flow was stopped by controlling the pump.
7. A single cell was captured and cell compression cycles were applied to perform cell characterization.
8. After the characterization, the pump was used to create a flow and the measured cell was flash away while a new cell was brought to the characterization area.

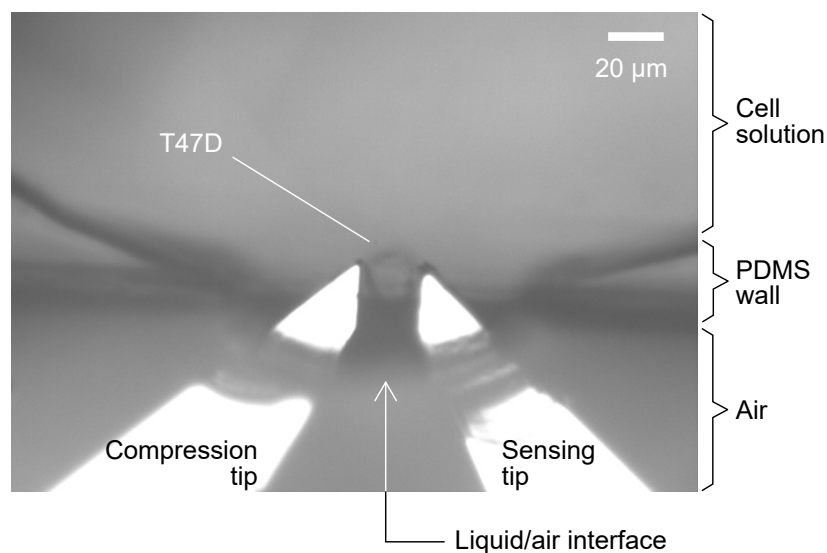


**Fig. 2.17** (a) The channel was filled with a solution, e.g., PBS. (b) Then, tips were inserted via side opening. (c) After injection, a cell was captured and analyzed.

### 2.3.5 Single cell characterization

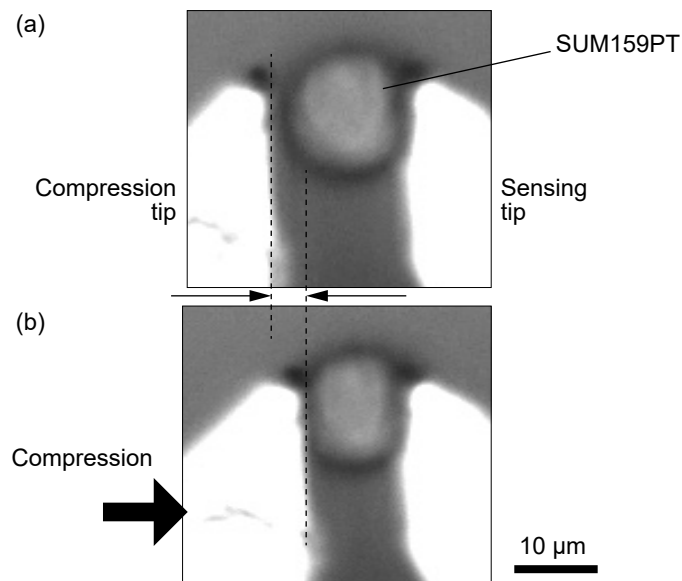
#### Capturing and handling single cells

Applying the described experimental procedure, single cells were captured between two tips that were accessing the channel *via* the side opening of the microfluidic device (**Fig. 2.18**). Both tips were penetrated through the air-liquid interface which separated the handling region of the SNT from the MEMS regions that should stay in air for optimal performance. Small dimensions, in the order of 100  $\mu\text{m}$ , of the side-opening prohibited any leakage of the liquid due to the surface tension of the liquid.



**Fig. 2.18** Microscope image of the captured cell by two SNT tips during the experiment.

The compression tip was actuated to capture a cell and applied compression cycles for mechanical characterization while the sensing tip was performing continuous real-time measurements. To provide linear compression, a square root voltage signal was required as a potential difference applied on the compression side. The compression tip can be displaced about 5.5  $\mu\text{m}$  by applying 50 V at the compression side actuator electrodes (**Fig. 2.19**). When the potential difference between those electrodes exceeded 60 V, the movable electrode of the electrostatic actuator stuck at the counter electrode.

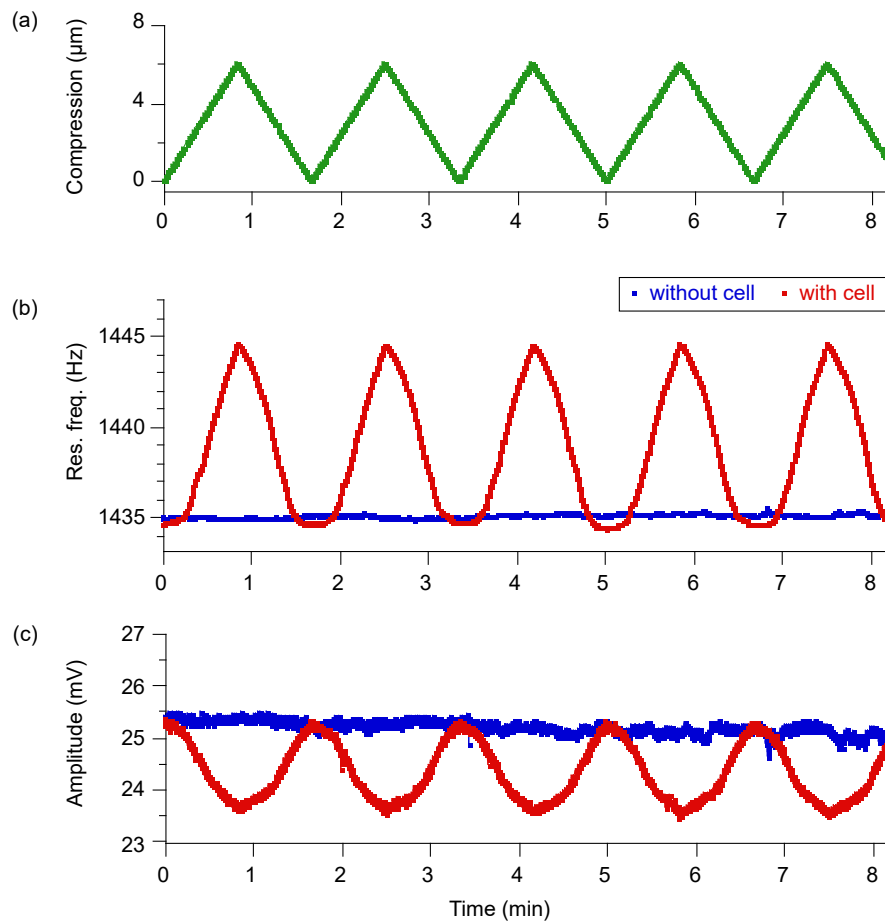


**Fig. 2.19** The captured cancer cell. (a) The initial gap before compressing the cell and (b) the compressed state of the cell.

An example of the linear compression cycles applied to a captured cell is shown in **Fig. 2.20 (a)**. One period (compression-relaxation) was 100 seconds and the signal was applied for five times. For performing single cell characterization, first, the stability of the system without any cells captured in between the tips was tested (control experiment: results are shown in blue line in **Fig. 2.20 (b)** and **(c)**). Neither the resonance frequency nor the sensor signal amplitude was affected by compression cycles even tips were inserted in the solution. Moreover, these control experiments show stable characteristics throughout the experiment.

In the same experiment with the fixed SUM159PT cell captured between the tips, the resonance characteristics (frequency and amplitude) clearly detected the effect of cell compression in real-time (red line in **Fig. 2.20 (b)** and **(c)**). The resonance frequency was increasing while the tips were compressing the captured cell (until 50 seconds of each period). In contrast, the sensor amplitude was decreasing with the cell compression. Consecutive five cell compression cycles resulted in similar responses for each time.

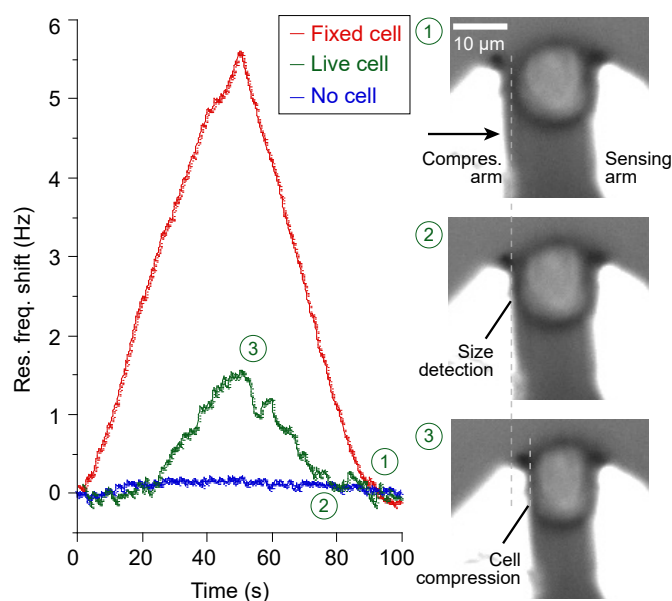
Mechanical characterization of single cells could be carried out in a few seconds to a few tens of seconds. To test the long-term stability of the detection method, the microfluidic device kept measuring mechanical properties of a cell up to 10 minutes without compromising the stability.



**Fig. 2.20** Given signal and responses during compression. (a) A linear displacement applied to the captured cell repeatedly (100 seconds periods). SNT were capable of detecting (b) resonance frequency and (c) sensor amplitude in real-time.

### Comparison between fixed and live SUM159PT cells

Mechanical responses of fixed and live SUM159PT cells were compared by applying linear compression cycles of 100 seconds period (**Fig. 2.21**). The control experiment (no-cell case) showed no increase in the resonance frequency even when a compression cycle was applied. Measured frequency shift of  $\sim 5.5$  Hz for a fixed cell (in red colour) and  $\sim 1.5$  Hz for a live cell (in green colour) show the effect of compression on cells in different states. A camera was used throughout experiments to monitor the real-time changes of a cell's shape due to the compression. The resonance frequency of the sensing tip stayed constant (**Fig. 2.21** ①–②) until the cell started to be compressed. The point where the resonance frequency began to increase was the detection point of the size of the captured cell (**Fig. 2.21** ②). Then, the captured cell was squeezed up to a predetermined level by the compressing tip (**Fig. 2.21** ②–③).



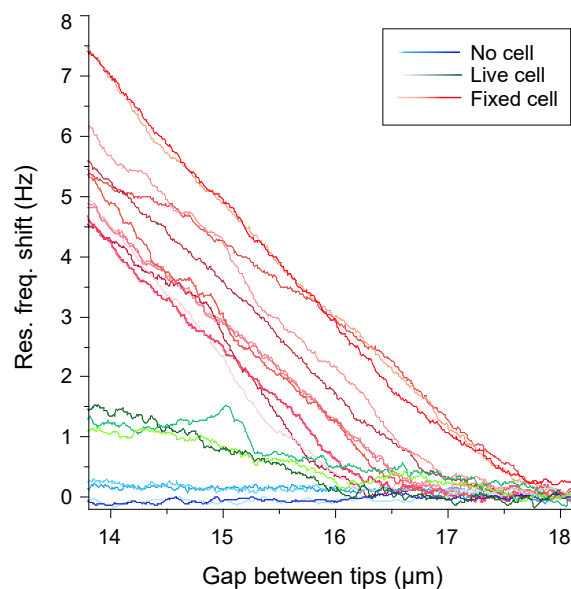
**Fig. 2.21** Applied compression cycle resulted in smaller response frequency changes for live SUM159PT cells (red) compared to fixed SUM159PT cells (green). A cell response deviated from no cell (blue) control result when the cells started to be compressed.

### Size detection of captured cells

Performing cell characterization several times, the differences could be observed between live and fixed SUM159PT cells as expected (**Fig. 2.22**). Fixed cells showed much higher resonance



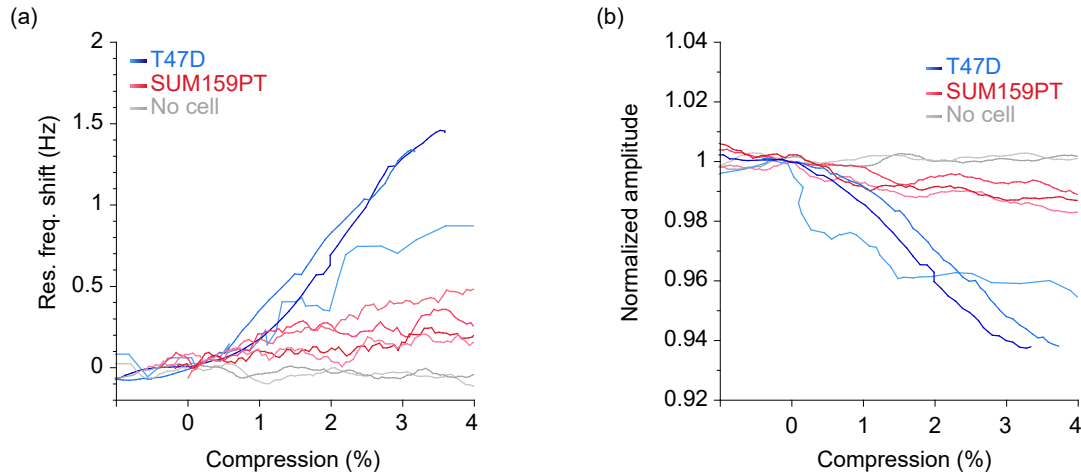
frequency shift (in red lines) when compared to the live cells (in green lines). Compared to no-cell control experiments (in blue lines), the effect of cell response can be seen clearly. Knowing the initial gap between the SNT tips and the displacement due to the comb drives actuator, the gap, when the resonance frequency was shifted from initial value, was equal to the diameter of the cell in compression. It was confirmed that the sensor output was enough to detect the cell diameter by optical verification with a camera monitoring the experiments all the time.



**Fig. 2.22** Detection of the diameter of the analyzed cell.

### Comparison between SUM159PT and T47D cells in live state

The resonance characteristics (frequency and sensor signal amplitude) of different cell lines, such as SUM159PT and T47D in live state, were compared to distinguish them (**Fig. 2.23**). The compression distance is normalized by the initial cell diameter and shown as a relative value in %. No-cell control (nothing captured in between the tips) and two different human breast cancer cell lines: SUM159PT (in reddish colours) and T47D (in bluish colours) are shown. Compared with highly malignant cells of SUM159PT, T47D had a higher resonance frequency shift of about 1.5 kHz change and normalized amplitude decrease of about 6 %.



**Fig. 2.23** The difference of resonance frequency shift and normalized amplitude by changing the compression level.

### 2.3.6 Data analysis

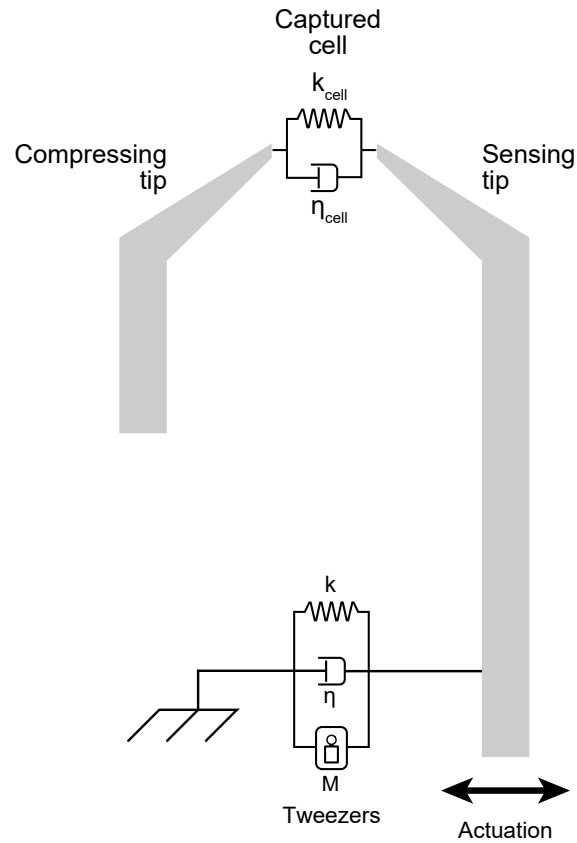
The characterization by SNT, essential to monitor the cell characteristics during compression, is based on the equivalent mass-spring-damper system, as shown in **Fig. 2.24** [79]. Response of a cell is obtained by the change of the resonance frequency and quality factor of the system (SNT + Cell). The resonance frequency,  $f_R$ , and the quality factor  $Q$  of the SNT + Cell damped oscillator are represented as follows:

$$f_R(t) = \frac{1}{2\pi} \sqrt{\frac{(k + k_{cell}(t))}{M}} \quad (2.11)$$

$$Q(t) = \frac{\sqrt{(k + k_{cell}(t)) \times M}}{(\eta + \eta_{cell}(t))} \quad (2.12)$$

where  $M$  is the mass of the movable part,  $k$  is total stiffness of springs, and  $\eta$  is the viscous losses.  $k_{cell}$  and  $\eta_{cell}$  are the time varying stiffness of the cell and viscosity of the cell due to losses. Total mass of movable part  $M$  was calculated based on the area calculation results using CleWin 4.0 software and theoretical results were shown in **Table 2.2**. The density of silicon is  $2.329 \text{ g/cm}^3$ . The back-side silicon parts for mechanical connection (while maintaining electrical isolation) of the sensing, actuating and handling elements of the front side have tapered shapes

due to the DRIE process. Decreased mass due to this issue was not considered in **Table 2.2**. However, the mass of movable part has high importance to determine the resonance frequency and the Q-factor, as shown in **Equation (2.11)** and **(2.12)**.



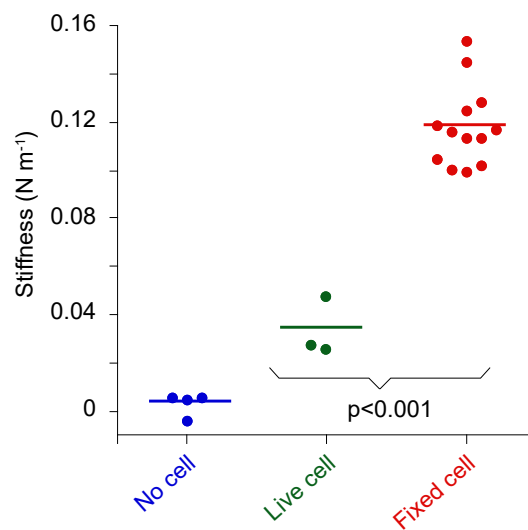
**Fig. 2.24** Equivalent dynamic model of the SNT with the cell.

**Table 2.2** Mass calculation of SNT movable part

Characteristics	Frontside	Backside	Total
Area ( $\mu\text{m}^2$ )	$4.78 \times 10^6$	$0.166 \times 10^6$	$4.946 \times 10^6$
Volume ( $\mu\text{m}^3$ )	$143 \times 10^6$	$58.0 \times 10^6$	$201 \times 10^6$
Mass (g)	$3.33 \times 10^{-4}$	$1.35 \times 10^{-4}$	468 ( $\mu\text{g}$ )

### 2.3.6.1 Comparison between fixed and live SUM159PT cells

Based on the results shown in **Fig. 2.22**, fixed and live SUM159PT cells were analyzed to obtain their stiffness N/m. Live (in green) and fixed SUM15PT cells (in red) at 10 % of the cell diameter had significant differences ( $p < 0.001$ ), as shown in **Fig. 2.25**. As a result, SNT was demonstrated to have enough sensitivity to distinguish live and fixed cancer cells.

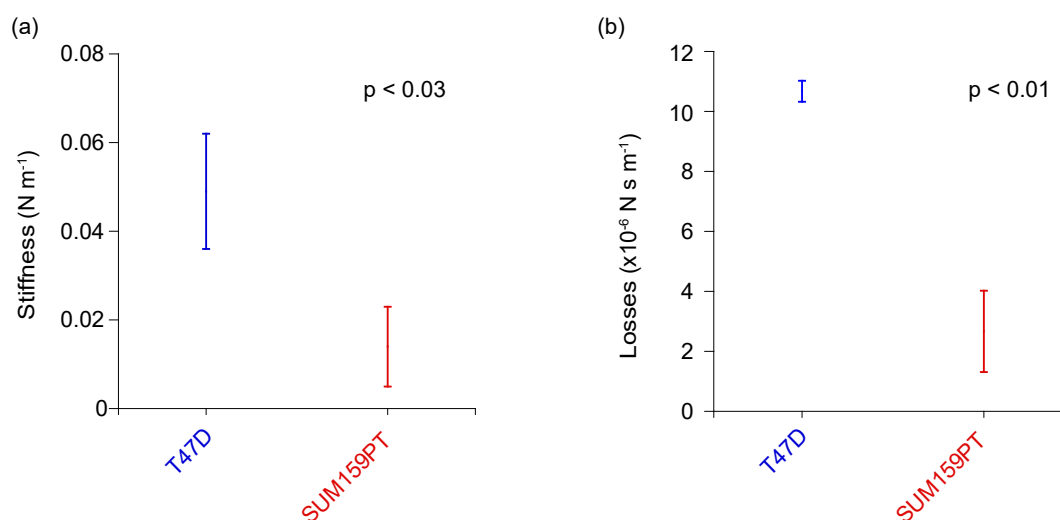


**Fig. 2.25** Measured stiffness at 10% compression was significantly different ( $p < 0.001$ ) between live (green) and fixed cells (red). No-cell condition as control experiments are also shown in same graph (blue).

### 2.3.6.2 Comparison between live SUM159PT and T47D cells

Similar to the previous section, stiffness and viscous losses analysis of live cells were carried out using experiments results shown in **Fig. 2.23** to distinguish two different cell lines. The extracted stiffness and viscous losses in two different cell lines at 3 % compression, were shown in **Fig. 2.26** (SUM159PT in red and T47D in blue). SNT used in this experiment had a large gap distance of 26  $\mu\text{m}$  which was much larger than an average cell dimension. Therefore, the cell could not be compressed up to 10 % as in the case of previous experiments due to the limit of the actuator. The stiffness value of T47D cells was detected as 2-3 times higher than SUM159PT cells in live state ( $p < 0.03$ ). SUM159PT has higher malignancy potential therefore it is not surprising for such cells to have softer characteristics that allow their migration in other tissues. Comparison of viscous losses in two different cell lines (**Fig. 2.26 (b)**) shows SUM159PT cells

demonstrating lower losses compared with T47D cells ( $p < 0.01$ ) at 3 % of cell compression level. These results indicate that T47D has higher rigidity and viscosity. To conclude, SNT could identify two different cancer cell lines in live state.



**Fig. 2.26** Extracted (a) stiffness and (b) viscous losses from resonance characteristics in two different human breast cancer cell lines.

### 2.3.7 Conclusions

Silicon Nano-Tweezers (SNT) were fabricated using the MEMS micromachining facilities in Fujita laboratory, IIS, University of Tokyo. The design of the SNT, such as the gap distance between tips, the stiffness of springs and the actuation force were adapted to perform measurements on single cancer cells.

Using SNT, fixed and live SUM159PT cells (human breast cancer cell line cells) were compared. Fixing cells protected the sample from extrinsic damage and altered cells at a molecular level to increase mechanical stability. Due to the increased strength and rigidity, the morphology (shape and structure) of cells were preserved and showed higher stiffness compared with live cells (**Fig. 2.25**).

Adapted SNT was used to compare mechanical properties of two different human cancer cell lines: T47D and SUM159PT in live state. SUM159PT has higher metastatic potential than T47D. The difference in stiffness (**Fig. 2.26 (a)**) and viscous losses (**Fig. 2.26 (b)**) of those cell

lines were shown using adapted SNTs. These differences in cell responses are expected to be linked to cells' metastatic potential.

The throughput of SNT was higher than AFM. However, the time needed to capture a cell was still much longer than the required levels to obtain statistically significant amount of data in a short time. Therefore, a new device providing much higher throughput is required.

## 2.4 Conclusions

AFM, as generally used to measure the local cell properties at the adhered state, is a time-consuming process to measure an entire cell which depends on the proficiency of the AFM operator. More importantly, AFM shows significant shortcomings for measurements on floating cells. SNT, combined with a microfluidic device, shows improved throughput and allows direct capturing and analysis of a single cell between two tips. In this chapter, the use of AFM and SNT was introduced for single cell analysis and their performance for characterizing mechanical properties of floating cells was examined.

AFM approach was modified with the use of PDMS microwells to keep floating cells steady during indentation tests. Live cancer cells were captured in these wells to perform single cell indentation tests. Beforehand, cancer cells were stained and sorted in two as CSC and non-CSC by a cell sorter. The number of measured cells varied for each sorting process. The Young's modulus (used as mechanical stiffness of cells) also showed variations even within the same population of CSC. Possible causes include: (1) variations in dimensions of both cells and microwells. (2) cells not reaching (contact) the bottom surface of the well and the constant compression not given to cells even if the AFM indentation test was performed for a constant distance compression. (3) cells beginning to deform as the measurement time was long. Due to the installation conditions of the AFM, it took time to find a cell suitable for the indentation test *via* the small measurement field of view.

Several design parameters of SNT were optimized (gap distance, actuation force, spring constant, etc.) to use for cancer cell measurement. Firstly, fixed and live SUM159PT cells were prepared to examine the resolution of detection in real-time. Due to the increased strength and rigidity by fixation process, mechanical properties of cells showed higher stiffness compared with live cells. Next, two types of cell lines with different metastatic characteristics (SUM59PT and T47D) were prepared to measure their mechanical properties. As a result, SNT could distinguish two different cell lines based on their mechanical properties. Some parameters such as spring constants on both compression and sensing side, the actuation force, and the resolution of cell detection were optimized by SNT that can be applied to the proposed new device. However, the throughput obtained with SNT approach was still far from providing the statistically significant amount of information. Although the measurement capabilities were adequate, a new approach for cell handling to achieve high-throughput was essential.

# Chapter 3

## Development of a built-in channel device for single cell biophysical characterization

### 3.1 Introduction

**Chapter 3** explains the development of a novel device based on combining the MEMS device and the microfluidic device proposed in the previous chapter for measuring physical properties of cells in suspension. The design principles, fabrication steps, and performance evaluation of this new MEMS device to improve the throughput (measurement speed) will be examined. In the new device, MEMS elements and a microfluidic channel which is embedded in the device layer are all integrated in the silicon device. A flow controls the cell motion inside a microfluidic channel and brings the cell to a characterization area where tips are positioned to capture and compress the cell. Mechanical measurements (as in the case of SNT) and electrical measurements can be performed simultaneously on the captured cell. Improved efficiency in measurements increases the throughput.

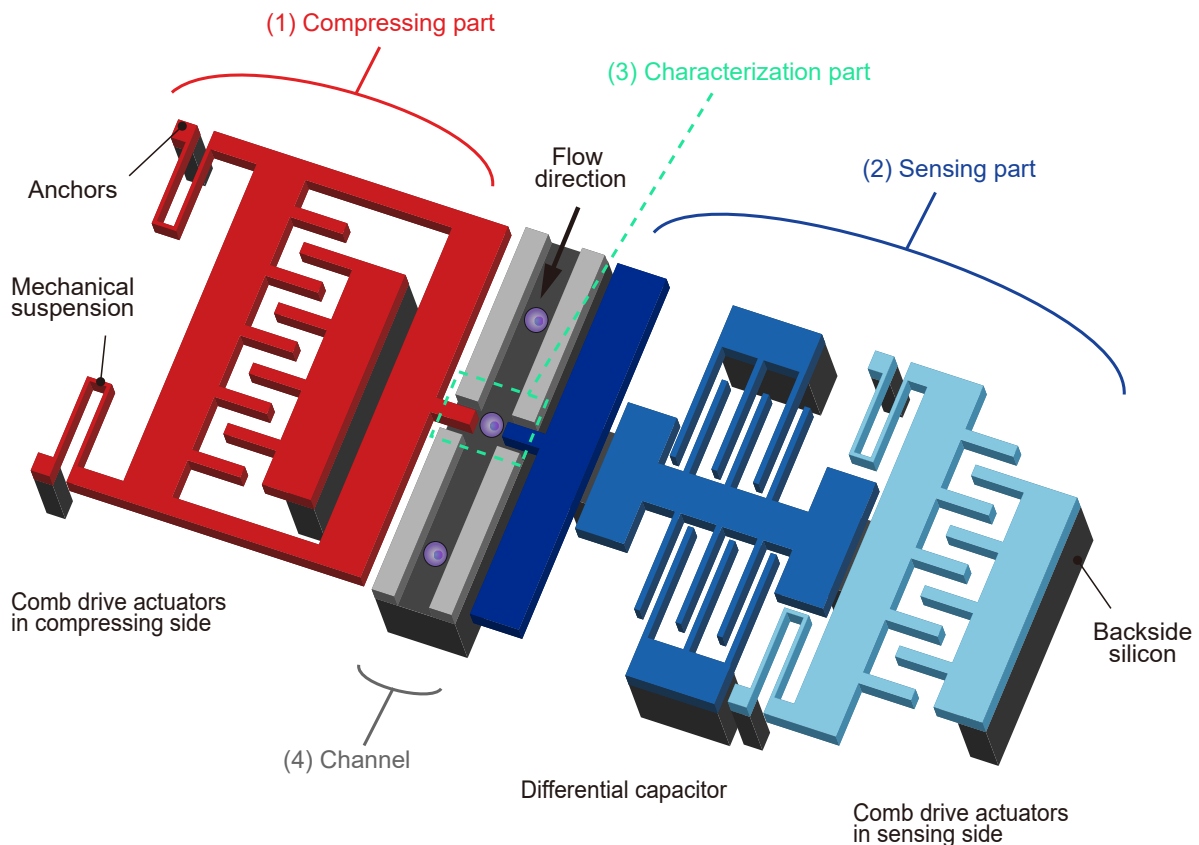
**Section 3.2** explains the basic concept and the design parameters of the proposed device. The basic MEMS structure is based on the same working principle as the SNT examined in **Chapter 2**. In addition to this, the main difference and difficulty is to integrate the microfluidic channel in the MEMS device to provide a stand-alone device with fully-integrated MEMS and microfluidic elements. Various design parameters are examined to obtain a better fit for cancer cell measurements, e.g., the spring constant, the suspension shape, and the comb tooth design. **Section 3.3** describes the details of device fabrication. Although both MEMS and microfluidics elements are fabricated on a single device, a PDMS cover is also used to complete the channel and provide fluidic inlets and outlets. The silicon device was fabricated at the



University of Tokyo, Japan, and brought back to France. In **Section 3.4**, the working principle of the fabricated device and the setup of the experiment are explained to show the capacity of high-throughput measurements and different means of characterization (mechanical and electrical) of non-adherent cells. Before carrying out cell experiments (to be described in **Chapter 4**), the performance of the fabricated device is evaluated, in **Section 3.5**, in solutions of different properties for frequency response, and real-time mechanical and electrical measurement.

## 3.2 Working principle and design

### 3.2.1 Principle



**Fig. 3.1** Schematic image of the proposed device with embedded microfluidic channel.

As detailed in **Chapter 1**, numerous methods have been used to examine the biophysical properties of single cells. However, the majority of these methods, such as AFM, can be applied solely for the study of adherent cells. Techniques to analyze non-adherent cells, such as CTC and CSC, are limited. Moreover, there is a trade-off between throughput and information content.

Using biophysical properties for practical routine tests to distinguish cells in a sample solution requires both high-throughput and multi-parameter analysis. Three main features necessary for the targeted practical system are (i) the high-throughput handling of non-adherent cells, (ii) high-sensitivity detection and (iii) simultaneous multi-parameter analysis. Although the main principle is similar to the SNT, the throughput of the proposed device would be much higher than that of SNT due to the integrated built-in channel. Thus, the proposed device can achieve a much more efficient use of MEMS and microfluidics.

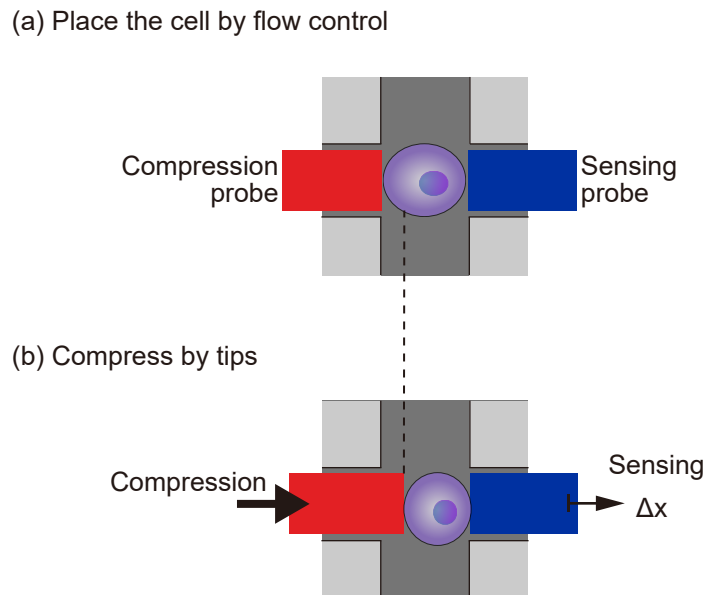
The proposed device allows low-noise electrical detection while providing mechanical and electrical stimulation of cells, similar to the SNT. However, by directing the cell to the characterization area, the initial setup and the capturing protocol of a cell is significantly simplified.

The proposed single cell characterization device consists of four main components as shown in **Fig. 3.1** and details of each part are as follows:

1. Compression part, a series of electrostatic comb drive actuators to perform compression of the cell (show in red),
2. Sensing part, a differential capacitive sensor for displacement measurements. This sensor is connected to a second electrostatic comb drive actuator for harmonic measurements (show in blue),
3. Characterization part, two opposing tips integrated in a microfluidic channel to compress and characterize the single cell (show in surrounded light green dotted line),
4. Microfluidic channel, a flow is created in the channel (show in gray) to handle the cell solution by a vacuum pump connected to the outlet.

Adjusting the vacuum pump pressure enables control of the flow rate, which allows for single cell positioning at the characterization area between tips as shown in **Fig. 3.2**. One tip, connected to an electrostatic actuator for quasi-static displacement (shown in red), is used for compressing cells, whereas the other (shown in blue) is used for harmonic sensing of the mechanical properties of cells under various compressive strain values with a displacement sensor based on differential capacitors. Microfluidic channel, a flow is created in the channel (show in gray) as detailed in the following sections. After being introduced *via* the inlet, a cell is positioned at the characterization area for opposing tips to perform single cell mechanical/electrical characterization. By controlling the flow rate, the captured cell can then be washed away to receive the next cell to characterize.

These key features allow the proposed device to perform high throughput measurement and multi-parameter analysis on cells in suspension.



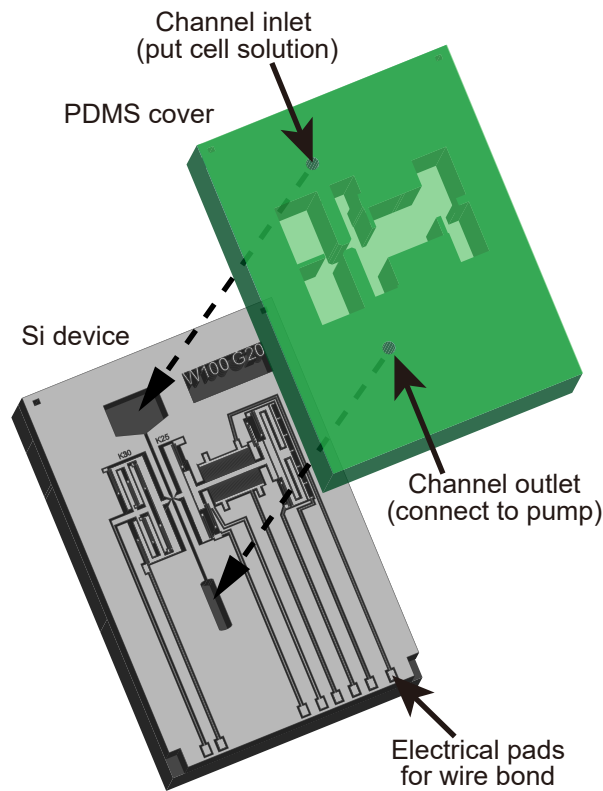
**Fig. 3.2** Schematic view of a close-up view of the tips at the characterization part. **(a)** Placing a cell between tips by flow control. **(b)** Applying compression cycles to the captured cell by moving the tip.

### 3.2.2 Design description

This device is composed of a silicon (MEMS/microfluidics) layer and a polydimethylsiloxane (PDMS) layer, as shown in **Fig. 3.3**. The MEMS layer is fabricated on a silicon-on-insulator (SOI) wafer. The top silicon of the wafer forms the functional parts of the proposed device (**Fig. 3.1**). In addition to serving as the handling layer of the device, the bottom silicon (backside silicon) has two other functions:

- (i) providing mechanical connection between electrically isolated elements of the sensing part,
- (ii) completing the microfluidic channel together with the PDMS layer.

The functionality of the device is achieved through the combination of four distinct areas as follows.



**Fig. 3.3** Schematic view of the channel integrated MEMS device and polydimethylsiloxane (PDMS) cover alignment.

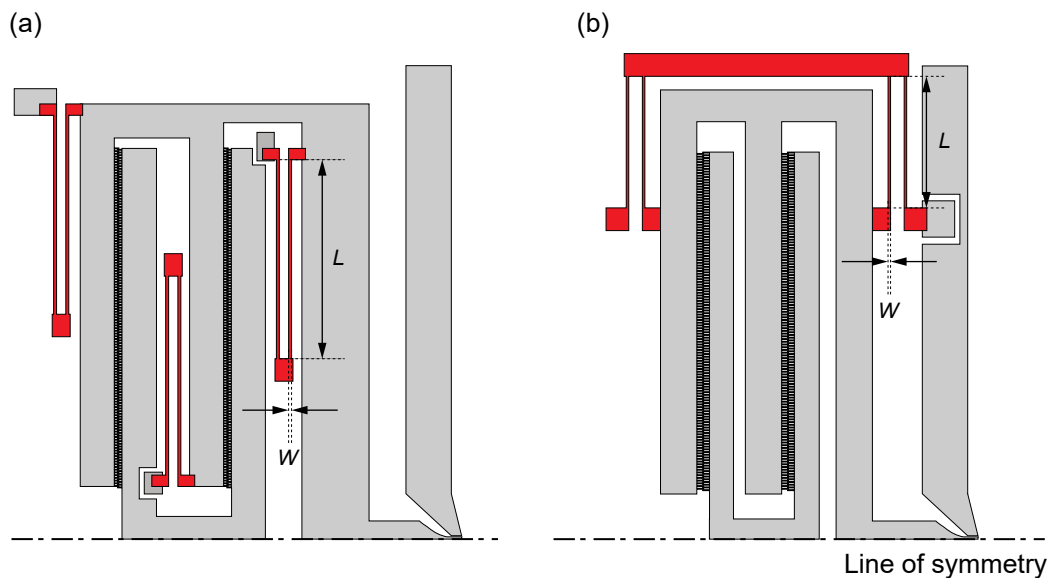
### 1. Compression part

The compressing side consists of a series of electrostatic comb drive actuator, which provides the necessary motion of the compressing tip. Depending on the dimension of the targeted cells, the displacement requirement for the actuator varies. Therefore, various designs with different spring geometries, spring constants, and actuator teeth dimensions were tested. In design (1), folded beam springs, as in the case of SNT, is used [74]. In (2) and (3) double folded beam (DFB) springs are implemented to allow longer displacement in  $x$ -direction with higher stability in  $y$ -direction as was discussed in **Subsubsection 2.3.2.4** [105],[106]. Especially in design (3), long comb teeth are introduced (DFB-L) to achieve longer displacement. Details are summarized in **Table 3.1**.

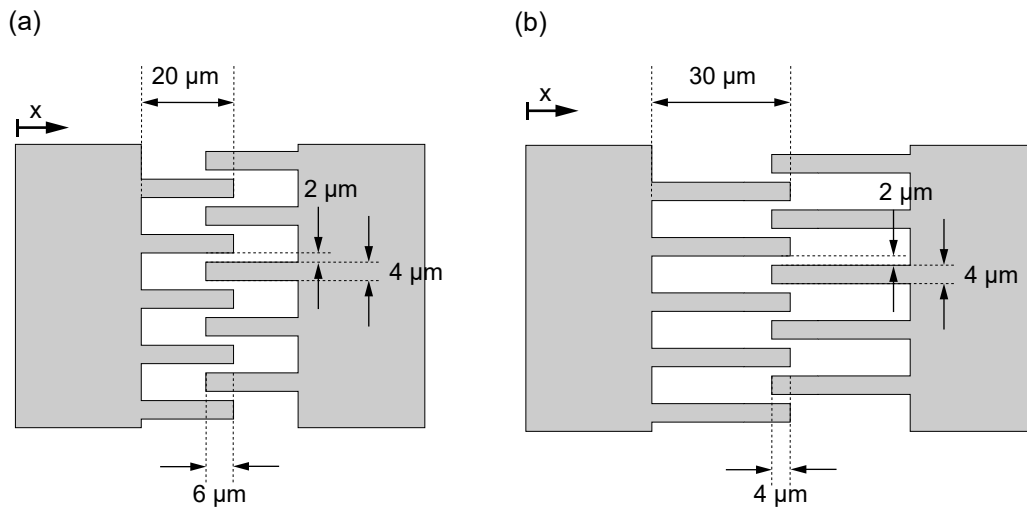
**Table 3.1** Main parameters of device designs

	U-shaped	DFB	DFB-L
Dimension ( $L \times w$ ), $\mu\text{m}$	$877 \times 12$	$580 \times 10$	$580 \times 10$
Thickness, $\mu\text{m}$	30	30	30
Spring constant $k_l$ , N/m	5	10	10
Total spring constant $k_L$ , N/m	30	40	40
Number of springs	6	4	4
Number of pairs per comb	125	125	125
Total comb teeth	1000	1000	1000
Comb tooth length, $\mu\text{m}$	20	20	30
Overlap, $\mu\text{m}$	6	4	4
Gap distance between opposite teeth, $\mu\text{m}$	2	2	2

Two different spring designs such as the folded beam (U-shaped) spring and the double folded beam (DFB) spring are adopted here (**Fig. 3.4**). Also, in order to obtain a long displacement in  $x$ -direction, different dimensions of comb teeth are designed (**Fig. 3.5**). Four groups of comb drives with 250 teeth per group (total number of comb teeth is 1000) provide actuation. Each tooth is designed to have a width of  $4 \mu\text{m}$ . A pitch of  $8 \mu\text{m}$  between each tooth results in a gap of  $2 \mu\text{m}$  between two complimentary opposing teeth.



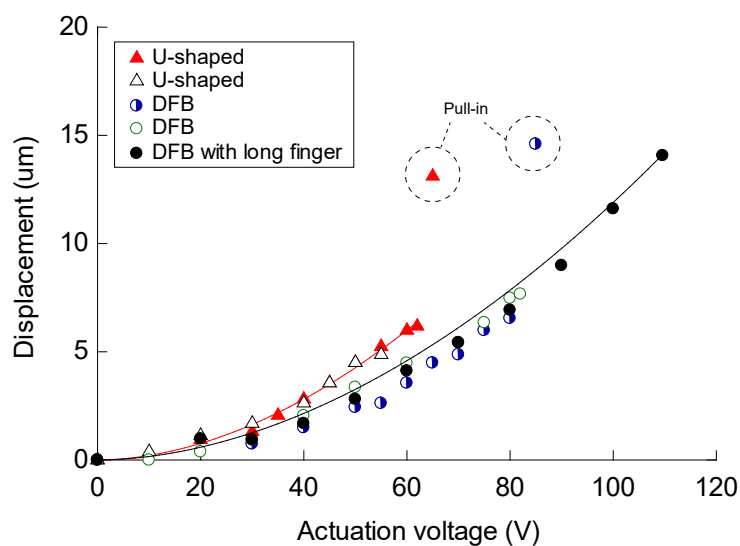
**Fig. 3.4** Schematic image of two different spring geometry. (a) U-shaped spring. (b) Double folded beam (DFB) spring.



**Fig. 3.5** Design of comb drive teeth. **(a)** Design for an U-shaped spring device. **(b)** Design for DFB (with long displacement) device.

**(I) Folded beam (U-shaped) springs** (same as SNT)

The spring constant value ( $k_L = 30 \text{ N/m}$ ) of SNTs for folded beam (U-shaped) springs is used in the design of the proposed device (**Fig. 3.4 (a)**). As this mechanical suspension has already supported actuation well in the SNT, and larger displacement can be obtained at lower actuation voltages (**Fig. 3.6**), adopting the same design guarantees successful actuation in the new device. Therefore, the fabrication processes and design parameters can easily be adopted.



**Fig. 3.6** Characteristics of actuation on various spring designs.

The dimensions of U-shape springs were redesigned in order to improve the yield of device during the fabrication process. Six sets of mechanical suspensions with the total spring constant value of  $k_L = 30 \text{ N/m}$  were used in the design of SNT. The required ratio between the beam width of spring ( $w = 12 \text{ }\mu\text{m}$ ) and the length of the beam ( $L = 877 \text{ }\mu\text{m}$ ) is derived using **Equation (2.3)**. From these values, the spring constant becomes:

$$k_l = 5.04 \approx 5 \text{ N/m},$$

The electrostatic actuator was designed to have a comb tooth dimension of  $20 \text{ }\mu\text{m}$  long teeth with  $6 \text{ }\mu\text{m}$  of overlap between opposing teeth (**Fig. 3.5 (a)**). The gap between parallel plate is  $8 \text{ }\mu\text{m}$  and the tooth width is  $4 \text{ }\mu\text{m}$ . Thus, distance from counter electrode teeth is  $2 \text{ }\mu\text{m}$ .

The actuation force in  $x$ -direction  $F_x$  with U-shaped springs is obtained from **Equation (2.6)** as follows:

$$F_x = 66.4 \times 10^{-9} \times V^2$$

Theoretically, this U-shaped spring can reach  $5.5 \text{ }\mu\text{m}$  at  $50 \text{ V}$ . The actual SNT experiment explained in **Section 2.3** showed that the electrostatic comb drive actuator stuck to the counter comb teeth due to the instability of the actuator when applied voltage exceeded  $60 \text{ V}$ . This phenomenon occurred when the force exceeded the restoring force of the mechanical suspension. However, some applications require larger displacement in direction depending on the dimension of target cells. Thus, an alternative spring shape, that has the feature of both larger displacement in  $x$ -direction and stronger in  $y$ -direction, was needed.

## (II) Double folded beam (DFB) springs

A wider displacement range is essential for cells with highly variable diameters. Four sets of double folded beam (DFB) spring design with the total spring constant of  $k_L = 40 \text{ N/m}$  provides highly stable characteristics in terms of  $y$ -direction displacement **Fig. 3.4 (b)**. Obtaining an overall spring constant of  $k_L = 40 = 4 \times k_l \text{ N/m}$ , dimensions of DFB is designed as  $w = 10 \text{ }\mu\text{m}$  in width and  $L = 580 \text{ }\mu\text{m}$  in length. From this, spring constant of one spring is calculated as follows:

$$k_l = 10.07 \approx 10 \text{ N/m}$$

Therefore, the spring dimension of  $20 \text{ }\mu\text{m}$  in teeth length,  $4 \text{ }\mu\text{m}$  in overlap and  $16 \text{ }\mu\text{m}$  in the initial gap distance are adopted to achieve a displacement  $\geq 10 \text{ }\mu\text{m}$ .

Obtained actuation force  $F_x$  is calculated with **Equation (2.6)**. The equation is derived from the vacuum permittivity, the Young's modulus of Si, the thickness of device, total number of teeth, and gap distance between counter electrodes. This value is the same in all compression part designs. Therefore, the actuation force is calculated as:

$$F_x = 66.4 \times 10^{-9} \times V^2$$

If the actuation voltage is applied at  $V = 50$  V, since then the displacement of  $\Delta x$  can be calculated at around  $4.2 \mu\text{m}$  by using the following equations:  $F_x = 16.6 \times 10^{-4}$  N and  $F = kx$ . From this, the comparison between U-shaped and DFB at the same applied voltage of 50 V shows that the microactuator with U-shaped springs has a larger displacement (around  $5.5 \mu\text{m}$ ) at lower voltage. However, if the voltage applied at 80 V, the actuation force is derived as  $F_x = 4.25 \times 10^{-4}$  N and the displacement of  $\Delta x$  is  $10.6 \mu\text{m}$ . The actual actuation characteristics are shown in **Fig. 3.6**.

### (III) Double folded beam springs with long teeth (DFB-L)

Dimensions of comb drive teeth are revised to obtain a much longer displacement, such as  $15 \mu\text{m}$ . The length of a comb tooth is designed as  $30 \mu\text{m}$  with an overlap length between opposing teeth as  $4 \mu\text{m}$ , and the initial gap distance between teeth as  $26 \mu\text{m}$  (**Fig. 3.5 (b)**). Other parameters, such as the spring constant and the arrangement of mechanical suspensions are adopted from the design described above (2). In theory, applying 110 V between the electrodes results in a displacement  $\Delta x$  of  $16.6 \mu\text{m}$ .

## 2. Sensing part

The sensing part, which is shown in **Fig. 3.1**, consists of three elements as follows:

- (1) a series of comb drive actuator providing the necessary vibrating motion of the sensing tip,
- (2) a capacitive sensor for displacement sensing,
- (3) a sensing tip to access the characterization area.

These elements are mechanically connected while kept isolated electrically to provide optimal simultaneous mechanical and electrical sensing.



The comb-drive actuators are driven by a lock-in amplifier while the phase is locked based on the output of the displacement sensor for resonance mode. The movable elements of the sensing part are suspended with 6 folded beam (U-shaped) springs. Two different U-shaped springs are designed to provide different stiffness: 5 N/m and 25 N/m. **Table 3.2** shows the details of designed springs. The stiffer design of 25 N/m provides enough sensitivity for measurements with harmonic oscillations while static measurements would benefit from the higher sensitivity of the softer design in 5 N/m.

**Table 3.2** Details of folded beam spring in sensing part

	U-shaped: $k_R$ 25	U-shaped: $k_R$ 5
Dimension ( $L \times w$ ), $\mu\text{m}$	$850 \times 11$	$900 \times 6.7$
Thickness, $\mu\text{m}$	30	30
Spring constant $k_I$ , N/m	4.2	0.8
Total spring constant $k_L$ , N/m	25	5
Number of springs	6	6
Total comb teeth	567	567
Comb tooth length, $\mu\text{m}$	20	20
Overlap, $\mu\text{m}$	4	4
Gap distance between opposite teeth, $\mu\text{m}$	2	2

Similar to the electrostatic actuator in the compression part, 567 teeth of the comb drive actuator provide motion for harmonic detection. Each tooth is designed to have the same dimensions as the compressing side: a tooth width of 4  $\mu\text{m}$ , a tooth length of 20  $\mu\text{m}$ , a gap of 2  $\mu\text{m}$  and an overlap of 4  $\mu\text{m}$  between two consequent opposing teeth.

The actuation force  $F_x$  is obtained from **Equation (2.6)**,

$$\begin{aligned}
 F_x &= \frac{1}{2} \times 8.854 \times 10^{-12} \times 567 \times \frac{30 \times 10^{-6}}{2 \times 10^{-6}} \times V^2 \\
 &= 37.7 \times 10^{-9} \times V^2
 \end{aligned}$$

with the vacuum permittivity of  $\epsilon_0 = 8.854 \times 10^{-12}$  F/m, the thickness  $t$ , the actuation voltage  $V$ , the gap between two opposing tips  $g$ , and the total number of comb teeth  $n$ . The sensing tip is actuated with amplitude of only 0.2  $\mu\text{m}$  during normal use (3  $V_{\text{p-p}}$  actuation voltage).

Forty pairs of teeth at one side form parallel plate capacitors. A tooth of the capacitive sensor has a length of 575  $\mu\text{m}$  and a width of 10  $\mu\text{m}$ . The movable electrode is designed to have a gap of 5  $\mu\text{m}$  between both fixed electrodes with an overlap of 550  $\mu\text{m}$  [74],[87]. The dimensions of the capacitor are summarized in **Table. 3.3**.

**Table 3.3** Dimension of the capacitive sensor

Parameters	Dimensions
Parallel plate ( $L \times w$ ), $\mu\text{m}$	$575 \times 10$
Thickness, $\mu\text{m}$	30
Overlap, $\mu\text{m}$	550
Initial gap, $\mu\text{m}$	40
$d_0$ , $\mu\text{m}$	5
$d_1$ , $\mu\text{m}$	25
Number of combs pairs	40

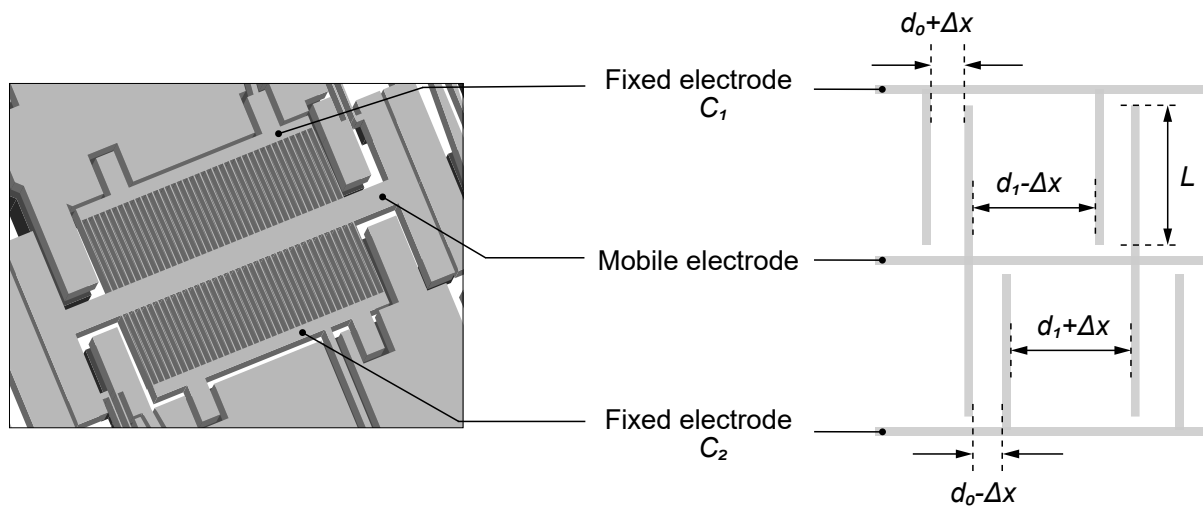
Working in differential mode, the gap between one of the electrode pair increases ( $C_1$ ), while the gap between the other electrode pair decreases ( $C_2$ ) during measurements, as shown in **Fig. 3.7**. Differential capacitances  $C_1$  and  $C_2$ , that difference of  $\Delta C$ , is related to the displacement of  $\Delta x$ . The capacitance differences  $\Delta C$  is calculated as following functions:

$$\Delta C = C_2 - C_1 \quad (3.1)$$

$$\Delta C = \epsilon_0 n L t \left[ \left( \frac{1}{d_0 - \Delta x} + \frac{1}{d_1 + \Delta x} \right) - \left( \frac{1}{d_0 + \Delta x} + \frac{1}{d_1 - \Delta x} \right) \right] \quad (3.2)$$

where  $\epsilon_0$  is the vacuum permittivity,  $n$  is the number of pairs of comb electrodes,  $L$  is the length of electrode,  $t$  is the device thickness,  $d_0$  is the initial gap between electrodes, and  $d_1$  the initial distances between repeating combs. The equation finally becomes:

$$\begin{aligned} \Delta C &\simeq 2 \epsilon_0 n L t \left( \frac{1}{d_0^2} + \frac{1}{d_1^2} \right) \Delta x \quad (3.3) \\ &= 2 \times 8.854 \times 10^{-12} \times 40 \times 575 \times 10^{-6} \times 30 \times 10^{-6} \\ &\quad \times \left( \frac{1}{(5 \times 10^{-6})^2} - \frac{1}{(40 \times 10^{-6})^2} \right) \Delta x \\ &= 481 \times 10^{-9} \times \Delta x \end{aligned}$$



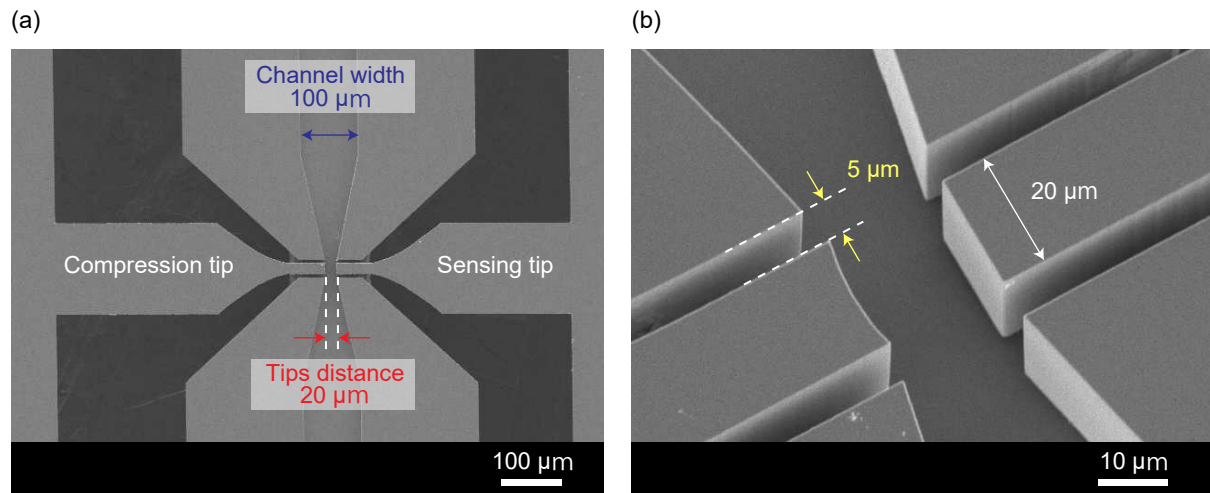
**Fig. 3.7** Differential capacitive sensor. The schematic image illustrates displacement sensing through  $C_1$  and  $C_2$  variation.

Being initially identical, the difference between  $C_1$  and  $C_2$  is 0 until the sensing tip moves. The differential capacitances are connected to the lock-in amplifier *via* two current-to-voltage (A/V) preamplifiers (Model 5182, Signal Recovery, AMETEK, Inc., Berwyn, PA, USA).

### 3. Microfluidic channel

The characterization area consists of a channel formed by the frontside silicon ( $30\ \mu\text{m}$ ) of the SOI wafer as sidewalls, the backside silicon of the SOI wafer as the bottom surface, and the PDMS slab as the top surface. The width of the channel is  $100\ \mu\text{m}$  with a narrower portion of  $20\ \mu\text{m}$  between the actuation and sensing tips, as shown in **Fig. 3.8**. The PDMS is covered entire device except around the characterization part and movable parts. The contact area between the PDMS and the MEMS surface is shown in green colour in **Fig. 3.9**.

The microfluidic channel is accessed by four openings: an inlet and an outlet in the PDMS slab to handle the liquid in the channel (**Fig. 3.3**) and two side openings at the sidewalls for inserting the compression and sensing tips. The inlet and outlet openings in the PDMS are formed using biopsy punches ( $1\ \text{mm}$  for the inlet and  $0.5\ \text{mm}$  for the outlet) and thus, do not require any specific designs. Injection to the inlet is performed using a micropipette, while the outlet is connected to the pump with a tube.

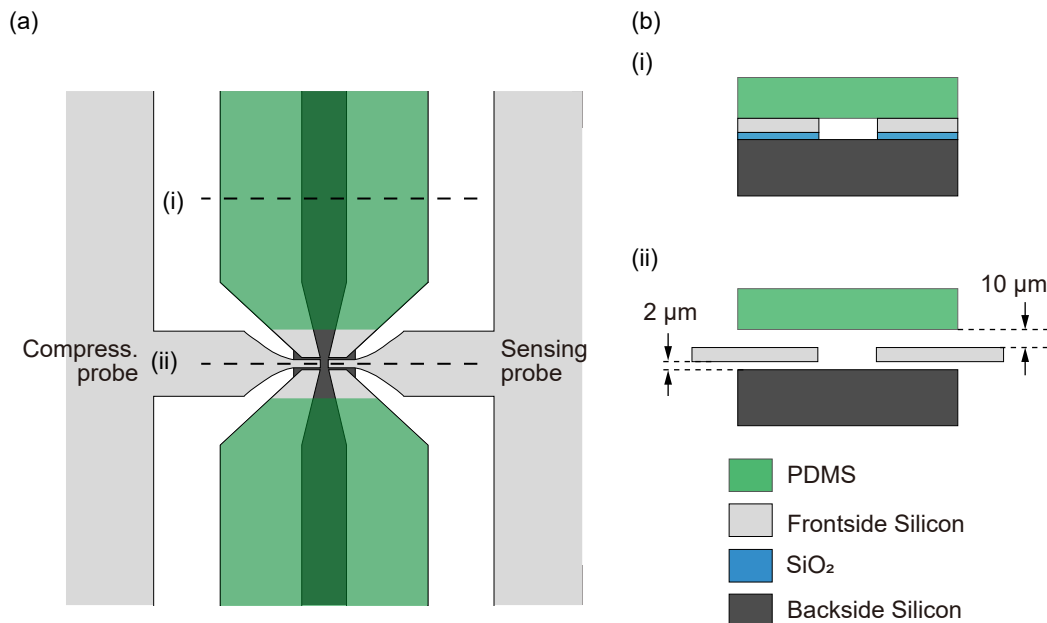


**Fig. 3.8** Scanning electron microscope (SEM) image of the (a) microfluidic channel around characterization part, and (b) embedded compression and sensing tips.

#### 4. Characterization part

The side openings for the actuating and sensing tips, on the other hand, are fabricated on the SOI wafer and require careful design consideration (**Fig. 3.8**). Excessively wide openings may compromise detection sensitivity, while a very narrow opening will cause fabrication difficulties. The objective is to prevent liquid within the channel from leaking out of the backside silicon layer border forming the channel. Ultimately a gap of 5  $\mu\text{m}$  between the sidewalls and the tips was chosen (**Fig. 3.8 (b)**). This value is similar to some previous studies using actuation at an air-liquid interface [104]. Another trade-off for a design parameter is related to the width of the tips themselves. The width was chosen as 20  $\mu\text{m}$  to be comparable with the targeted cell dimensions. Larger tip width could improve cell-capturing efficiency, however, etching the  $\text{SiO}_2$  layer under the tips would be more difficult.

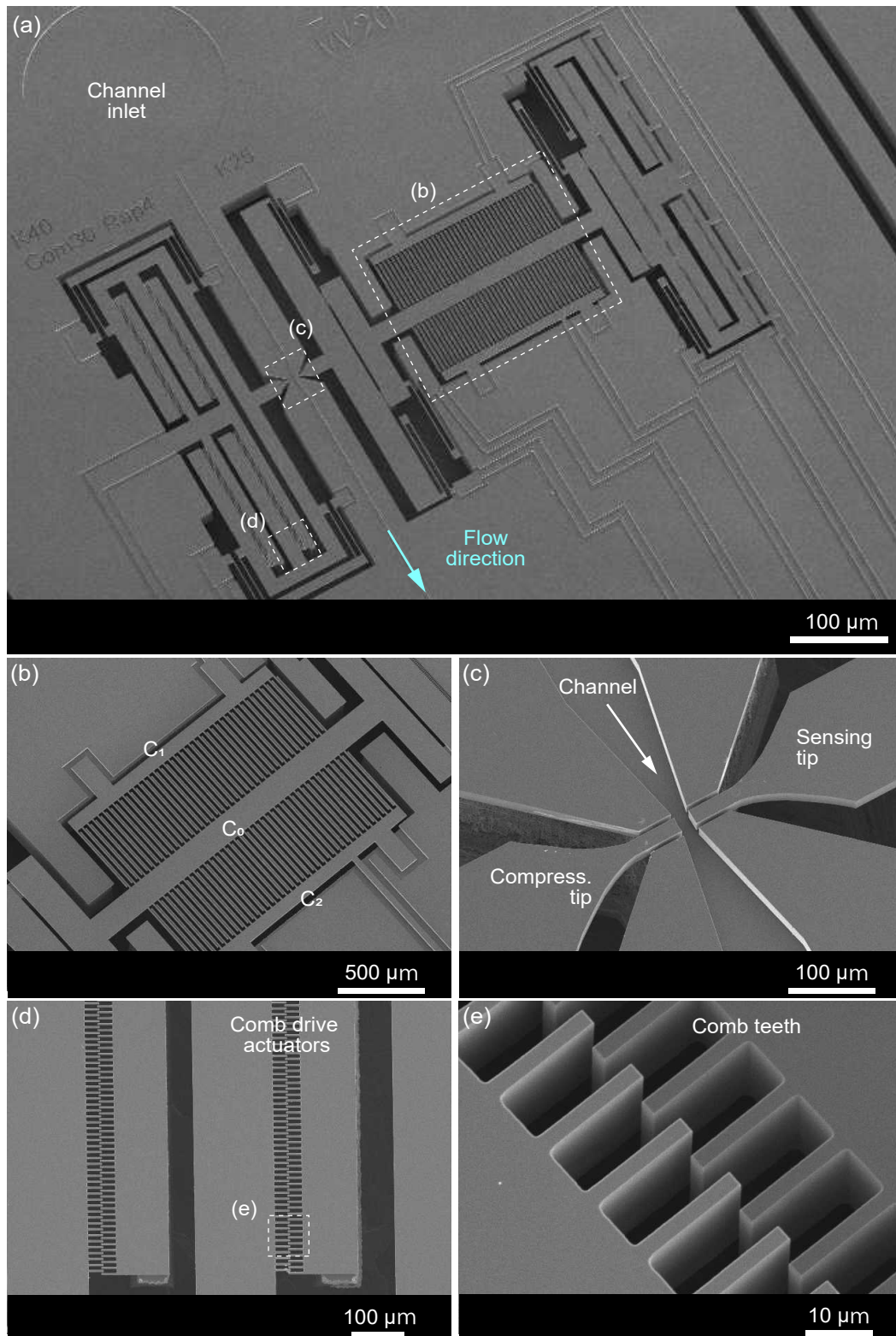
As both compression and sensing tips need to be movable, the PDMS surface above the characterization area is 10  $\mu\text{m}$  above the top of the sidewalls, preventing any contact with the actuating elements (**Fig. 3.9 (a)**). The tips are free to move after the oxide layer between the frontside and backside silicon of the SOI wafer is removed (**Fig. 3.9 (b-ii)**). The width of the elevated PDMS area is designed as 500  $\mu\text{m}$  to allow for simple alignment of the two layers.



**Fig. 3.9** A close-up view of the microfluidic channel schematic image around characterization area. **(a)** Top view shows the attachment area between the PDMS cover and the MEMS device surface (in green). **(b)** The side view shows two different cross-sections: (i) Formed channel between the MEMS device and the PDMS cover is completely closed apart from (ii) the characterization area where removal of SiO<sub>2</sub> layer and the higher PDMS bottom surface allow movable parts of MEMS device to move freely.

### 3.3 Fabrication

The details of fabrication process are described in **Appendix E**. By using the detailed fabrication process, the silicon based MEMS device was also fabricated in Fujita Laboratory's clean room at IIS, the University of Tokyo. The fabrication process is based on Silicon-on-insulator (SOI) technology. The SOI wafer used in the fabrication process had the following characteristics: (100) oriented either N type or P type of 30 μm Si frontside (top layer)/ 2 μm buried oxide (BOX) insulator/ and 350 μm Si backside (handle layer) (UltraSil Corporation, CA, USA). **Fig. 3.10** shows SEM images of a fabricated device.

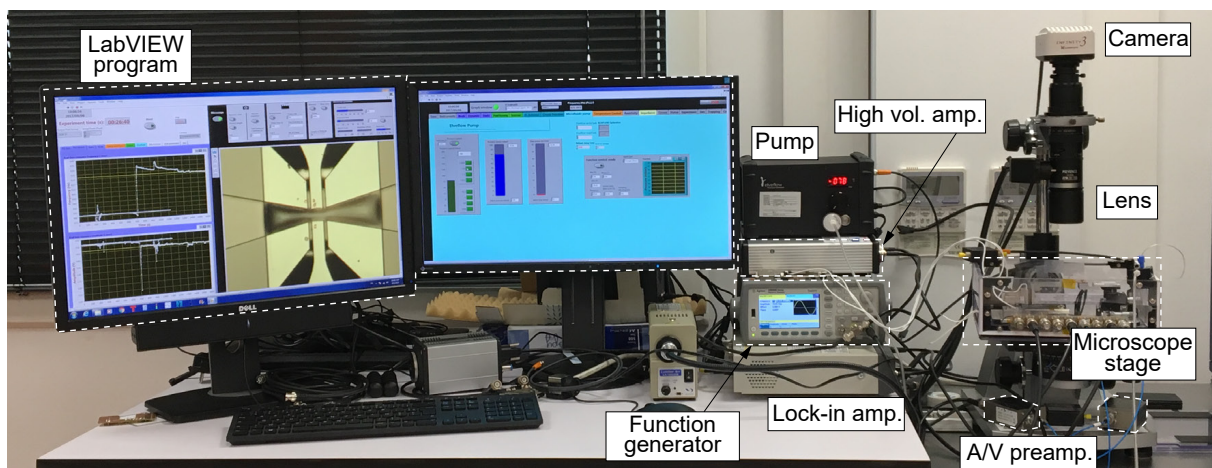


**Fig. 3.10** SEM images of the fabricated device. (a) An overview of the device. (b) Displacement sensor based on differential capacitors. (c) Opposing tips accessing the characterization part. (d) Electrostatic comb drive actuators. (e) A close-up view of combs.

## 3.4 Experimental setup

### 3.4.1 Setup

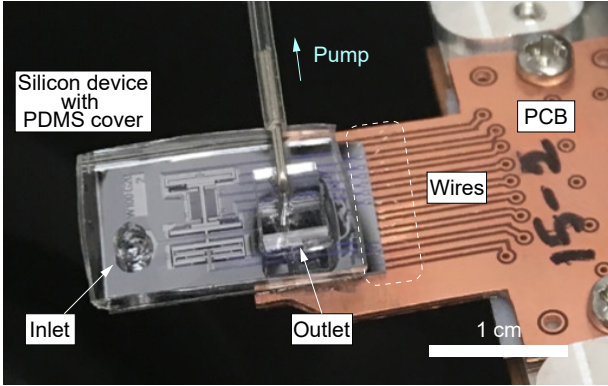
Here, the experimental setup used for evaluating the mechanical and electrical detection of the developed device is explained (**Fig. 3.11**). Experiments were performed on an upright microscope stage (VH-S30B, Keyence Corporation, Osaka, Japan). A long-working distance objective (VH-Z50L, Keyence Corporation) and a camera (Infinity 3, Lumenera Corporation, Ottawa, ON, Canada) were used to monitor the experiments. The fabricated devices were connected to peripheral electronics and the fluidic equipment, which were controlled and driven by a LabVIEW (version 16, National Instruments Corporation, Austin, TX, USA) program. Prior to positioning on the microscope stage, the assembled device was mounted on a printed circuit board (PCB) and connected with aluminum wires (**Fig. 3.12**).



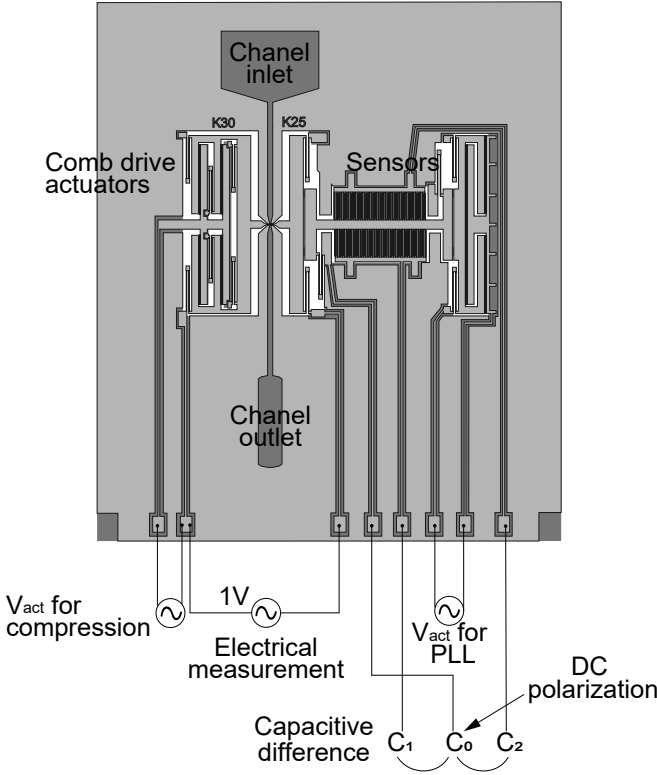
**Fig. 3.11** Photograph of experimental setup.

**Fig. 3.13** illustrates a schematic view of electrical connections of the device. Actuating the compressing tip requires applying a potential difference between the combs of the electrostatic actuator. This potential difference was provided with a function generator (33500B, Keysight Technologies Inc., Santa Rosa, CA, USA) and a high voltage amplifier (WMA-100, Falco Systems BV, Katwijk aan Zee, The Netherlands) to maintain higher voltages. As one of the actuation electrodes was also used for electrical sensing, this electrode was grounded virtually by the transimpedance amplifier needed for electrical measurements and the actuation signal is applied on the other electrode.





**Fig. 3.12** A close-up photograph of the channel integrated MEMS device and PDMS cover assembled on a printed circuit board (PCB) and installed in the setup.



**Fig. 3.13** Schematic view illustrating electrical connections of the device.



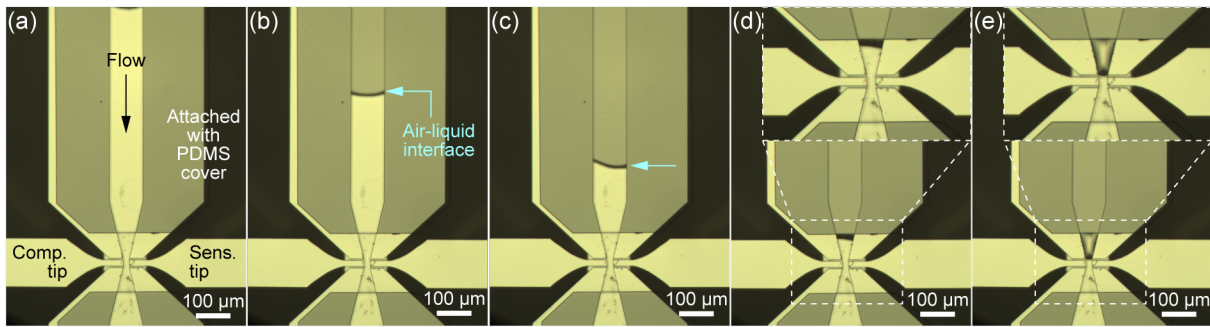
The sensing part had a more complex structure to provide mechanical oscillations for harmonic analysis while simultaneously performing electrical measurements [87],[74]. Phase-lock loops (PLL) were essential to maintain harmonic oscillations for mechanical measurements. A lock-in amplifier (Model 7230, AMETEK, Inc., Berwyn, PA, USA) drove the comb-drive actuators at a constant phase according to the differential capacitive sensor readings. Two stationary electrodes ( $C_1$  and  $C_2$ ), forming two identical capacitors with the movable electrode ( $C_0$ ), were connected to the inputs of the lock-in amplifier after passing through low-noise current-to-voltage (A/V) preamplifiers (Model 5182, Signal Recovery, AMETEK, Inc., Berwyn, PA, USA).  $C_0$ , on the other hand, was connected to a power source (provided by the lock-in amplifier) to be polarized with a constant voltage. The lock-in amplifier used sensor measurements to drive the actuators at the resonance frequency. The tip of the sensing area was connected to another lock-in amplifier (HF2LI, Zurich Instruments Ltd., Zurich, Switzerland) for electrical measurements. An electrical signal was applied on the sensing tip, while the compressing tip was connected to a transimpedance preamplifier (Zurich Instruments HF2TA) that fed the input of the lock-in amplifier.

The channel outlet on the microfluidic PDMS cover was connected to a flow sensor with tubing before reaching the vacuum pump (AF1, Elveflow, Paris, France) (**Fig. 3.12**). This equipment was monitored and controlled by the LabVIEW program.

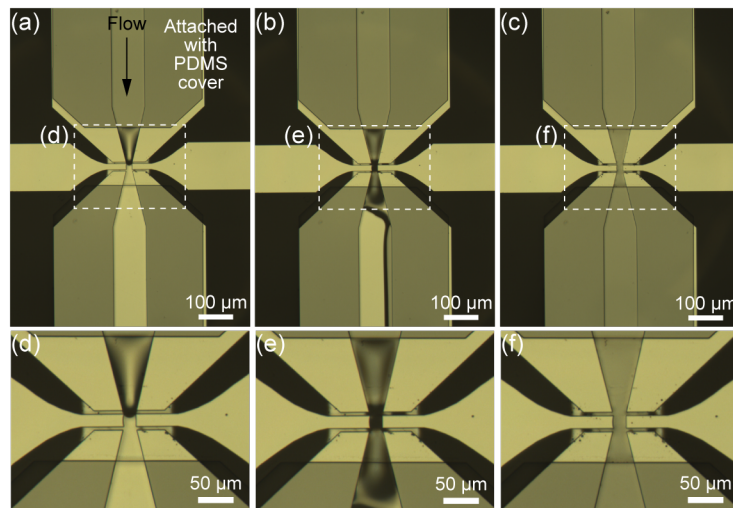
#### 3.4.1.1 Liquid Handling

As cell characterization can only be performed in a dedicated area, targeted cells inserted via the channel inlet have to be transported and positioned between the tips. Applying a negative pressure at the outlet of the channel creates a flow and adjusting the pressure level changes the flow speed to control the motion of cells in the channel.

After assembling the PDMS cover and the MEMS device, the outlet of the channel was connected to the pump with tubes (**Fig. 3.12**). Then, the channel filling protocol was started. At first, half of the channel was filled with liquid by capillary action (**Fig. 3.14 (a)-(d)**). Then, the pressure created by the pump was applied to the channel and the channel was filled up to the characterization area (**Fig. 3.14 (e)**). Then, the pressure in the channel was adjusted in order to break the air-liquid interface. The downstream of channel was filled with the liquid, as shown in **Fig. 3.15**, which was followed by filling the connection tube (no image).

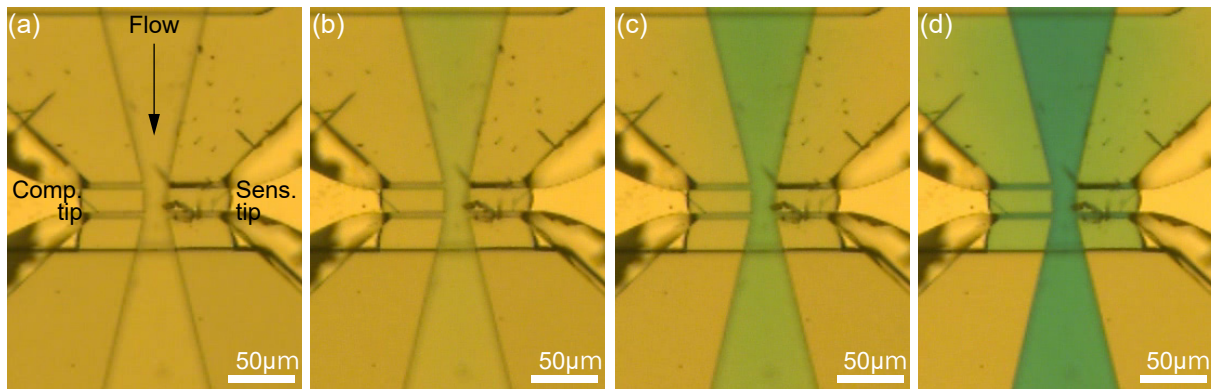


**Fig. 3.14** The channel filling protocol with liquid until tips part. **(a)** After assembling the PDMS cover on the MEMS device, the channel is formed. **(b) and (c)** The liquid is injected from the inlet and **(d)** adjusted the pressure with the pump, the liquid filled the channel. **(e)** The liquid reaches the opposing tips.



**Fig. 3.15** The channel filling protocol. **(a)** The liquid reaching the opposing tips and **(b)** going through the characterization part. **(c)** The channel completely filled with liquid. **(d)-(f)** Focus on tips.

Due to the small dimensions (5 μm gap between tips and the sidewalls), high surface tension at the characterization area maintained the stability of the air-liquid interface [104]. As a result, the liquid inside the channel did not leak out (**Fig. 3.15 (c) and (f)**). Moreover, by injecting another solution into the inlet, the liquid in the channel could be exchanged within seconds [79],[103]. This property is important for a variety of purposes, such as washing, surface treatment, and drug testing. **Fig. 3.16** demonstrates replacing water inside the channel with a blue-dye solution.



**Fig. 3.16** The liquid exchange capability of the silicon device with water and a blue dye solution. **(a)** While the channel is filled with water, **(b) and (c)** a blue dye solution is injected from the inlet and within seconds **(d)** the liquid in the channel is completely replaced.

### 3.4.1.2 Mechanical detection method

By avoiding the usage of the MEMS elements in liquid, a higher system quality factor could be achieved when performing sensitive harmonic analyses [102],[74]. In short, the sensing part of the device oscillated harmonically with a series of comb-drive actuators ( $0.2 \mu\text{m}$  of actuation at  $3 V_{\text{rms}}$ ). These actuators were driven at the resonance frequency of the system by a lock-in amplifier (Signal Recovery, AMETEK 7270 DSP). Due to the mechanical connection (between the sensor, the actuator and the sensing tip), actuators oscillated the central electrode ( $C_0$ ) of the differential capacitive sensor. Detecting the capacitance between the movable common electrode ( $C_0$ ) and the other two fixed electrodes of the differential capacitive sensor ( $C_1$  and  $C_2$ ), a LabVIEW-controlled PLL kept the sensing arm at resonance throughout the experiment. Capturing a biological sample between the tips changed the spring constant of the system, which could be detected as a change in the resonance frequency by the PLL driven by the lock-in amplifier.

To improve the detection performance of the displacement sensor,  $C_0$  was polarised with a constant voltage  $V_0$  ( $3 \text{ V}$ ) and the fixed electrodes were kept grounded [87],[74]. During harmonic oscillations, the change in the gap between the mobile and fixed parallel plate electrodes created dynamic currents that were collected from  $C_1$  and  $C_2$ . Amplified with low-noise current-to-voltage (A/V) preamplifiers (with a gain of  $10^8$ ), the sensor outputs were fed into the lock-in amplifier for real-time measurements.

### 3.4.1.3 Electrical detection method

Electrical insulation of the various elements of the sensing area was crucial for simultaneous mechanical and electrical detection. By connecting through the backside silicon, the SiO<sub>2</sub> layer kept the sensing elements mechanically attached while providing electrical access to each individual element. This allowed applying a sinusoidal signal at the actuator ( $3 V_{p-p}$  at the resonance frequency of the system) and to read the sensor outputs in parallel with the electrical measurements performed at the tip of the sensing arm.

The electrical detection was performed between the sensing and the compressing tips. A  $1 V_{p-p}$  signal was applied on the sensing tip, while the compressing tip was connected to the virtual ground of a transimpedance amplifier. The dynamic current passing through the amplifier was converted to voltage and measured in real-time. Moreover, by sweeping the frequency at the sensing tip, the frequency response of the system could be analyzed.

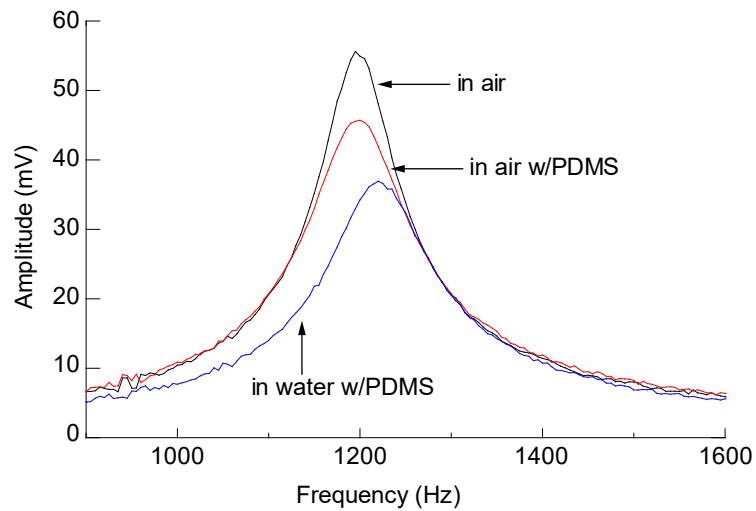
## 3.5 Device evaluation

Hereafter, some results are shown to investigate the performance of the proposed device. Starting with the frequency response of the device, mechanical and electrical measurements performed on different sample solutions are shown. Finally, the biomaterial-handling capabilities of the proposed device are demonstrated to confirm the capability of single cell analysis.

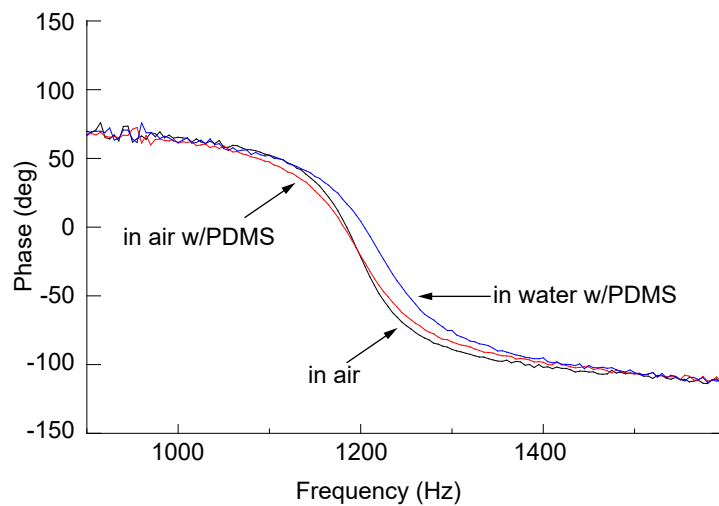
### 3.5.1 Frequency response and real time analysis

To characterize the behavior of the device during harmonic analysis, the frequency response of the system was monitored with the lock-in amplifier as a network analyzer. **Fig. 3.17** and **Fig. 3.18** depict the frequency response of the device in different conditions: the air, the air with the PDMS slab and the water with the PDMS slab. Compared to the initial device characteristics (resonance frequency of 1195 Hz with a quality factor (Q-factor) of 8.9), the assembled device (with a PDMS cover) showed a slight increase in the resonance frequency (1200 Hz) and a decrease in the Q-factor (6.9) due to the increased damping as a result of the PDMS slab. Filling the channel with liquid also changed the frequency response. Although the effect of the liquid in terms of mass was negligible compared to the total mass of the mobile part of the sensing arm, the surface tension at the air-liquid interface in the handling region affected the spring constant

of the system. As a result, the resonance frequency was increased to 1220 Hz with a similar Q-factor (6.8).



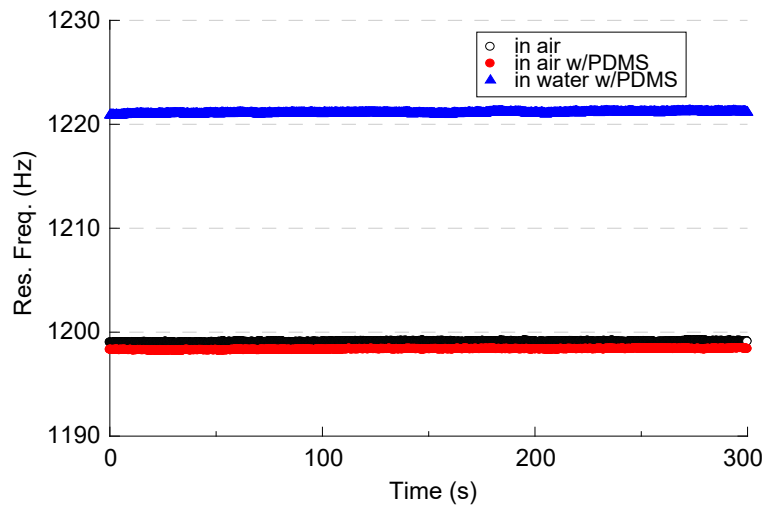
**Fig. 3.17** Frequency response of the device in different conditions showing the amplitude shift of the sensor readouts.



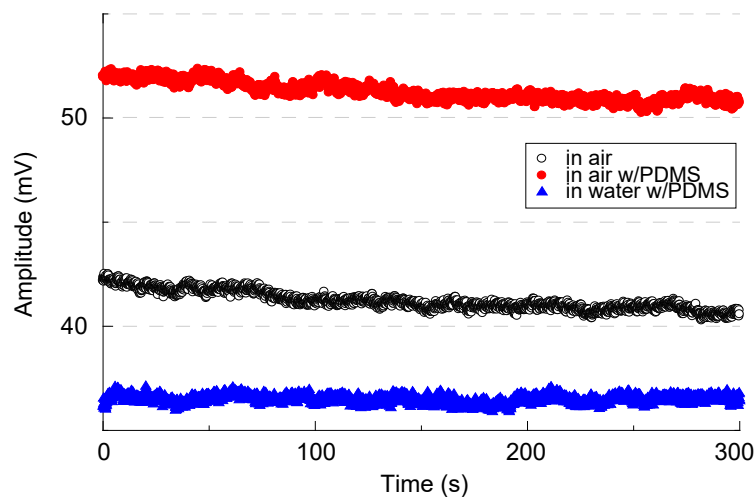
**Fig. 3.18** Frequency response of the device in different conditions showing the phase shift of the sensor readouts.

Observing the changes in the mechanical properties of biological samples requires real-time monitoring of the system response. To achieve this, repeated PLLs were performed while controlled by a LabVIEW program. Before comparing different samples and solutions, stability of the detection method was tested. The stability of the system was monitored for over 5 min

although the mechanical characterization of cells requires less than 30 seconds, as shown in **Fig. 3.19** and **Fig. 3.20**. Confirmation of the system stability allowed performing mechanical measurements in various sample media.



**Fig. 3.19** Real-time measurement of the device to examine the detection stability. Resonance frequency of the sensor readouts in 5 min.



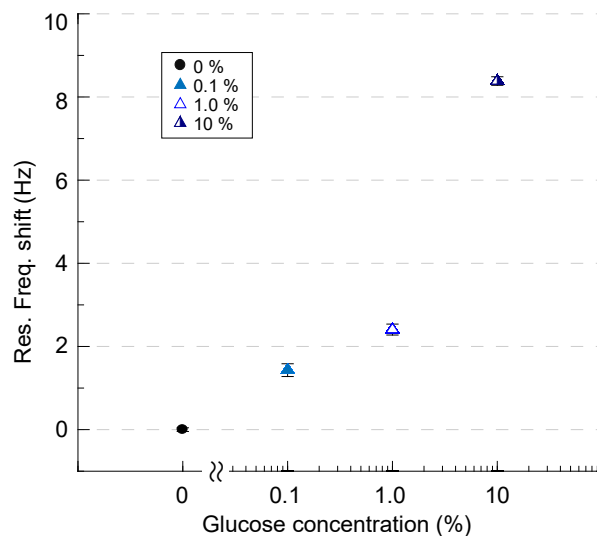
**Fig. 3.20** Real-time measurement of the device to examine the detection stability. Amplitude shift of the sensor readouts in 5 min.

### 3.5.2 Mechanical measurements

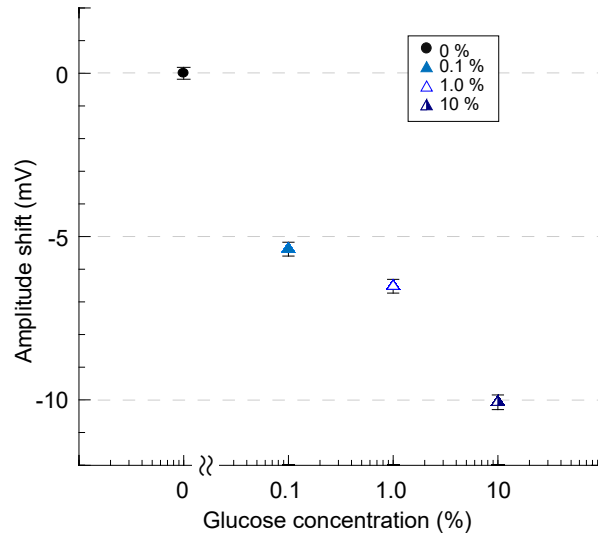
Mechanical detection performance of the system was tested by measuring the change in the resonance frequency in solutions with different viscosities and surface properties. The mechanical

response of the device was compared in glucose solutions of various concentrations ranging from 0.1 % to 10 % (w/v). Using the vacuum pump, these solutions were consecutively injected after filling the channel with water. The PLL measurements allowed real-time observation of the changes in the solution between the tips.

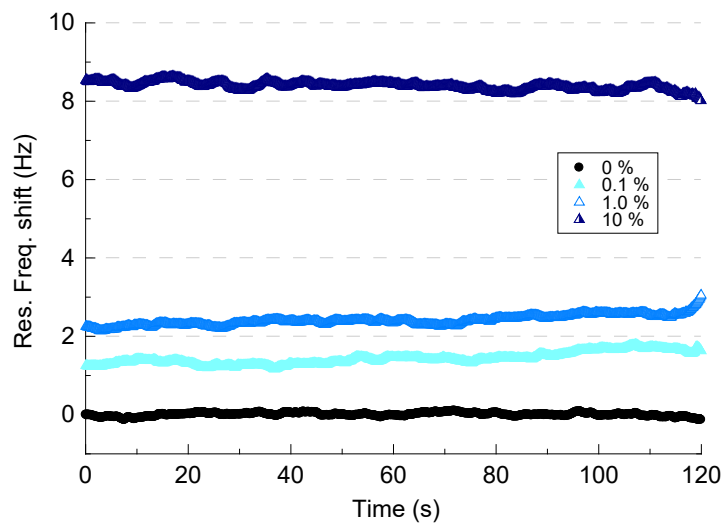
Increasing glucose concentration resulted in an increase of the resonance frequency (**Fig. 3.21** and **Fig. 3.22**). Taking the water measurements as the base value, resonance frequency shifts of 1.4 Hz, 2.4 Hz, and 8.3 Hz were obtained for glucose concentrations of 0.1 %, 1 % and 10 %, respectively (**Fig. 3.21**) with stable characteristics (**Fig. 3.23**). Similarly, a decrease in amplitude was observed with increasing glucose concentration (**Fig. 3.22**, **Fig. 3.24**). Compared to the initial water measurements, a decrease of 5 mV, 7 mV, and 10 mV in the amplitude was observed due to higher damping. These measurements show that the proposed device was capable of observing changes in the mechanical characteristics at the characterization area.



**Fig. 3.21** Resonance frequency of the system increased with increasing glucose concentration.

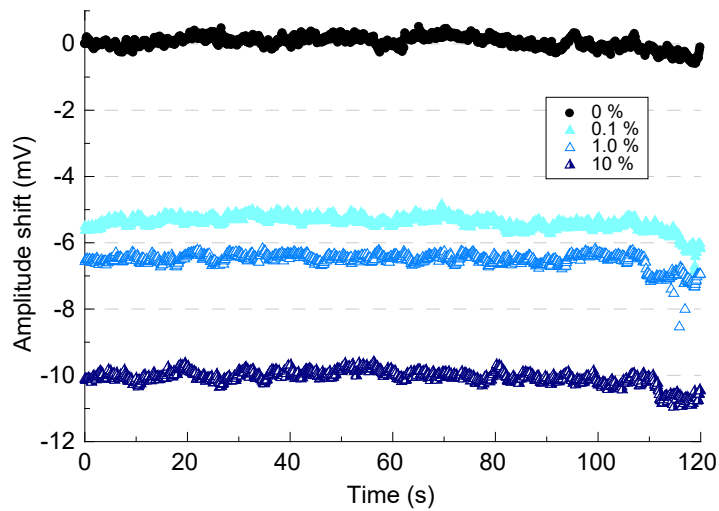


**Fig. 3.22** The amplitude of the system decreased with increasing glucose concentration.



**Fig. 3.23** Mechanical characteristics of glucose solutions with different concentrations in real-time. Resonance frequency increased with increasing glucose concentration.





**Fig. 3.24** Mechanical characteristics of glucose solutions with different concentrations in real-time. The amplitude decreased with increasing glucose concentration.

### 3.5.3 Electrical measurement

An important feature of the proposed device was the ability to perform electrical measurements together with mechanical characterization. To demonstrate this capability, solutions with different ionic strengths were injected in the channel and examined according to their electrical properties. Similar to the glucose measurements, the channel was first filled with water and then different molar concentrations of NaCl (0.1 mM ~10 mM) were consecutively injected. Using a lock-in amplifier, 1 V<sub>p-p</sub> was applied on the sensing tip and the signal obtained from the compressing tip was amplified with a transimpedance amplifier (with a gain of 10<sup>5</sup>). Measurements resulted in increasing voltage waveform amplitudes for increasing ion concentration when the potential difference was applied at 4 kHz (**Fig. 3.25**) indicating an increase in the current passing through the tips. In addition to these real-time measurements (**Fig. 3.27** and **Fig. 3.28**), we could also obtain the frequency response of the system by sweeping the frequency from 100 Hz to 100 kHz (**Fig. 3.26** and **Fig. 3.29**).

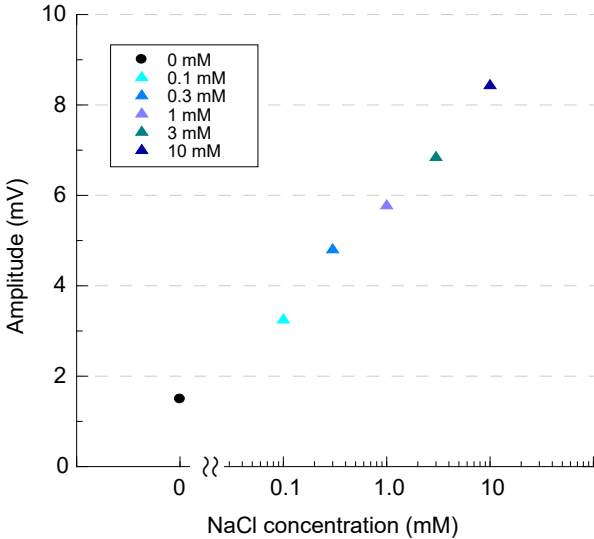


Fig. 3.25 The amplitude of the signal at 4 kHz in different conditions.

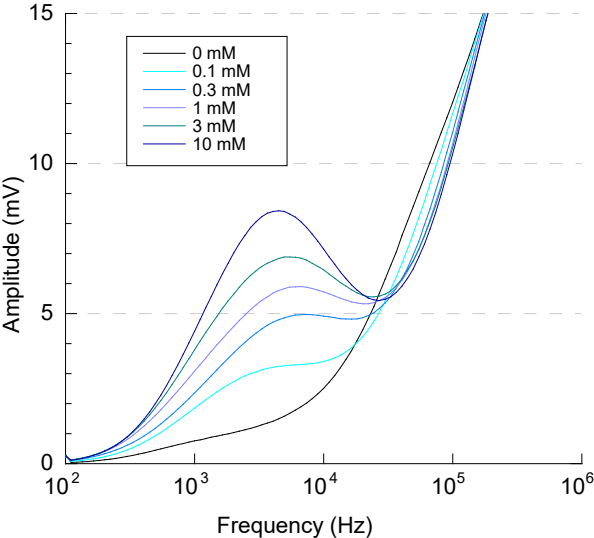
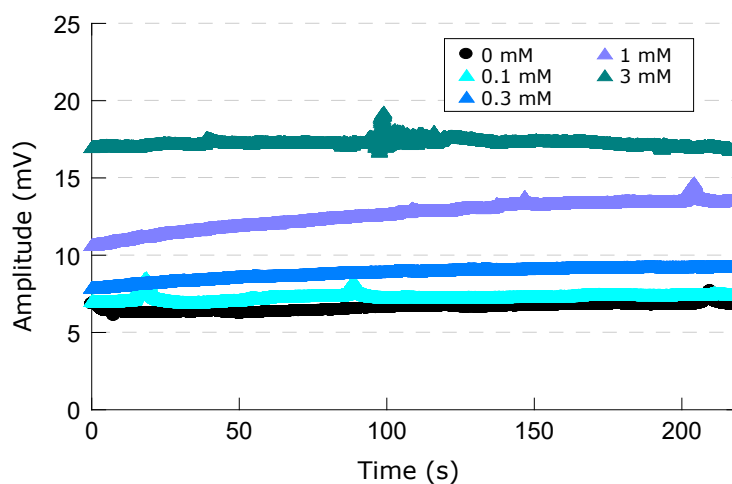
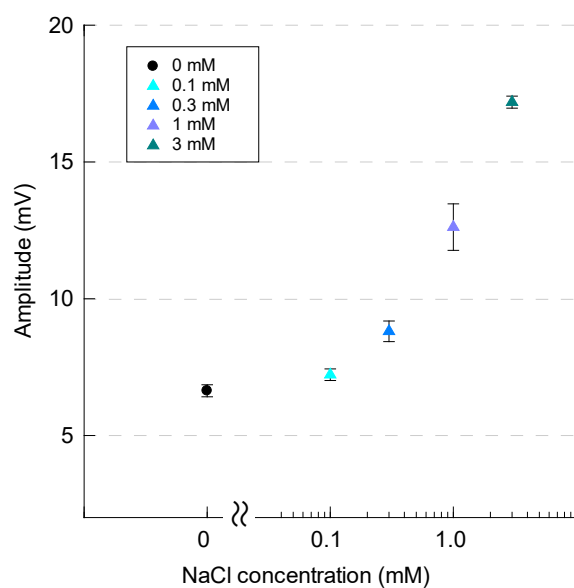


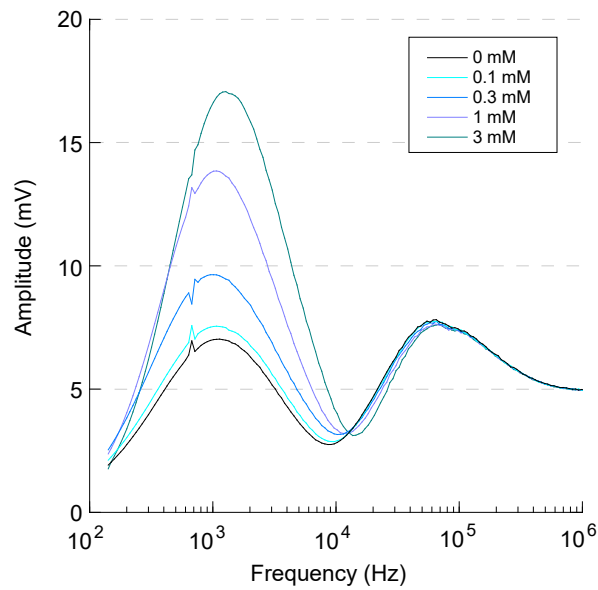
Fig. 3.26 The amplitude of the signal during sweeping the frequency in different conditions.



**Fig. 3.27** The real-time measurements were performed at 1 kHz. Higher NaCl concentration resulted in a higher current which is detected as higher amplitude.



**Fig. 3.28** Average value of the real-time measurements show the relation between the NaCl concentration and the amplitude.



**Fig. 3.29** Sweeping the frequency provided the frequency response of the system. Note that the electrical measurements detected a small noise due to the mechanical measurements at around 600 Hz. The target frequency for the electrical measurements and the mechanical resonance frequency of the MEMS device should be designed carefully.

## 3.6 Conclusions

Separating handling and sensing elements of a microfabricated device is the key to handle and analyze biological samples without compromising optimal MEMS performance. **Chapter 3** demonstrated a MEMS device with a built-in microfluidic channel to perform single cell biophysical characterization. The built-in channel, requiring no assembly actions between the MEMS and microfluidics elements, not only provides higher-throughput for analysis but also improves sensitivity by allowing integration of microfluidic and MEMS elements at a much finer assembly resolution. Moreover, simultaneous electrical and mechanical measurements allow various parameters to be targeted, such as size, stiffness, viscous losses, membrane fluidity, membrane capacitance, and cytoplasm resistivity. The device is sensitive enough to distinguish differences between liquids according to their mechanical and electrical properties. Applying this device on biological samples is demonstrated in **Chapter 4**.

# Chapter 4

## Cell biophysical characterization with a built-in channel device

### 4.1 Introduction

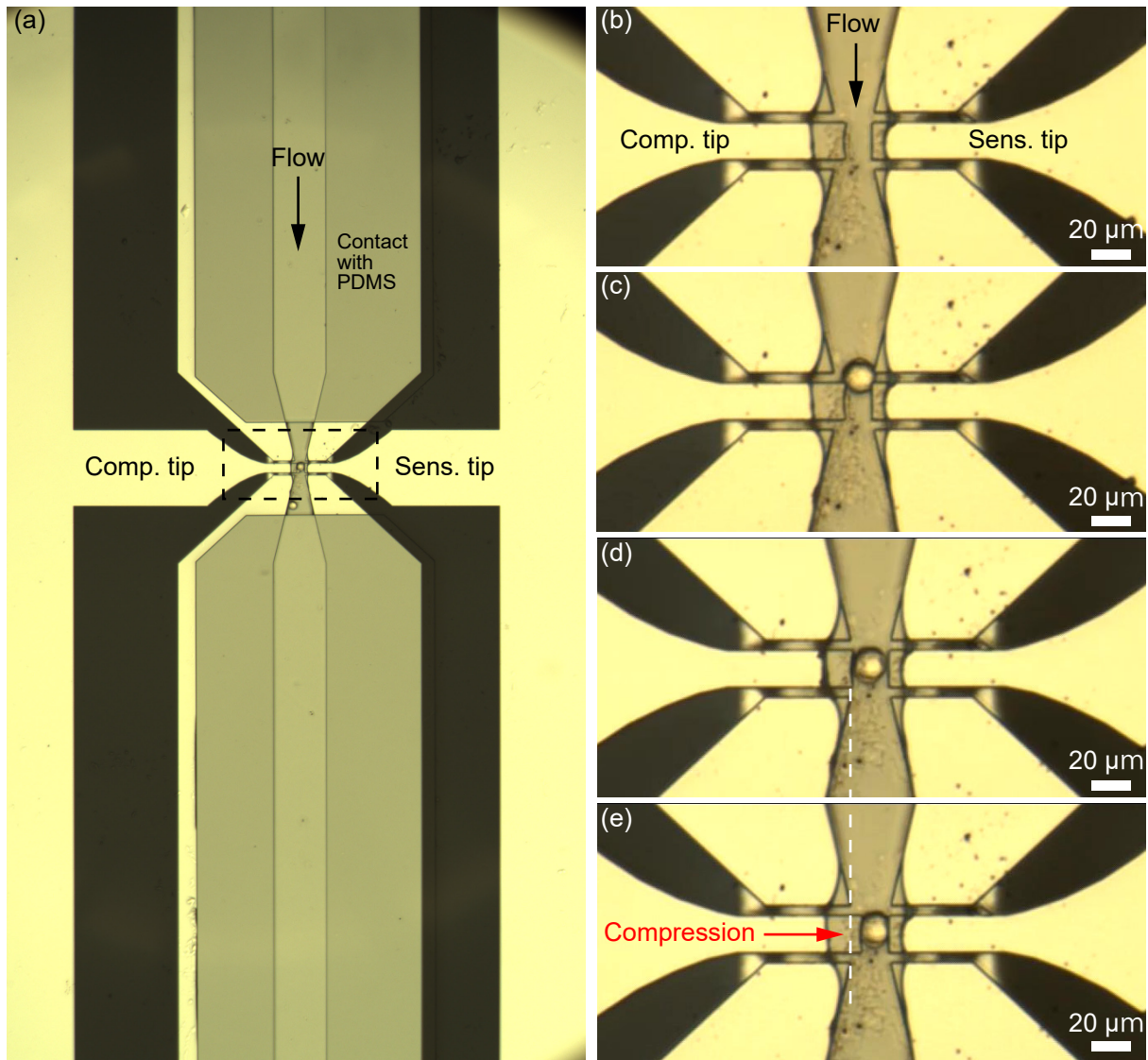
The key features of the developed channel integrated MEMS device were described in **Chapter 3**: the liquid inside channel could be replaced within seconds, mechanical detection was sensitive enough to distinguish solutions with different viscosity and solutions with different ionic strength could be discriminated. In **Chapter 4**, the developed device was used for biophysical analysis of cancer cells. In **Section 4.2**, a single cell capturing protocol is explained. Initial tests used **fixed cancer cells**, although distinguishing live cancer cells have already been demonstrated using SNTs [84]. Single cells in suspension were flown inside the channel using the pressure controlled pump and stopped at the characterization area. Two different cell lines were characterized, as described in **Section 4.3**. Similar to the protocol described in **Section 2.3**, continuously compression cycles were applied on the cell and resonance frequency and amplitude measurements were obtained. The stiffness and the viscous losses were calculated from experiment results. To demonstrate electrical characterization, electrical measurements were obtained using SUM159PT cells. In **Section 4.4**, the measured SUM159PT data was compared with another cell line, MCF7. Also, the SNT measurements and the new channel integrated MEMS device measurements were compared.

## 4.2 Single cell capturing procedure

Actual cell characterization, such as mechanical property measurements, was performed with a single cancer cells. Here, the experimental setup used for this experiment was not repeated as the applied method was the same as the one detailed in the previous chapter in **Subsection 3.4.1**. Fixed human breast cancer cell lines, SUM159PT cells and MCF7 cells, were used in this experiment. The cell fixation protocol is explained in **Subsection 4.3.2 and 4.3.3**. Due to fixation, cells can maintain a stable state for a long time. After injecting the fixed cell suspension via the inlet hole the following capturing protocol was performed:

1. First, the microfluidic channel was filled with a biological buffer such as phosphate-buffered saline solution (PBS, 8.475 g NaCl, 1.093 g Na<sub>2</sub>HPO<sub>4</sub>, and 0.276 g NaH<sub>2</sub>PO<sub>4</sub> in 1 L DI water; pH 7.4) for fixed cells or culture medium for live cells (**Fig. 4.1 (a)**). The liquid had to reach the PDMS cover. Especially at the characterization area, the space between the frontside Si surface and the PDMS cover had to be filled with liquid to obtain a stable air-liquid interface.
2. To decrease the distance between the tips, the compression tip was driven closer to the opposing tip (sensing tip) by applying a potential difference between the electrodes of the electrostatic actuator in the compression side. This facilitated the cell trapping (**Fig. 4.1 (b)**).
3. A cell solution was injected from the inlet hole and flown by controlling the vacuum pump. A cell, moving with the flow, was stopped at the characterization area (**Fig. 4.1 (c)**). Then, the flow rate was reduced.
4. The potential difference at the compression side was reduced to open the tip and after the cell moving between the tips with the slow flow, the tips were quickly closed again. As a result, the cell was captured between the two tips (**Fig. 4.1 (d)**).
5. Finally, the flow was stopped completely and measurements from the sensing tip were recorded to detect the cell response while the cell compression cycles were applied on the captured cell (**Fig. 4.1 (e)**).

This is the procedure used for capturing single cells characterizing their mechanical properties.



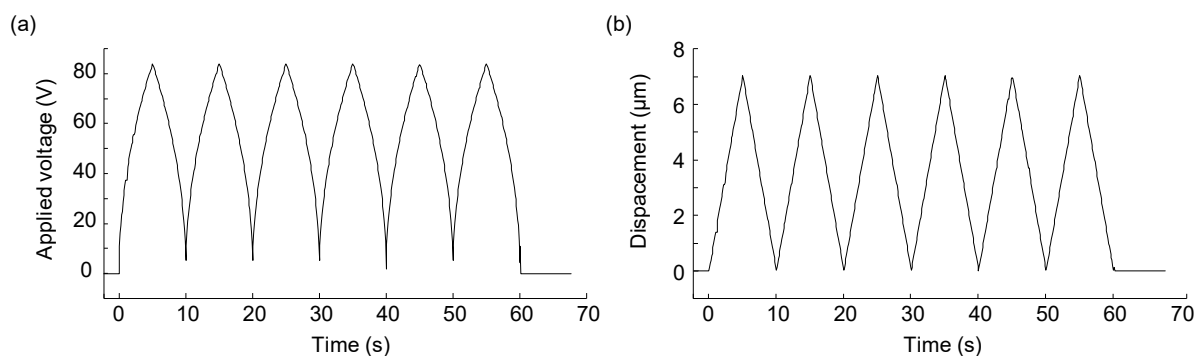
**Fig. 4.1** Low magnification image of the channel and the characterization area (a), and sequential photos demonstrate single cell capturing (b)-(e). (a) The channel and the characterization area. Only the channel part except around tips is closed with the PDMS cover. (b) Applying a potential difference between the compressing actuator electrodes narrows the gap between the tips. (c) The solution is kept flowing until a cell arrives at the handling area. (d) Then, the flow rate and the potential difference between the compressing actuator electrodes are decreased until the cell is positioned between the tips. (e) Finally, the flow is completely stopped and cell compression is performed.

## 4.3 Results

### 4.3.1 SUM159PT (fixed)

The human SUM159PT breast cancer cell line was purchased from Asterand (Detroit, MI, USA). The cells were cultured in F12 medium (Invitrogen Corporation, Carlsbad, CA, USA) supplemented with 5 % fetal bovine serum (Lonza Group, Basel, Switzerland), streptomycin (100  $\mu\text{g}/\text{mL}$ ), penicillin (100 units/mL), insulin (5  $\mu\text{g}/\text{mL}$ ) and hydrocortisone (1  $\mu\text{g}/\text{mL}$ ) (Invitrogen). Prior to the experiment, the fixation of cells were performed. Subconfluent cultured cells were trypsinized and resuspended in single cell solution. Then, cells were fixed with 4 % Paraformaldehyde in 10 min at the room temperature and were rinsed with PBS. After cell fixation, cells were kept in PBS.

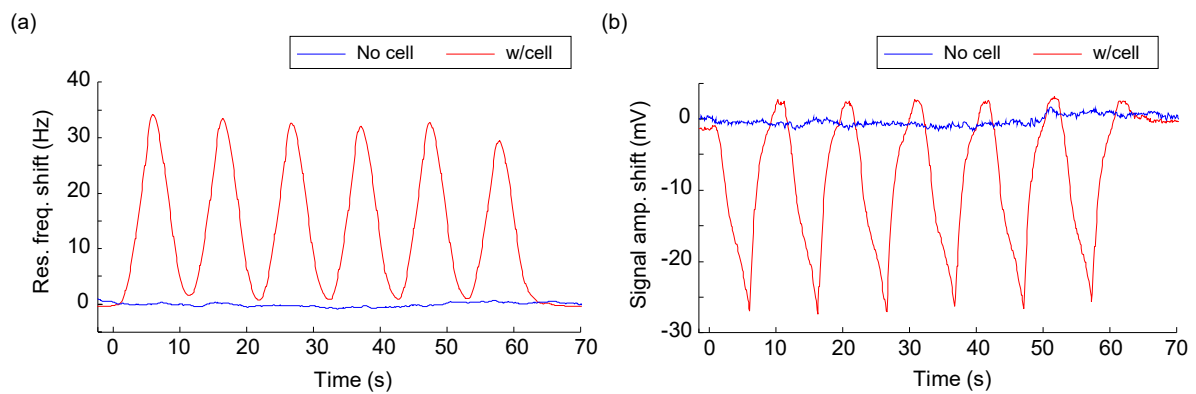
A fixed cell suspension was injected to the channel from the inlet hole and the cell-capturing protocol was applied (see **Section 4.2**). Then, the compression tip performed cell compression cycles ( **Fig. 4.2 (a)**). Six consecutive compression-relaxation cycles (10 s of compression followed by 10 s of relaxation) were applied on each captured cell. For linear compression, a square root signal was used (**Fig. 4.2 (b)**). Applying a potential difference of 85 V between the comb-drive electrodes in the compression side provided a decrease of about 7  $\mu\text{m}$  in the gap between the tips (since the initial gap length was 20  $\mu\text{m}$ , the gap closed down to 13  $\mu\text{m}$ ).



**Fig. 4.2** The cell compression cycles. **(a)** Voltage cycles applies to electrostatic combs in the compression side for compressing the captured cell, and **(b)** Displacement of the compression tip. The tip moves over 7  $\mu\text{m}$  with applied voltage of 85 V.

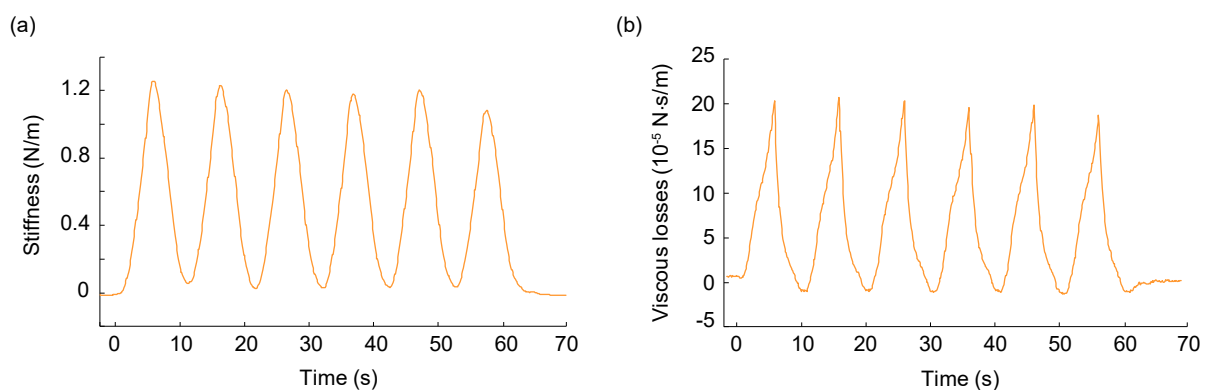


**Fig. 4.3 (a)** and **Fig. 4.3 (b)** show an example of real-time responses (changes) of resonance frequency shift and amplitude shift during cell compression (in red line). In the same graph, the response before capturing the cell was shown as a control case (in blue line). The differences between resonance frequency and amplitude signals, and the control experiments correspond to the effect of the compressed cell. The resonance frequency was increased while the vibration amplitude was decreased with the increasing compression level.



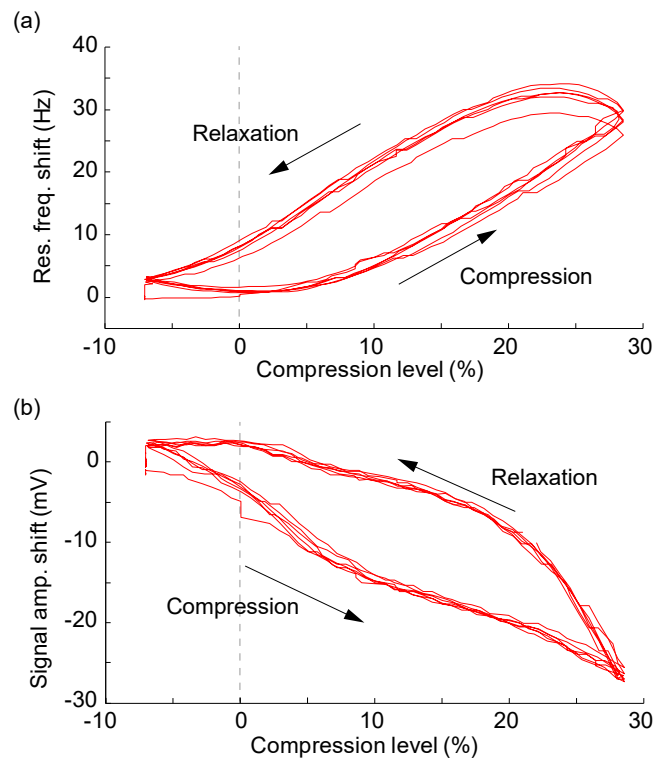
**Fig. 4.3** Frequency response in real-time. **(a)** Applied compression cycles resulted in resonance frequency changes (in red). No cell control (in blue) was also shown in same graph, and **(b)** Applied compression cycles resulted in amplitude shift (in red).

Using **Equation (2.11)** and **Equation (2.12)**, the stiffness (in N/m) and the viscous losses (in  $\text{N} \cdot \text{s}/\text{m}$ ) of the captured cell were calculated from these real-time responses (**Fig. 4.4**). Both the stiffness and the viscous losses were increased during cell compression.



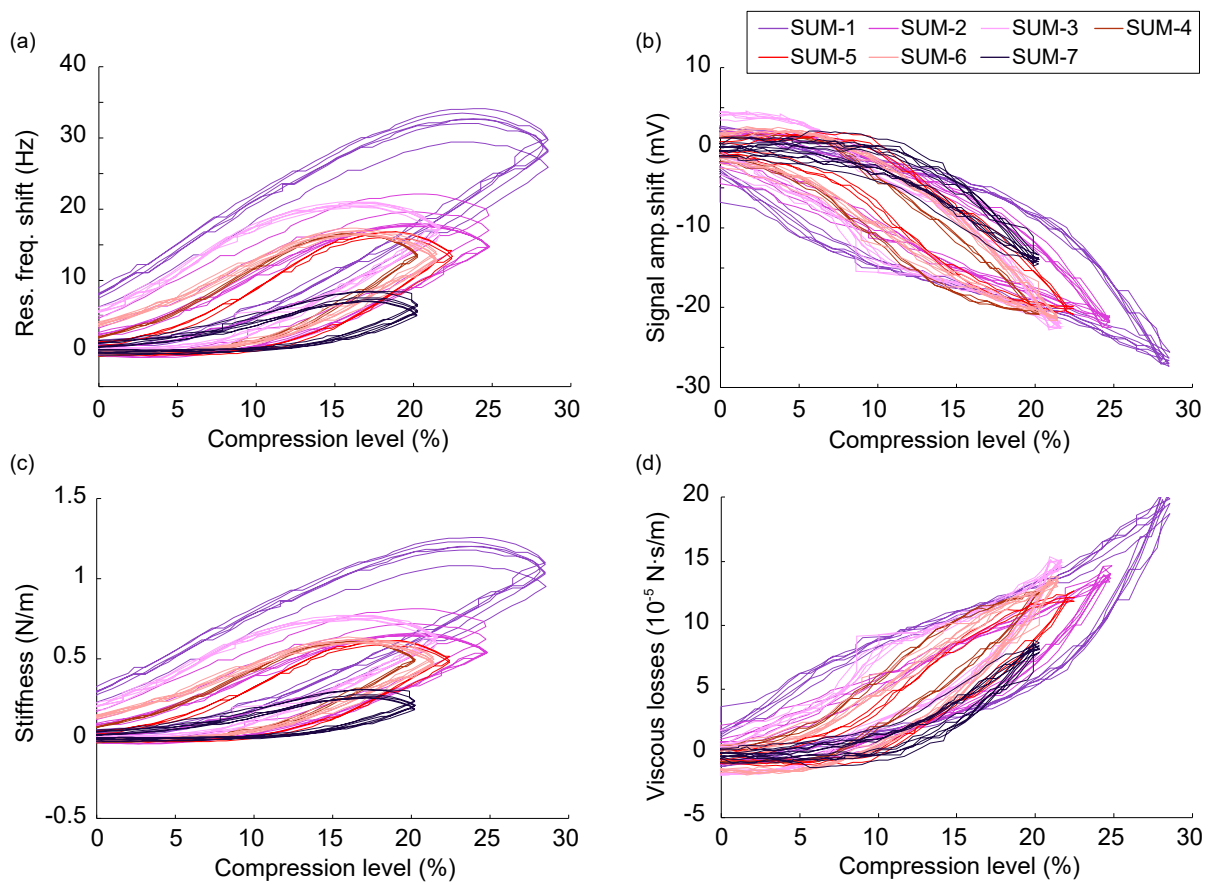
**Fig. 4.4** Real-time responses of the cell. **(a)** Stiffness, and **(b)** Viscous losses of the captured cell.

Size of cells in a solution varies even within the same cell line, as shown in **Fig. 2.2**. Therefore, the compression level of the cell was obtained by normalization based on the original diameter for better comparison. For example, a captured cell was compressed 7  $\mu\text{m}$  by applying a potential difference of 85 V on the compression comb actuator reaching to about 30 % of compression (**Fig. 4.5**).



**Fig. 4.5** Presented compression cycles using the cell compression level. **(a)** Resonance frequency shift, and **(b)** Signal amplitude shift.

Seven different SUM159PT cells (which were named as SUM-1 to SUM-7) were characterized. As described above, these cells were compared in the resonance frequency shift, the amplitude shift, the stiffness and the viscous losses using the cell compression level in % (**Fig. 4.6**). Each graph has similar tendency. When the compression level increased, the resonance frequency shift, the stiffness and the viscous losses were increased. In contrast, the signal amplitude shift was decreased. Conditions of cell compression cycles applied to seven different fixed SUM159PT cells are summarized in the **Table. 4.1**. Two different voltages at 75 V and 85 V were applied to the electrostatic combs actuator in the compression side. Also, there were different compression cycles as 3 periods or 6 periods in one compression cycle.



**Fig. 4.6** Mechanical properties of seven different SUM159PT cells during the compression. (a) Resonance frequency, (b) Signal amplitude shift, (c) Stiffness, and (d) Viscous losses.

**Table 4.1** Cell compression conditions applied to seven different SUM159PT cells

Cell number	Applied voltage	Periods	Time/ 1 period
SUM-1	85 V	6	10 s
SUM-2	85 V	6	10 s
SUM-3	85 V	6	10 s
SUM-4	75 V	3	10 s
SUM-5	75 V	3	10 s
SUM-6	85 V	6	10 s
SUM-7	75 V	6	10 s

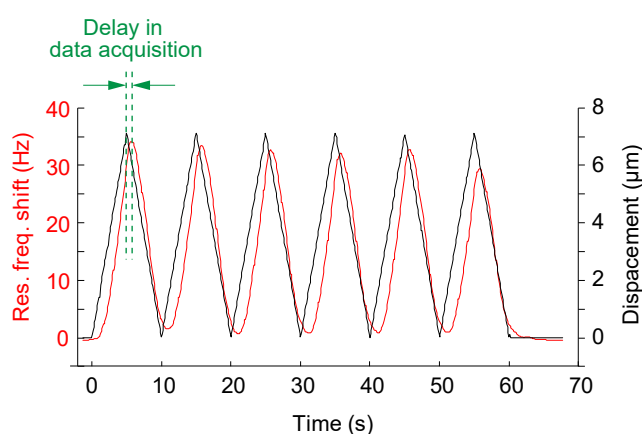
The cell size was detected by the gap between the tips at the starting point of cell detection by capacitive sensor (**Fig. 4.2 (b)** and **Fig. 4.3 (a)**). Hence, by subtracting the compressing arm displacement (at the applied potential difference) from the initial gap distance of 20  $\mu\text{m}$ , the cell dimension can be calculated. The analyzed cell sizes are summarized in **Table. 4.2**. For given experiments, the cell size was detected based on the resonance frequency measurements. However, as seen clearly on **Fig. 4.5**, the starting point of the change differs between the resonance frequency and the amplitude measurements. The optical images suggested the resonance frequency measurements to be more accurate for size detection. Yet, further analysis with higher resolution and slower compression would be beneficial to provide a better selection of the size detection protocol.

**Table 4.2** Measured cell size of SUM159PT

Cell number	Cell size
SUM-1	18.6 $\mu\text{m}$
SUM-2	17.8 $\mu\text{m}$
SUM-3	17.2 $\mu\text{m}$
SUM-4	18.6 $\mu\text{m}$
SUM-5	19.0 $\mu\text{m}$
SUM-6	17.2 $\mu\text{m}$
SUM-7	18.6 $\mu\text{m}$

According to applied voltage, the maximum displacement of the compression tip presented in the examples was different. For cells SUM-1, SUM-2, SUM-3 and SUM-6, 85 V of a potential difference was applied on the actuator of the compression side to compress the cells up to 7  $\mu\text{m}$ . However, as shown in **Fig. 4.6** and **Table. 4.2**, the maximum cell compression level was different due to the cell size. For example, SUM-1 cell reached to about 30 % of compression as its size was 18.6  $\mu\text{m}$ . Other cells such as SUM-2, SUM-3 and SUM-6 could only reach around 22-25 % of compression even though the applied voltage was the same. SUM-4 and SUM-7, both having similar size as SUM-1, were compressed at the maximum applied voltage of 75 V resulted in a compression level reaching only to 20 % compression.

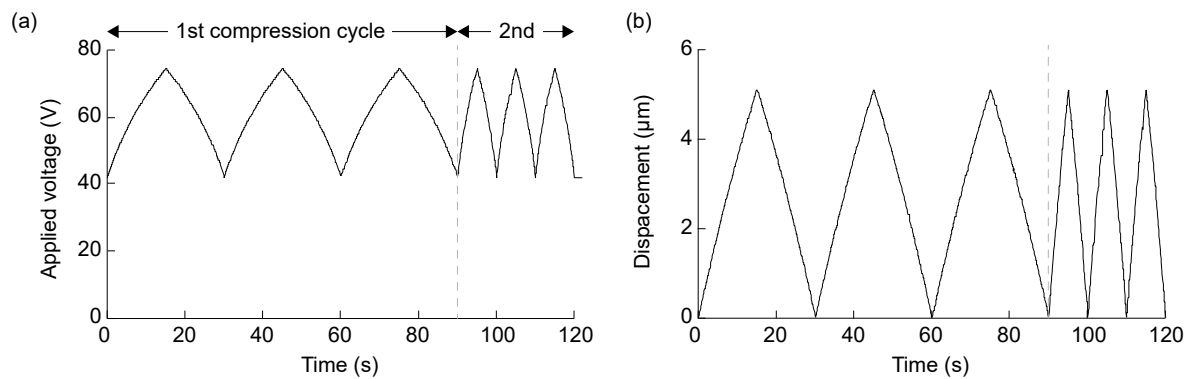
The compression-relaxation (retract) part exhibited hysteresis as shown by the arrows in the **Fig. 4.5**. This demonstrates the limitation of the resolution of the system detection with the current condition. The resonance characteristics (the frequency and the amplitude) of the system were examined using PLL algorithm with every 20 ms-time resolution. Also, the phase of PLL was read with 100 ms-time resolution and provides the feedback to keep the lock value of PLL. There was a delay of data acquisition time and the system cannot follow the cell response, as shown in **Fig. 4.7**. From this, these hysteresis loops were caused by the measurement system but did not represent a response of the cell itself.



**Fig. 4.7** Delay in the data acquisition. Resonance frequency shift (in red) and displacement of compression tip (in black) were shown.

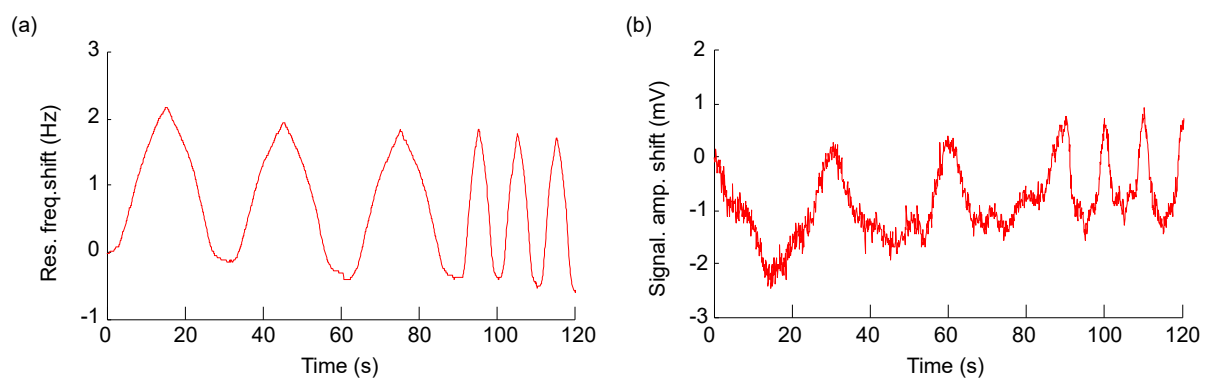
### 4.3.2 Correction of data acquisition time lagging

As shown in **Fig. 4.6**, there were hysteresis loops due to a lag in data acquisition. As the most-likely reason of this lag was the response of the cell being much faster than the measurement speed, the data acquisition of the measurements was changed from 20 ms to 1 ms-time resolution. To cope with the faster response, the feedback was also changed from 100 ms to 20 ms loops. With the new system setting, compression cycles were applied on another SUM159PT cell between the tips (**Fig. 4.8**). The cell started to be sensed after applying a potential difference of about 40 V. Then, compression cycles (compression-relaxation periods) were repeated six times. The first three cycle were applied with a period of 30 seconds and the following three cycles were applied with 10 seconds periods.

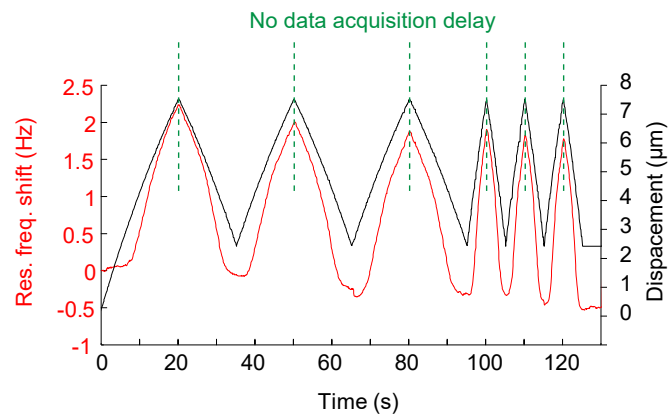


**Fig. 4.8** (a) Square root voltage cycles applies to comb drive actuator on compression side, and (b) Displacement of the compression tip.

The result of faster response time for the given compression cycles fit better with applied potential difference (**Fig. 4.9**). Both shifts were set to zero at the starting point of the cell compression cycle. The resonance frequency increased while the amplitude decreased during the cell compression. There was no delay of data acquisition time with the new system setting. (**Fig. 4.10**) For better comparison of the compression, each compression cycle is analysed as the change in the resonance frequency and signal amplitude with respect to the compression level. This provides better information on the cell behaviour under repeated compression cycles.

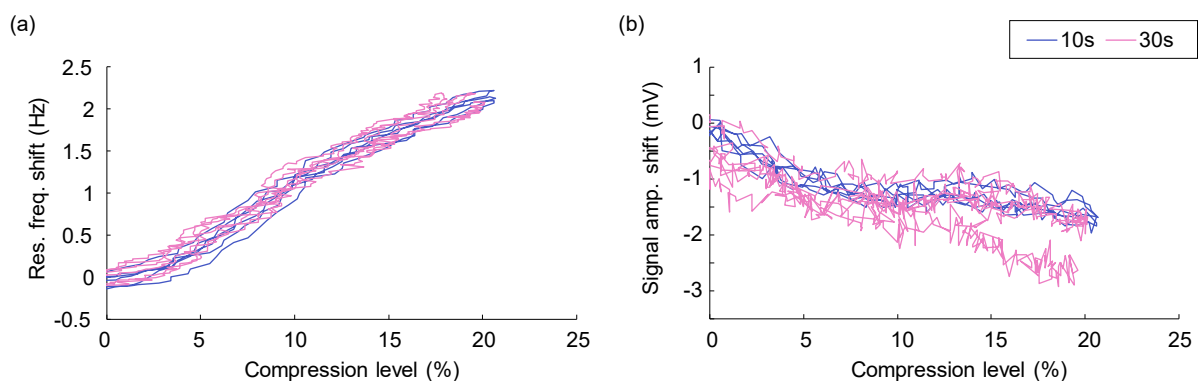


**Fig. 4.9** Cell responses of the captured cell in real-time while applying cell compression cycles. (a) Resonance frequency shift, and (b) Signal amplitude shift.



**Fig. 4.10** After correction of data acquisition time. Resonance frequency shift (in red) and displacement of compression tip (in black) were shown.

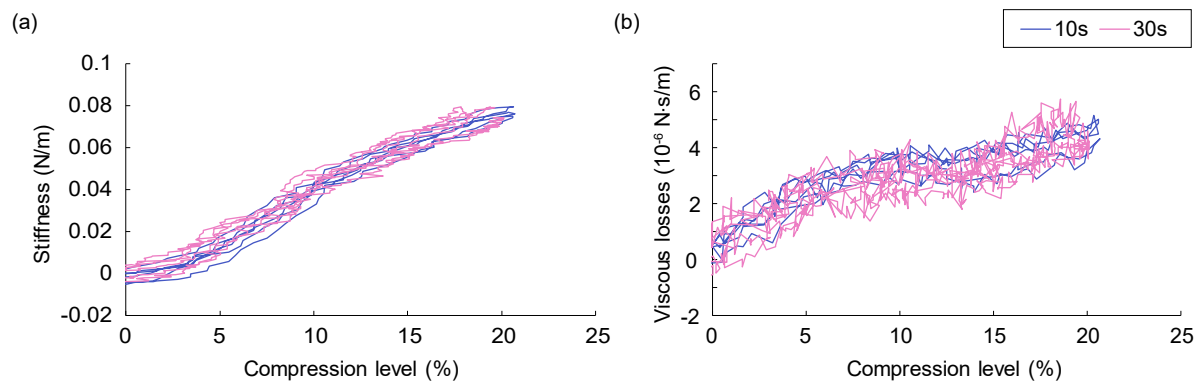
The captured cell was compressed until 20 % of the cell initial size even though the compression duration was different (**Fig. 4.11**). The resonance frequency shift and the signal amplitude shift showed the similar change of around 2.2 Hz and -2.0 mV, respectively, regardless of the cell compression duration. Also, no hysteresis was observed in these graphs. It was confirmed that the hysteresis was not due to the cell itself but due to the delay of data acquisition time.



**Fig. 4.11** Compared two different duration time (10s: in purple, 30s: in pink) by the compression level. **(a)** Resonance frequency shift, and **(b)** Signal amplitude shift.

Similar to the previous experiments, the stiffness and the viscous losses of the captured cell were calculated using **Equation (2.11)** and **Equation (2.12)**. The stiffness and the viscous losses changed with increasing compression levels regardless of the compression duration such as 30 seconds or 10 seconds (**Fig. 4.12**). The viscous losses showed a more complex result when compared to the stiffness result which had a more linear characteristics. This suggests that these different parameters can be helpful to distinguish cells based on different properties. Moreover,

obtaining similar responses during repeated compression cycles suggested that the cell was not damaged during the compression.



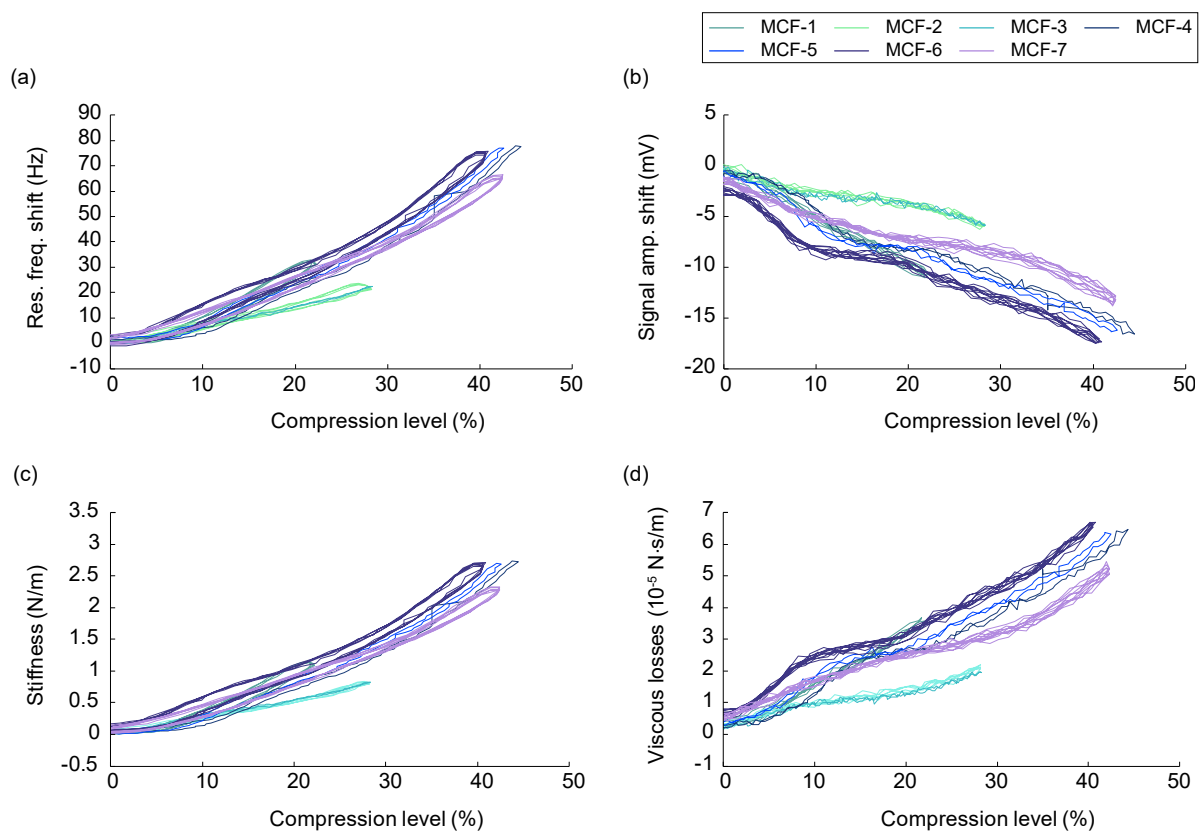
**Fig. 4.12** Mechanical properties of the captured cell compared two different duration time (10 seconds: in purple, 30 seconds: in pink). **(a)** Stiffness, and **(b)** Viscous losses.

### 4.3.3 MCF7 (fixed)

The same protocol was applied to carry out measurements on a different cancer cell line, i.e. MCF7. MCF7, human breast cancer cell line, was obtained from ATCC. The cells were cultured in DMEM medium (Invitrogen Corporation, France) supplemented with 10 % fetal bovine serum (Lonza, France), streptomycin (100  $\mu\text{g}/\text{mL}$ ), penicillin (100 units/mL). Before measurements in the developed channel integrated MEMS device, cells were trypsinized (0.1 % Trypsin/EDTA) to detach them from the culture flask and washed with PBS. Fixation of cells were done with 4 % Paraformaldehyde in 10 min at the room temperature. After that, they were kept in PBS. Cells assumed to have a spherical shape in suspension without any further manipulation.

The floating single cell suspension introduced in the channel to be characterized between two tips. The data acquisition time of measurement response of the system was the same as **Subsection 4.3.2**, i.e. 1 ms of data acquisition for 20 ms loops. As shown in **Fig. 4.13**, seven different MCF7 cells were characterized. Similar to the corrected SUM159PT examples, MCF7 results did not show any significant hysteresis.





**Fig. 4.13** Mechanical properties of seven different MCF7 cells during the compression in real-time. (a) Resonance frequency shift, (b) Amplitude shift, (c) Stiffness, and (d) Viscous losses.

The characterized cells were allocated to names from MCF-1 to MCF-7. To apply the linear compression to the captured cell, the square root signal was provided to the comb drive actuator on the compression side (see an example in **Fig. 4.2**). Conditions of the cell compression which applies to seven different cells were summarized in **Table. 4.3**. The MCF-1 to MCF-3 were provided the applied voltage at 85 V on the compression side and MCF-4 to MCF-7 were provided at 115 V. There were three different cell compression cycles from 1, 3, until 5 periods (one period included the compression-relaxation). Also, three different compression periods were tested: 10 s, 15 s, and 30 s.

**Table 4.3** Conditions of the cell compression for providing seven different MCF7 cells

Cell number	Applied voltage	Periods	Time/1 period
MCF-1	85 V	3	10 s
MCF-2	85 V	3	10 s
MCF-3	85 V	1	30 s
MCF-4	115 V	1	30 s
MCF-5	115 V	1	30 s
MCF-6	115 V	5	15 s
MCF-7	115 V	5	15 s

The resonance frequency shift, the signal amplitude shift, the stiffness, and the viscous losses of the cell showed expected results during compression (**Fig. 4.13**). Once more, no significant differences were detected based on the number of compression cycles. Applied higher voltage resulted in the higher compression level of the captured cell. Cells MCF-4 to MCF-7 were exposed to a compression obtained by applying 115 V on the compression side of comb drive actuator. Obtained compression was about 40 % of the initial cell size. In the case of applying 85 V, on cells MCF-1 to MCF-3, the cell compression level were reached around 20-30 %. These variations were due to the different size of captured cells. MCF-2 and MCF-3 have almost the same cell size with very similar mechanical properties.

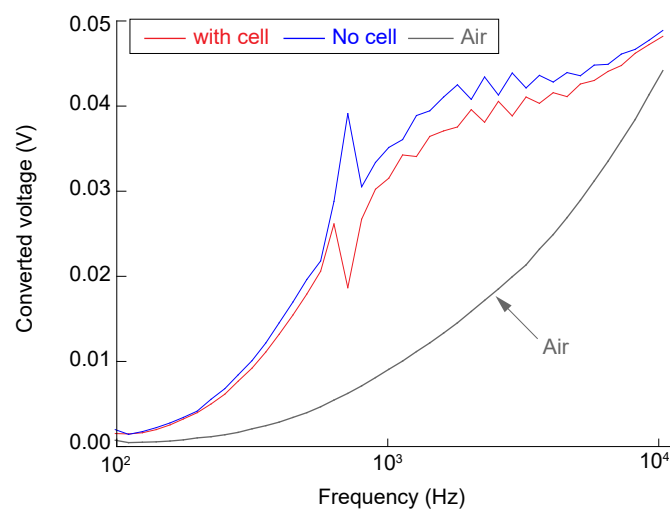
The size of MCF7 cells, summarized in **Table 4.4**, were obtained using the same method as SUM159PT. The analyzed cell size, arying from around 14  $\mu\text{m}$  to 18  $\mu\text{m}$ , was smaller than SUM159PT cells.

**Table 4.4** Measured cell size of MCF7

Cell number	Cell size
MCF-1	16.0 $\mu\text{m}$
MCF-2	17.6 $\mu\text{m}$
MCF-3	17.5 $\mu\text{m}$
MCF-4	15.1 $\mu\text{m}$
MCF-5	14.6 $\mu\text{m}$
MCF-6	14.1 $\mu\text{m}$
MCF-7	14.6 $\mu\text{m}$

### 4.3.4 Electrical measurement

Simultaneously with the mechanical detection, electrical property of the cell was characterized by impedance spectroscopy, as shown in **Fig. 4.14**. A fixed SUM159PT was used in this experiment. 1 V<sub>p-p</sub> was applied to the sensing tip by the lock-in amplifier. While sweeping the excitation frequency, the obtained signal such as the dynamic current passing through the opposing compression tips was recorded for three different conditions at in air (grey line), in PBS (No cell, blue line) and in PBS with a fixed SUM159PT cell captured between tips (with cell, red line). The signal obtained from the compression tip was amplified with the transimpedance amplifier with the setting gain of 10<sup>5</sup> V/A and converted to voltage. The electrical measurements were performed in real-time with the mechanical measurements. The spikes in the electrical measurement results were due to the influence of measuring mechanical properties of the captured cell.



**Fig. 4.14** Electrical measurements performed on a cell in PBS solution (red line) and control (no cell in PBS, blue line). Electrical characteristics of the setup (in air) are shown in grey line.

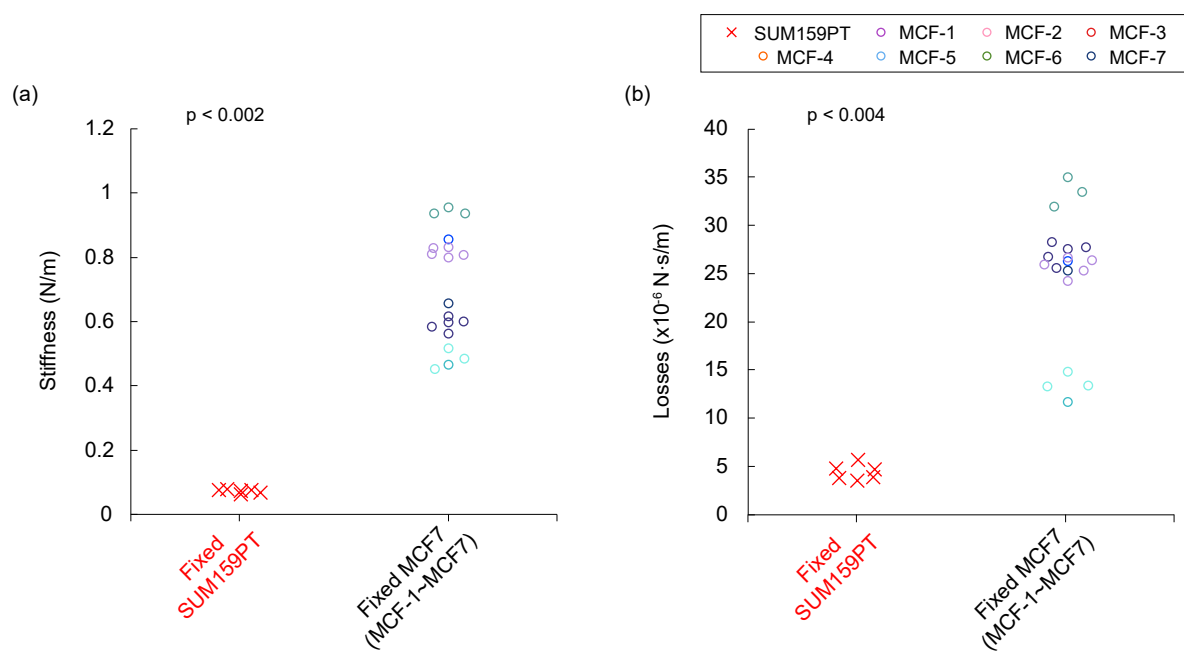
## 4.4 Discussions

### 4.4.1 Comparison between fixed SUM159PT and MCF7

In this chapter, two different human derived breast cancer cell lines, SUM159PT and MCF7, were used in fixed state. SUM159PT has high metastatic potential but MCF7 does not. SNTs were already used to test the possibility of distinguishing different type of the cell based on their

mechanical properties. SNT was able to identify fixed and live SUM159PT cells (**Fig. 2.25**), and also two different cell lines in live state (**Fig. 2.26**). Mechanical properties of a cell, such as the stiffness and the viscous losses, obtained by SNT are potentially used as biomarkers to distinguish cell types without any staining procedures. With the benefit of MEMS, the channel integrated device adopted the same detecting sensitivity as SNT. Thus, the developed device can also be applied to distinguish the type of cells. Here, using the channel integrated device, different fixed cell lines are compared.

From the results of **Fig. 4.12** and **Fig. 4.13 (c),(d)**, the stiffness and the viscous losses of two different cancer cells in fixed state were compared. Since cells were fixed for keeping the stable condition, direct biological implications were not relevant. The extracted data, SUM159PT (in red) and MCF7 (see legends) at 20 % of cell compression, are shown in **Fig. 4.15**.



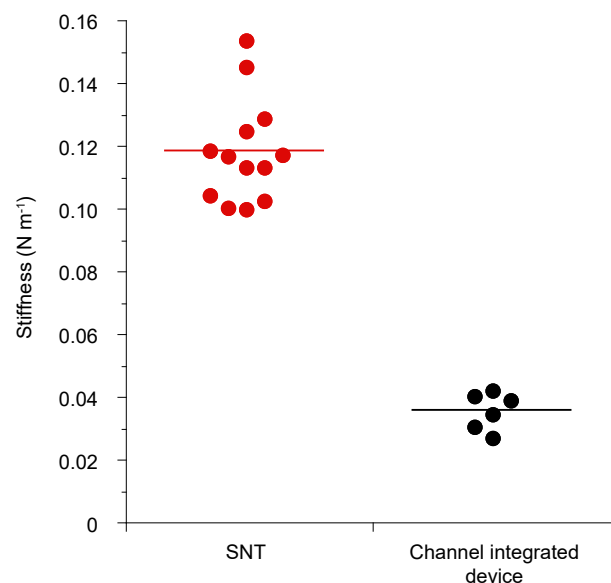
**Fig. 4.15** Comparison between fixed SUM159PT and MCF7 cells extracted at 10 % of the cell compression level. (a) Stiffness, and (b) Viscous losses of the analyzed cell.

Fixed MCF7 cells which included all MCF7 results (MCF-1 ~ MCF-7) was stiffer than fixed SUM159PT cells. A comparison between these two cells showed significant differences to indicate  $p < 0.002$ . SUM159PT, which had softer characteristics and was more flexible than MCF7 due to higher malignancy potential, may possibly show higher success going through a narrow spaces such as the gap between cells in a blood vessel wall, leading to cancer metastasis. Furthermore, SUM159PT cells were demonstrating lower viscous losses compared with MCF7

cells. It showed  $p < 0.004$  to conclude statistical significance of difference on two cell lines. These results indicate that the channel integrated device has enough sensitivity to distinguish two different fixed cancer cells.

#### 4.4.2 Comparison between SNT and the developed MEMS device

All cells measured in the channel integrated device were fixed with 4 % Paraformaldehyde to keep stable condition during measurements as in the case of Silicon Nano Tweezers (SNT). As the main detection and stimulation designs are similar to each other, the obtained results when analysing the same cell line can be expected to have similar values. To compare SNT and the channel integrated device using fixed SUM159PT cells, cells were compressed to be analysed based on their mechanical properties. From both sets of experiments, the 10 % compression level of fixed SUM159PT cells were chosen to be compared based on their stiffness obtained by SNT and by the channel integrated device. The stiffness value of fixed SUM159PT cells obtained by SNT was higher than the stiffness value obtained using the channel integrated device (**Fig. 4.16**) although these values were expected to be similar.



**Fig. 4.16** Comparison the extracted stiffness of fixed SUM159PT cells from 10 % of the cell compression level between (a) SNT, and (b) the channel integrated MEMS device.

The difference in the stiffness values of the same cell line obtained using different devices might be caused by a combination of reasons. One important cause of uncertainty in the stiffness (and viscous losses) calculation was due to the approximated values of the spring constant of

the suspensions and the mass of the moving part of the device. The mass value,  $M$ , used in the equation was derived from the ideal case, which was based on the mask area and the thickness of the wafer. However, there were significant differences among devices especially due to the 350- $\mu\text{m}$  height backside silicon etching process. The mass changed significantly due to the condition of the plasma during the DRIE etching process (side walls being etched obliquely). Another important issue based on fabrication was related to the etching process of the spring structures. Slight differences in the etching process changes the spring constant of the devices (significantly due to the scaling law) which altered the sensitivity of the device. As a result of this, the dimension of a cell could be detected differently from an SNT device to a channel-integrated device. The difference in cell detection was reflected on the compressed values resulting in comparing cells under different compression levels between the SNT device and the channel integrated device. These two reasons were caused by the effect of plasma on the differences in the designs. A third issue was related to the size detection algorithm used in the experiments. There was over 1 year between the experiments performed by SNT and the channel integrated device. This time was used to improve the size-detection algorithm. As a result, the SNT experiments did not have the same sensitivity as the channel integrated device experiments. Similar to the second issue, guaranteeing the results being obtained at the same compression level is not possible. One last point to note is that the objective used for these two experimental setup was different. As a result, although experiments on different cells were performed under the same conditions and protocols for each device type, there were slight differences between different types. Therefore, result comparison among each type of device was performed successfully but each device should be better characterized according to differences in the fabrication process if reliable quantitative results are desired.

## 4.5 Conclusions

The real-time bio sample analysis was performed using a MEMS device with a built-in microfluidic channel. This device could simultaneously characterize bio samples, such as cancer cells, electrically and mechanically. Fixed single cancer cells, SUM159PT and MCF7 from human breast cancer cell lines, were flown in the integrated channel. First, capturing procedure of circulating cells was established. Next, captured fixed single cancer cells were characterized. The repeated compression cycles were applied to the captured cells and their responses were

measured during cell compression in real-time. Using the measurement results, mechanical properties of cells, such as the stiffness and the viscous losses, were calculated, and compared between two different cell lines. SUM159PT cells having higher metastatic potential than MCF7 could be seen in the results as having softer stiffness and lower viscous losses. On the other hand, the results obtained by two different types of devices, that are SNT and the channel integrated device, for the same type of cells were very different. The channel integrated MEMS device and SNT were compared at 10 % compression level of the fixed cell from the same cell line. Although the fixed cells were expected to obtain almost the same value, the cell stiffness measured by SNT was higher than the channel integrated device results. This was possibly due to the differences of the device design which affecting during fabrication processes. As well as, it was due to the effect of developments in the protocols and setup on the detection sensitivity throughout the study. This clearly shows the need to develop protocols to characterize each type of devices more precisely.

# Chapter 5

## Conclusions and future work

### 5.1 Conclusions

In this chapter, the main findings regarding the research questions are summarised. Furthermore, the strengths and limitations of the proposed method and suggestions for further research are presented.

MEMS technology based on Silicon microfabrication for realising devices integrated mechanical elements, sensors, actuators, and electrical circuits provided various application possibilities at the scale of micro/ nano order. Nowadays, devices manufactured by MEMS technology have already been a part of daily life due to a wide range of application fields such as in cars and mobile phones. Moreover, applying MEMS technologies on biological studies has been attracting increasing attention. MEMS, an advanced technology, allows designing and fabricating intricate structures for different biological target samples, such as cells, DNA, proteins, and so on. In this thesis, the development of a new device with integrated built-in microfluidic channel for multi-parameter characterisation of individual cells in suspension, with circulating cancer cells as target, is addressed. Below are the main conclusions emerging from this work.

#### Results of this work

1. As a proof of concept to distinguish individual cancer cells based on physical properties, Atomic Force Microscopy (AFM) and Silicon Nano Tweezers (SNT) were used. AFM is a well established and widely used technique to characterise adherent cells. As a proof of concept to distinguish individual cancer cells based on physical properties, Atomic Force Microscopy (AFM) and Silicon Nano Tweezers (SNT) were used. AFM is a well estab-



lished and widely used technique to characterise adherent cells. Because of this sample preparation characteristics, the different sizes of wells array were applied for capturing and for stopping individual cells in suspension during the cantilever indentation test. However, it was impossible to get the stable measurements. Moreover, it is a time-consuming process to measure an entire cell and also depends on the proficiency of the AFM operator. To provide higher throughput than AFM, the techniques combining microfluidic technologies were applied, such as SNT with a separated microfluidic device. Fundamental microfabrication techniques allow optimising the MEMS device by redesigning and testing several SNT parameters (spring constant, actuation voltage, etc.). SNT could distinguish the following types of cells: (1) fixed and live cancer cells (of the same cell line), and (2) two different cancer cell lines having different cancer metastatic properties. The throughput obtained with SNT approach was far low from providing the statistically significant amount of information. The measurement capabilities were adequate, however, it was crucial to develop a new cell handling approach for higher throughput.

2. A novel built-in microfluidic channel MEMS device was proposed to achieve higher throughput. Similar to SNT, this device was capable of measuring cancer cells physical properties using multi-parameter measurements of single cells in non-adherent/suspension state. Thus, the optimal parameters that were found by SNT to be suitable for distinguishing cells for the label-free detection method could be measured by the new device. The main advantages compared to the SNT system was the positioning of single cells directly at the characterisation area without any assembly and positioning actions between the SNT and the microfluidics device, and also between the SNT tips and the cells. This advantage is the key point improving the throughput without compromising the sensitivity. Moreover, the device provides simultaneous electrical and mechanical measurements targeting various parameters, such as cell size, stiffness, viscous losses, and cytoplasm resistivity.
3. The main structures of the channel integrated MEMS device, such as the compression part, the sensor part, two tips for handling the bio sample, and sidewalls of microfluidic channel, were fabricated in the frontside Si of an SOI wafer. The bottom of the channel consisted of the backside Si. All movable parts could actuate freely as the backside was completely etched, except the channel part (movable parts were connected to the frontside Si through anchors). However, two tips which inserted into the channel from the both side direction

of the channel overlapped with the channel bottom in the design. To allow the actuating elements move freely, the 2- $\mu\text{m}$  BOX layer of SOI under the two tips was removed by HF. The integrated channel was approximately 100  $\mu\text{m}$  in width. The width of channel became narrower by the tips reaching down to 20  $\mu\text{m}$  at the tips part (the gap distance between tips was 20  $\mu\text{m}$ ).

4. To complete the channel, a PDMS cover was placed on the top part of the channel. Although the PDMS cover was designed to cover up the entire device except electrical pads to connect with PCB, the cover maintained a space about 10  $\mu\text{m}$  above the moving part not to disturb the movement of the movable parts, including the compression part, the sensor part, and two tips that formed with the frontside Si of the SOI wafer. Despite the 10- $\mu\text{m}$  height difference, the air-liquid interface did not leak owing to the surface tension of the liquid flowing in the channel. Note that using a liquid with lower surface tension, such as ethanol, made it difficult to keep the air-liquid interface.
5. The preliminary tests of the developed device for mechanical and electrical measurements were done with different concentration of glucose solutions and NaCl solutions. The channel integrated device could successfully detect differences among these solutions.
6. The mechanical and electrical properties of cancer cells were evaluated with the proposed device. During a cell compression cycle, the size of a cell could be detected at the initial moment the cell was sensed. The cell size was calculated by subtracting the the displacement obtained at the applied potential difference from the initial gap between the two tips, that is 20  $\mu\text{m}$ .
7. The channel-integrated MEMS device was used to compare two types of human breast cancer cell lines, SUM159PT and MCF7, that were fixed with 4 % Paraformaldehyde. Mechanical properties of cells, including the stiffness and the viscous losses, derived from the experimental results. SUM159PT cells, known to have higher metastatic potentials than MCF7 cells, were softer with lower viscous losses.

As a result, this research shows that MEMS technology, with a  $1 \times 1.5\text{-cm}$  MEMS device, can be used to handle single cells for simultaneous electrical and mechanical characterisation to detect differences among cell lines.

## 5.2 Recommendations for further research

This study successfully build up the design, fabrication and application trials to develop a high-throughput device for single cell characterization. However, there are still many points to improve in the future. Future work concerns deeper analysis of single cancer cells and new proposals to optimise the device for specific targets. There are some ideas that I would have liked to try during the development of the channel integrated device described in **Chapter 3**. The following points to be improved are described below:

### 1. Device

- (a) The long distance actuation of the compression tip was designed and realised. It was achieved 16.6  $\mu\text{m}$  of movement when applied 110 V on the compression side of comb drive actuator. However, it is better to use the low voltage to actuate the tip because the electrical breakage of BOX layer may happen if the applied voltage is too high. With a softer spring constant, the same actuation distance can be possible with a lower actuation voltage.
- (b) The contact area of the Si device with the PDMS cover requires certain area to attach well. This is because there is no permanent bonding. An optimised attachment (and alignment) process can miniaturise the device even further to improve the fabrication yield.
- (c) The narrowest part of the channel is designed to be 20  $\mu\text{m}$  as the gap between two tips. A filter can be used near the channel inlet (e.g., pillar arrays) to trap cells larger than 20  $\mu\text{m}$ . As a result, larger cells can be prohibited to enter the channel, which minimises possible clogging of the channel.
- (d) By creating branches downstream of the microfluidic channel, characterized cells can then be sorted later. Sorted cells can be tested with other analyse methods to derive new parameters other than the physical properties of the single cell.
- (e) Since a lipid bilayer membrane on the surface of living cell tends to adhere to silicon surface, this problem can be solved by carrying out the surface treatment of the channel and the tips (e.g., Pluronic F68) before performing experiments using cells similar to the case of tweezers.

- (f) In the future, it will be necessary to do a calibration of the fabricated device one by one. At present, the spring constant of the device is set using an ideal value estimated from the design. With this estimated spring constant, information of the cell (e.g., stiffness and viscous losses) are calculated. However, each device has dispersion (difference) due to the fabrication. There are differences in the etching rate of Si between the outer and inner positions of the wafer. Accordingly, each device has a slight difference in the beam width used for calculating the spring constant. Also, the mass of backside Si that mechanically supports of the movable structures have difference due to the taper shape of etching wall. By measuring them, it will be possible to perform correct calibration on each device.
- (g) By performing the above calibration, quantitative information of the cell can be obtained more accurately. The cell information such as the cell stiffness and the viscous losses largely depend on the calibration of the each device because it will be obtained by subtracting the control experiment (results of device only) measured in advance.
- (h) The calibrated device is used to acquire enough information on various physical parameters of the cell such as membrane capacitance, cytoplasm resistivity, shape recovery time in addition to the demonstrated parameters. By measuring various parameters based on mechanical and electrical properties and collecting the cell data, it should be possible to distinguish the cell metastatic potential without staining the cell.

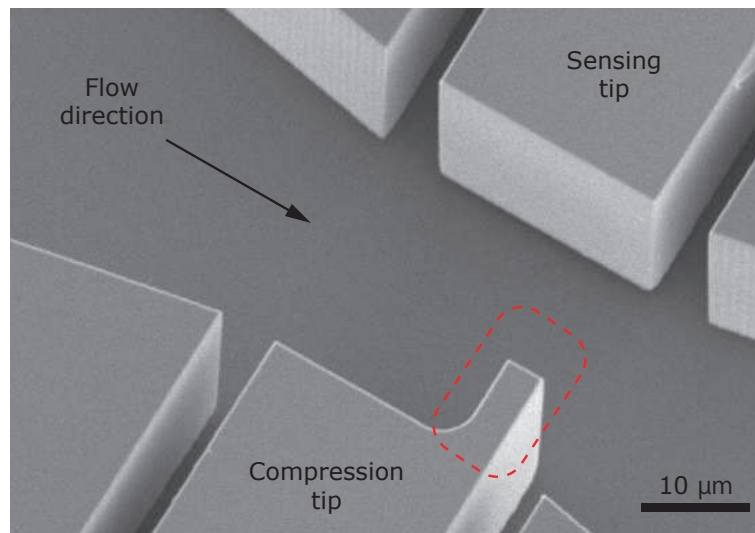
## 2. PDMS

- (a) The demonstrated PDMS cover had the bottom surface at two different height. The lowest surface corresponded to the area attaching the silicon device. The second level of the surface corresponded to the area overlapping with the mobile parts of the MEMS device. For simplicity, the demonstrated devices had the same gap between the PDMS cover and the mobile parts of the device and this gap was chosen to minimise the air-liquid interface around the tips. However, increasing the gap above the actuating and sensing elements decreases air damping and improves the overall performance of the proposed device. Thus, a third level of bottom PDMS surface can be highly beneficial by performing a 2-layer SU8 mould fabrication.

- (b) The metal tube is penetrated to the outlet of PDMS due to the connection to the tube which goes to the vacuum pump. If it is not straight penetrating, the PDMS shape will become deformed. Also, the hardness of PDMS sheet is better to use the hard and thick one. This is because if it is too soft and thin, the PDMS sheet bends during the alignment with the Si device. At least, it need to keep its flatness during it picked up by the tweezers.
- (c) The tube which connected to the vacuum pump requires to have the long enough length. If it will be too short of the length, the tension by tube itself breaks the contact between Si device and the PDMS cover.

### 3. Flow

- (a) It could be interesting to consider the way to stop the single cell in the certain position such as between the tips. For now, the capturing protocol of the cell uses the flow in the channel, but it is particularly difficult to arrange the cell. To fabricate a mechanical stopper, such as an extended bar from the tip, it makes easier to stop the flowing cell (**Fig. 5.1**). By solving this cell capturing protocol, the measurement throughput will be possibly improved.



**Fig. 5.1** Fabricated the L-shaped compression tip for easier capturing the cell.

- (b) The single suspension cell was injected into the channel inlet, however, there was no system to send the cell to the channel one by one. Sometimes, two single cells have come at a time. Also, it was impossible to know when the cell will arrive at the handling part. Integrating the device with methods transporting cells regularly, such as flow focusing, can improve the cell handling and thus the throughput.

#### 4. Cell

- (a) Further study is still required to collect cells information on different cell lines, especially to study the metastatic potential of cells.

Improving the developed MEMS device (with a built-in channel) according to the proposed steps leads to an effective method characterising mechanical and electrical properties that can be used for cancer diagnosis and drug testing in the future.

# References

- [1] B.W. Stewart and C.P. Wild (Eds.), “World Cancer Report 2014”, International Agency for Research on Cancer, World Health Organization, ISBN: 978-92-832-0429-9, 2014.
- [2] M. Malvezzi, G. Carioli, P. Bertuccio, P. Boffetta, F. Levi, C. La Vecchia and E. Negri, “European cancer mortality predictions for the year 2018 with focus on colorectal cancer”, *Annals of Oncology*, Vol. 29, No. 4, pp. 1016-1022, 2018.  
DOI: <https://doi.org/10.1093/annonc/mdy033>
- [3] D. M. Gonzalez and D. Medici, “Signaling mechanisms of the epithelial-mesenchymal transition”, *Science Signaling*, Vol. 7, No. 344, pp. re8-re8, 2014.  
DOI: <https://doi.org/10.1126/scisignal.2005189>
- [4] T. Brabletz, “EMT and MET in Metastasis: Where Are the Cancer Stem Cells?”, *Cancer Cell*, Vol. 22, No. 6, pp. 699-701, 2012.  
DOI: <https://doi.org/10.1016/j.ccr.2012.11.009>
- [5] A. M. Haslehurst, M. Koti, M. Dharsee, P. Nuin, K. Evans, J. Geraci, T. Childs, J. Chen, J. Li, J. Weberpals, S. Davey, J. Squire, P. C. Park and H. Feilotter, “EMT Transcription Factors Snail and Slug Directly Contribute to Cisplatin Resistance in Ovarian Cancer”, *BMC Cancer*, Vol. 12, No. 1, pp.91, 2012.  
DOI: <https://doi.org/10.1186/1471-2407-12-91>
- [6] A. Singh and J. Settleman, “EMT, Cancer Stem Cells and Drug Resistance”, *Oncogene*, Vol. 29, No. 34, pp. 4741–4751, 2010.  
DOI: <https://doi.org/10.1038/onc.2010.215>
- [7] K. Wolf, M. te Lindert, M. Krause, S. Alexander, J. te Riet, A.L. Willis, R.M. Hoffman, C.G. Figdor, S.J. Weiss, and P. Friedl, “Physical limits of cell migration: Control by ECM space and nuclear deformation and tuning by proteolysis and traction force”, *The Journal of Cell Biology*, Vol. 201, No. 7, pp. 1069-1084, 2013.  
DOI: <https://doi.org/10.1083/jcb.201210152>
- [8] S. Suresh, “Nanomedicine: Elastic clues in cancer detection”, *Nature nanotechnology*, Vol. 2, pp. 748-749, 2007.
- [9] S. Suresh, J. Spatz, J.P. Mills, A. Micoulet, M. Dao, C.T. Lim, M. Beil, and T. Seufferlein, “Connections between single-cell biomechanics and human disease states: gastrointestinal cancer and malaria”, *Acta Biomaterialia*, Vol. 1, No. 1, pp. 15-30, 2005.  
DOI: <https://doi.org/10.1016/j.actbio.2004.09.001>
- [10] G. Bao, and S. Suresh, “Cell and molecular mechanics of biological materials”, *Nature Materials*, Vol. 2, No. 11, pp. 715-725. 2003.  
DOI: <https://doi.org/10.1038/nmat1001>

- [11] K.A. Ward, Wen-I. Li, S. Zimmer, T. Davis, "Viscoelastic properties of transformed cells: Role in tumor cell progression and metastasis formation", *Biorheology*, Vol. 28, No. 3-4, pp. 301-313, 1991.  
DOI: <http://dx.doi.org/10.3233/BIR-1991-283-419>
- [12] E.H. Zhou, S.T. Quek, and C.T. Lim, "Power-law rheology analysis of cells undergoing micropipette aspiration", *Biomech Model Mechanobiol*, Vol. 9, No. 5, pp. 563-572, 2010.  
DOI: <http://dx.doi.org/10.1007/s10237-010-0197-7>
- [13] G. Zhang, M. Long, Z. Wu, and W. Yu, "Mechanical Properties of Hepatocellular Carcinoma Cells", *World Journal of Gastroenterology*, Vol. 8, No. 2, pp. 243-246, 2002.  
DOI: <https://doi.org/10.3748/wjg.v8.i2.243>
- [14] Y-S. Chu, S. Dufour, J.P. Thiery, E.Perez, and F. Pincet, "Johnson-Kendall-Roberts Theory Applied to Living Cells", *Physical Review Journals*, Vol. 94, No. 2, pp.028102, 2005.  
DOI: <https://doi.org/10.1103/PhysRevLett.94.028102>
- [15] E. Shojaei-Baghini, Y. Zheng, M.A.S. Jewett, W.B. Geddie, and Y. Sun, "Mechanical Characterization of Benign and Malignant Urothelial Cells from Voided Urine", *Applied Physics Letters*, Vol. 102, No. 12, pp. 123704, 2013.  
DOI: <https://doi.org/10.1063/1.4798495>.
- [16] Y. Zheng, J. Wen, J. Nguyen, M.A. Cachia, C. Wang, and Y. Sun, "Decreased Deformability of Lymphocytes in Chronic Lymphocytic Leukemia", *Scientific Reports*, Vol. 5, No. 1, pp. 7613, 2015.  
DOI: <https://doi.org/10.1038/srep07613>
- [17] M. Radmacher, M. Fritz, C. M. Kacher, J. P. Cleveland, and P. K. Hansma, "Measuring the viscoelastic properties of human platelets with the atomic force microscope", *Biophysical Journal*, Vol. 70, No. 1, pp. 556-567, 1996.  
DOI: [https://doi.org/10.1016/S0006-3495\(96\)79602-9](https://doi.org/10.1016/S0006-3495(96)79602-9)
- [18] Y. Wang, C. Xu, N. Jiang, L. Zheng, J. Zeng, C. Qiu, H. Yang, and S. Xie, "Quantitative Analysis of the Cell-Surface Roughness and Viscoelasticity for Breast Cancer Cells Discrimination Using Atomic Force Microscopy: Roughness and Viscoelasticity of Breast Cancer Cells", *Scanning*, Vol. 38, No. 6, pp. 558-563, 2016.  
DOI: <https://doi.org/10.1002/sca.21300>
- [19] M. Nikkhah, J.S. Strobl, R.D. Vita, and M. Agah, "The Cytoskeletal Organization of Breast Carcinoma and Fibroblast Cells inside Three Dimensional (3-D) Isotropic Silicon Microstructures", *Biomaterials*, Vol. 31, No. 16, pp. 4552-4561, 2010.  
DOI: <https://doi.org/10.1016/j.biomaterials.2010.02.034>
- [20] A.N. Ketene, E.M. Schmelz, P.C. Roberts, M. Agah, "The effects of cancer progression on the viscoelasticity of ovarian cell cytoskeleton structures", *Nanomedicine: Nanotechnology, Biology and Medicine*, Vol. 8 No. 1, pp. 93-102, 2012.  
DOI: <https://doi.org/10.1016/j.nano.2011.05.012>
- [21] D. Kirmizis, "Atomic Force Microscopy Probing in the Measurement of Cell Mechanics", *International Journal of Nanomedicine*, Vol. 137, 2010.  
DOI: <https://doi.org/10.2147/IJN.S5787>
- [22] Y.M. Efremov, W.-H. Wang, S.D. Hardy, R.L. Geahlen, and A. Raman, "Measuring Nanoscale Viscoelastic Parameters of Cells Directly from AFM Force-Displacement



- Curves”, *Scientific Reports*, Vol. 7, No. 1, 2017.  
DOI: <https://doi.org/10.1038/s41598-017-01784-3>
- [23] S.E. Cross, Y.-S. Jin, J. Rao, and J.K. Gimzewski, “Nanomechanical Analysis of Cells from Cancer Patients”, *Nature Nanotechnology*, Vol. 2, No. 12, pp. 780-783, 2007.  
DOI: <https://doi.org/10.1038/nnaNo.2007.388>
- [24] S.E. Cross, Y.-S. Jin, Q.-Y. Lu, J. Rao, and J.K. Gimzewski, “Green Tea Extract Selectively Targets Nanomechanics of Live Metastatic Cancer Cells”, *Nanotechnology*, Vol. 22, No. 21, pp. 215101, 2011.  
DOI: <https://doi.org/10.1088/0957-4484/22/21/215101>
- [25] H. Zoellner, N. Paknejad, K. Manova, and M.A.S. Moore, “A Novel Cell-Stiffness-Fingerprinting Analysis by Scanning Atomic Force Microscopy: Comparison of Fibroblasts and Diverse Cancer Cell Lines”, *Histochemistry and Cell Biology*, Vol. 144, No. 6, pp. 533-542, 2015.  
DOI: <https://doi.org/10.1007/s00418-015-1363-x>
- [26] J.A. Hessler, A. Budor, K. Putschakayala, A. Mecke, D. Rieger, Mark M.B. Holl, B.G. Orr, A. Bielinska, J. Beals, and J. Baker. “Atomic Force Microscopy Study of Early Morphological Changes during Apoptosis”, *Langmuir*, Vol. 21, No. 20, pp. 9280-9286, 2005.  
DOI: <https://doi.org/10.1021/la051837>
- [27] K.J. Van Vliet, G. Bao, S. Suresh, “The biomechanics toolbox: experimental approaches to living cells and biomolecules”, *Acta Materialia*, Vol. 51, Issue 19, pp. 5881-5905, 2003.  
DOI: <https://doi.org/10.1016/j.actamat.2003.09.001>
- [28] B.J. Haupt, A.E. Pelling, and M.A. Horton, “Integrated Confocal and Scanning Probe Microscopy for Biomedical Research”, *The Scientific World Journal*, Vol. 6, pp. 1609-1618, 2006.  
DOI: <https://doi.org/10.1100/tsw.2006.269>
- [29] M. Lekka, P. Laidler, D. Gil, J. Lekki, Z. Stachura, and A.Z. Hryniewicz, “Elasticity of Normal and Cancerous Human Bladder Cells Studied by Scanning Force Microscopy”, *European Biophysics Journal*, Vol. 28, No. 4, pp. 312-316, 1999.  
DOI: <https://doi.org/10.1007/s002490050213>
- [30] M. Lekka and P. Laidler, “Applicability of AFM in cancer detection”, *Nature Nanotechnology*, Vol. 4, pp. 72-72, 2009.  
DOI: <https://doi.org/10.1038/nnano.2009.004>
- [31] C. Rotsch and M. Radmacher, “Drug-induced changes of cytoskeletal structure and mechanics in fibroblasts: An atomic force microscopy study”, *Biophysical Journal*, Vol. 78, pp. 520-535, 2000.
- [32] G.Y.H. Lee, and C.T. Lim, “Biomechanics approaches to studying human diseases”, *Trends in Biotechnology*, Vol. 25, No. 3, pp. 111-118, 2007.
- [33] W. Xu, R. Mezencev, B. Kim, L. Wang, J. McDonald, and T. Sulchek, “Cell Stiffness Is a Biomarker of the Metastatic Potential of Ovarian Cancer Cells”, Edited by Surinder K. Batra., *PLoS ONE*, Vol. 7, No. 10 , pp. e46609, 2012.  
DOI: <https://doi.org/10.1371/journal.pone.0046609>

- [34] S.E. Cross, Y.-S. Jin, J. Tondre, R. Wong, J. Rao, and J.K. Gimzewski, "AFM-Based Analysis of Human Metastatic Cancer Cells", *Nanotechnology*, Vol. 19, No. 38, pp. 384003, 2008.  
DOI: <https://doi.org/10.1088/0957-4484/19/38/384003>
- [35] E.M. Darling, S. Zauscher, J.A. Block, and F. Guilak, "A Thin-Layer Model for Viscoelastic, Stress-Relaxation Testing of Cells Using Atomic Force Microscopy: Do Cell Properties Reflect Metastatic Potential?", *Biophysical Journal*, Vol. 92, No. 5, pp. 1784-1791, 2007.  
DOI: <https://doi.org/10.1529/biophysj.106.083097>
- [36] Li, Q.S., G.Y.H. Lee, C.N. Ong, and C.T. Lim, "AFM Indentation Study of Breast Cancer Cells", *Biochemical and Biophysical Research Communications*, Vol. 374, No. 4, pp. 609-613, 2008.  
DOI: <https://doi.org/10.1016/j.bbrc.2008.07.078>
- [37] K. Hayashi, and M. Iwata, "Stiffness of Cancer Cells Measured with an AFM Indentation Method", *Journal of the Mechanical Behavior of Biomedical Materials*, Vol. 49, pp. 105-111, 2015.  
DOI: <https://doi.org/10.1016/j.jmbbm.2015.04.030>
- [38] M. Lekka, "Discrimination Between Normal and Cancerous Cells Using AFM", *Bio-NanoScience*, Vol. 6, No. 1, pp. 65-80, 2016.  
DOI: <https://doi.org/10.1007/s12668-016-0191-3>
- [39] M. Lekka, and J. Wiltowska-Zuber. "Biomedical Applications of AFM". *Journal of Physics, Conference Series*, Vol. 146, pp. 012023, 2009.  
DOI: <https://doi.org/10.1088/1742-6596/146/1/012023>
- [40] Y. Ding, G.-K. Xu, and G.-F. Wang, "On the Determination of Elastic Moduli of Cells by AFM Based Indentation", *Scientific Reports*, Vol. 7, pp. 45575, 2017.  
DOI: <https://doi.org/10.1038/srep45575>
- [41] D.R. Gossett, H.T.K. Tse, S.A. Lee, Y. Ying, A.G. Lindgren, O.O. Yang, J. Rao, A.T. Clark and D.D. Carlo, "Hydrodynamic stretching of single cells for large population mechanical phenotyping", *PNAS*, Vol. 109, No. 20, pp. 7630-7635, 2012.  
DOI: <https://doi.org/10.1073/pnas.1200107109>
- [42] O. Oliver, P. Rosendahl, A. Mietke, S. Golfier, C. Herold, D. Klaue, S. Girardo, S. Pagliara, A. Ekpenyong, A. Jacobi, M. Wobus, N. Töpfner, U.F. Keyser, J. Mansfeld, E. Fischer-Friedrich, and J. Guck, "Real-Time Deformability Cytometry: On-the-Fly Cell Mechanical Phenotyping", *Nature Methods*, Vol. 12, No. 3, pp. 199-202, 2015.  
DOI: <https://doi.org/10.1038/nmeth.3281>
- [43] H.T.K. Tse, D.R. Gossett, Y.S. Moon, M. Masaeli, M. Sohsman, Y. Ying, K. Mislick, R.P. Adams, J. Rao, and D.D. Carlo, "Quantitative Diagnosis of Malignant Pleural Effusions by Single-Cell Mechanophenotyping". *Science Translational Medicine*, Vol. 5, Issue. 212, pp. 212ra163, 2013.  
DOI: <https://doi.org/10.1126/scitranslmed.3006559>
- [44] N. Wang, J. P. Butler, and D. E. Ingber, "Mechanotransduction across the cell surface and through the cytoskeleton". *Science*, Vol. 260, pp. 1124-1127, 1993.  
DOI: [https://doi.org/10.1016/0962-8924\(93\)90050-B](https://doi.org/10.1016/0962-8924(93)90050-B)

- [45] J. Wilhelm and E. Frey, "Elasticity of stiff polymer networks". *Phys. Rev. Lett.*, Vol. 91, No. 10, 108103, 2003.
- [46] O. Thoumine and A. Ott, "Comparison of the mechanical properties of normal and transformed fibroblasts". *Biorheology*. Vol. 34, Issues 4-5, pp. 309-326, 1997.
- [47] Sleep, J., D. Wilson, R. Simmons, and W. Gratzner. "Elasticity of the red cell membrane and its relation to hemolytic disorders: an optical tweezers study". *Biophysical Journal*. Vol. 77, pp. 3085-3095, 1999.
- [48] Dao, M., C.T. Lim, and S. Suresh. "Mechanics of the Human Red Blood Cell Deformed by Optical Tweezers". *Journal of the Mechanics and Physics of Solids*, Vol. 51, No. 11-12, pp. 2259-2280, 2003. DOI: <https://doi.org/10.1016/j.jmps.2003.09.019>
- [49] Mills, J. P., L. Qie, M. Dao, C. T. Lim, and S. Suresh. "Nonlinear Elastic and Viscoelastic Deformation of the Human Red Blood Cell with Optical Tweezers". *MCB Tech Science Press*, Vol. 1, No. 3, pp. 169-180, 2004.
- [50] Wolfgang Schulz, "Molecular Biology of Human Cancer, An Advanced Student's Text-book". Springer Netherlands, 978-1-4020-3186-1, Chapter 9, 2007,
- [51] Hanahan, Douglas, and Robert A. Weinberg. "Hallmarks of Cancer: The Next Generation". *Cell*, Vol. 144, No. 5, pp. 646-674, 2011.  
DOI: <https://doi.org/10.1016/j.cell.2011.02.013>
- [52] Banyard, Jacqueline, and Diane R. Bielenberg. "The Role of EMT and MET in Cancer Dissemination". *Connective Tissue Research*, Vol. 56, No. 5, pp. 403-413, 2015.  
DOI: <https://doi.org/10.3109/03008207.2015.1060970>
- [53] Talmadge, J. E., and I. J. Fidler. "AACR Centennial Series: The Biology of Cancer Metastasis: Historical Perspective". *Cancer Research*, Vol. 70, No. 14, pp. 5649-5669, 2010.  
DOI: <https://doi.org/10.1158/0008-5472.CAN-10-1040>
- [54] Wyckoff, Jeffrey B, Joan G Jones, John S Condeelis, and Jeffrey E Segall. A Critical Step in Metastasis: In Vivo Analysis of Intravasation at the Primary Tumor". *Cancer Research*, Vol. 60, No. 9, pp. 2504-2511, 2000.
- [55] Mitchell, Michael J, and Michael R King. "Unnatural Killer Cells to Prevent Bloodborne Metastasis: Inspiration from Biology and Engineering". *Expert Review of Anticancer Therapy*, Vol. 14, No. 6, pp. 641-644, 2014.  
DOI: <https://doi.org/10.1586/14737140.2014.916619>
- [56] H. Fujita, "A DECADE OF MEMS AND ITS FUTURE", *Proceedings IEEE The Tenth Annual International Workshop on Micro Electro Mechanical Systems. An Investigation of Micro Structures, Sensors, Actuators, Machines and Robots*, pp. 56372459, 1997.  
DOI: <http://dx.doi.org/10.1109/MEMSYS.1997.581729>
- [57] K.E. Petersen, "Silicon as a Mechanical Material", *Proceedings of the IEEE*, Vol. 70, No. 5, pp. 420-457, 1982.  
DOI: <http://dx.doi.org/10.1109/PROC.1982.12331>
- [58] Prime Faraday Partnership, "Technology Watch, An Introduction to MEMS (Micro-electromechanical Systems)", ISBN 1-84402-020-7, 2002.

- [59] E. Mounier, “Extracted from: Status of the MEMS Industry report”, Yole Développement, May 2018.  
<https://electroiq.com/2018/06/the-mems-market-is-showing-a-17-5-cagr-between-2018-and-2023/>
- [60] “BioMEMS Market Size, Industry Analysis Report, Regional Outlook (U.S., Germany, UK, Italy, Russia, China, India, Japan, South Korea, Brazil, Mexico, Saudi Arabia, UAE, South Africa)”. Application Development, Price Trend, Competitive Market Share & Forecast, 2016 - 2023. Global Market Insights, Insights to innovation.  
Report ID: GMI344 <https://www.gminsights.com/industry-analysis/biomems-market>
- [61] J. Voldman, M. L. Gray, and M. A. Schmidt, “Microfabrication in Biology and Medicine”, *Annual Review of Biomedical Engineering*, Vol. 1, pp. 401-425, 1999.  
DOI: <https://doi.org/10.1146/annurev.bioeng.1.1.401>
- [62] S. Sant, S. L. Tao, O. Z. Fisher, Q. Xu, N. A. Peppas, and A. Khademhosseini, “Microfabrication technologies for oral drug delivery”, *Advanced Drug Delivery Reviews*, Vol. 64, No. 6, pp. 496-507, 2012.  
DOI: <https://doi.org/10.1016/j.addr.2011.11.013>
- [63] R. R. Jivani, G. J. Lakhtaria, D. D. Patadiya, L. D. Patel, N. P. Jivani, and B. P. Jhala, “Biomedical microelectromechanical systems (BioMEMS): Revolution in drug delivery and analytical techniques”, *Saudi Pharmaceutical Journal*, Vol. 24, No. 1, pp. 1-20, 2016.  
DOI: <https://doi.org/10.1016/j.jsps.2013.12.003>
- [64] S. Sant, S. L. Tao, O. Z. Fisher, Q. Xu, N. A. Peppas, and A. Khademhosseini, “Microfabrication technologies for oral drug delivery”, *Advanced Drug Delivery Reviews*, Vol. 64, No. 6, pp. 496-507, 2012.  
DOI: <https://doi.org/10.1016/j.addr.2011.11.013>
- [65] E. Larrañeta, R. E. M. Lutton, A. D. Woolfson, and R. F. Donnelly, “Microneedle arrays as transdermal and intradermal drug delivery systems: Materials science, manufacture and commercial development”, *Materials Science and Engineering: R: Reports*, Vol. 104, pp. 1-32, 2016.  
DOI: <https://doi.org/10.1016/j.mser.2016.03.001>
- [66] C. Moraes, G. Mehta, S. C. Leshner-Perez, and S. Takayama, “Organs-on-a-Chip: A Focus on Compartmentalized Microdevices”, *Annals of Biomedical Engineering*, Vol. 40, No. 6, pp. 1211-1227, 2012.  
DOI: <https://doi.org/10.1007/s10439-011-0455-6>
- [67] D. Huh, B. D. Matthews, A. Mammoto, M. Montoya-Zavala, H. Y. Hsin, and D. E. Ingber, “Reconstituting Organ-Level Lung Functions on a Chip”, *Science*, Vol. 328, No. 5986, pp. 1662-1668, 2010.  
DOI: <https://doi.org/10.1126/science.1188302>
- [68] M. B. Esch, T. L. King, and M. L. Shuler, “The Role of Body-on-a-Chip Devices in Drug and Toxicity Studies”, *Annual Review of Biomedical Engineering*, Vol. 13, No. 1, pp. 55-72, 2011.  
DOI: <https://doi.org/10.1146/annurev-bioeng-071910-124629>
- [69] Hou, H. W., Q. S. Li, G. Y. H. Lee, A. P. Kumar, C. N. Ong, and C. T. Lim. “Deformability Study of Breast Cancer Cells Using Microfluidics”. *Biomedical Microdevices*, Vol. 11, No. 3, pp. 557-564, 2009.  
DOI: <https://doi.org/10.1007/s10544-008-9262-8>

- [70] Moon, Hui-Sung, Kiho Kwon, Kyung-A. Hyun, Tae Seok Sim, Jae Chan Park, Jeong-Gun Lee, and Hyo-II Jung. “Continual Collection and Re-Separation of Circulating Tumor Cells from Blood Using Multi-Stage Multi-Orifice Flow Fractionation”. *Biomicrofluidics*, Vol. 7, No. 1, pp. 014105, 2013.
- [71] Chen, Jian, Jason Li, and Yu Sun. “Microfluidic Approaches for Cancer Cell Detection, Characterization, and Separation”. *Lab on a Chip*, Vol. 12, No. 10, pp. 1753, 2012.  
DOI: <https://doi.org/10.1039/c2lc21273k>
- [72] Guck, Jochen, Stefan Schinkinger, Bryan Lincoln, Falk Wottawah, Susanne Ebert, Maren Romeyke, Dominik Lenz, “Optical deformability as an inherent cell marker for testing malignant transformation and metastatic competence”. *Biophysical Journal*, Vol. 88, pp. 3689-3698, 2005.  
DOI: <https://doi.org/10.1529/biophysj.104.045476>
- [73] J. Guck, and Edwin R. Chilvers. “Mechanics Meets Medicine”. *Science Translational Medicine* Vol. 5, Issue. 212, 212fs41-212fs41, 2013.  
DOI: <https://doi.org/10.1126/scitranslmed.3007731>
- [74] C. Yamahata, D. Collard, B. Legrand, T. Takekawa, M. Kumemura, G. Hashiguchi, and H. Fujita, “Silicon Nanotweezers With Subnanometer Resolution for the Micromanipulation of Biomolecules”, *Journal of Microelectromechanical Systems*, Vol. 17, No. 3, pp. 623-631, 2008.  
DOI: <https://doi.org/10.1109/JMEMS.2008.922080>
- [75] C. Yamahata, T. Takekawa, M. Kumemura, M. Hosogi, G. Hashiguchi, D. Collard and H. Fujita, “Silicon nanotweezers with adjustable and controllable gap for the manipulation and characterization of DNA molecules”, *International Conference on Microtechnologies in Medicine and Biology*, pp. 123–126, 2006.
- [76] M.C. Tarhan, R. Yokokawa, L. Jalabert, D. Collard, and H. Fujita. “Pick-and-Place Assembly of Single Microtubules”. *Small*, Vol. 13, No. 32, pp. 1701136, 2017.  
DOI: <https://doi.org/10.1002/smll.201701136>
- [77] Lafitte, Nicolas, Hervé Guillou, Momoko Kumemura, Laurent Jalabert, Teruo Fujii, Hiroyuki Fujita, and Dominique Collard. “Integrated MEMS Platform with Silicon Nanotweezers and Open Microfluidic Device for Real-Time and Routine Biomechanical Probing on Molecules and Cells”. In *Engineering in Medicine and Biology Society (EMBC), 35th Annual International Conference of the IEEE*, pp. 148-151. IEEE, 2013.  
DOI: <http://ieeexplore.ieee.org/abstract/document/6609459/>
- [78] Tarhan, Mehmet C., Dominique Collard, Laurent Jalabert, Momoko Kumemura, Nicolas Lafitte, Quentin Delouvee, Stanislav L. Karsten, and Hiroyuki Fujita. “Continuous Real-Time Monitoring of Molecular Detection by Silicon Nanotweezers-Integrated Microfluidic Device”. *16th International Conference on Miniaturized Systems for Chemistry and Life Sciences (microTAS’ 12)*, 2012.
- [79] M.C. Tarhan, N. Lafitte, Y. Tauran, L. Jalabert, M. Kumemura, G. Perret, B.J. Kim, A.W. Coleman, H. Fujita, and D. Collard, “A Rapid and Practical Technique for Real-Time Monitoring of Biomolecular Interactions Using Mechanical Responses of Macromolecules”. *Scientific Reports*, Vol. 6, pp.28001, 2016.  
DOI: <https://doi.org/10.1038/srep28001>

- [80] Y. Tauran, M.C. Tarhan, L. Mollet, J.B. Gerves, M. Kumemura, L. Jalabert, N. Lafitte, I. Byun, B.J. Kim, H. Fujita, D. Collard, F. Perret, K. Suwinska, C. Goutaudier and A.W. Coleman, “Elucidating the mechanism of the considerable mechanical stiffening of DNA induced by the couple  $Zn^{2+}$ /Calix[4]arene-1,3-Odiphosphorous acid”. *Scientific Reports*, Vol. 8, 1226, 2018.  
DOI: <https://10.1038/s41598-018-19712-4>
- [81] I. Montasser, A.W. Coleman, Y. Tauran, L. Jalabert, D. Collard, B.J. Kim and M.C. Tarhan, “Direct measurement of the mechanism by which Magnesium specifically modifies the mechanical properties of DNA”. *Biomicrofluidics*, Vol. 11, No. 5, 051102, 2017.  
DOI: <https://10.1063/1.5008622>
- [82] Guillou, H., N. Lafitte, R. Léal, L. Jalabert, T. Fujii, H. Fujita, Y. T. Matsunaga, and D. Collard, “Silicon Nanotweezers with Double Actuation and Extended Stroke for Single Cell Studies”. *The 17th International Conference on Solid-State Sensors, Actuators and Microsystems (Transducers Eurosensors XXVII)*, pp. 46-49, 2013.  
DOI: <https://doi.org/10.1109/Transducers.2013.6626697>
- [83] Baëtens, Tiffany, Grégoire Perret, Yuki Takayama, Momoko Kumemura, Laurent Jalabert, Samuel Meignan, Chann Lagadec, Fujita Hiroyuki, Dominique Collard, and Mehmet Cagatay Tarhan, “A Practical Single Cell Analysis Method for Mechanical Characterization of Cancer Cells”. in *2017 IEEE 30th International Conference on Micro Electro Mechanical Systems (MEMS 2017)*, pp. 608-611, 2017.
- [84] P. Perret, Y. Takayama, M. Kumemura, S. Meignan, H. Fujita, C. Lagadec, D. Collard, and M.C. Tarhan, “MECHANICAL CHARACTERIZATION OF SINGLE CELLS TO DISTINGUISH DIFFERENT BREAST CANCER CELLS”. *21st International Conference on Miniaturized Systems for Chemistry and Life Sciences*, pp. 978-0-692-94183-86, 2017.
- [85] Perret, Grégoire, Po-Tsun Chiang, Thomas Lacornerie, Momoko Kumemura, Nicolas Lafitte, Herve Guillou, Laurent Jalabert, et al., “Silicon Nanotweezers with a Microfluidic Cavity for the Real Time Characterization of DNA Damage under Therapeutic Radiation Beams”. *IEEE Engineering in Medicine and Biology Society. Annual Conference 2013*, pp. 6820, 2013.  
DOI: <https://doi.org/10.1109/EMBC.2013.6611123>
- [86] Perret, Grégoire, Thomas Lacornerie, Fabio Manca, Stefano Giordano, Momoko Kumemura, Nicolas Lafitte, Laurent Jalabert, et al., “Real-Time Mechanical Characterization of DNA Degradation under Therapeutic X-Rays and Its Theoretical Modeling”. *Microsystems & Nanoengineering*, Vol. 2, pp. 16062, 2016.  
DOI: <https://doi.org/10.1038/micronano.2016.62>
- [87] Lafitte, Nicolas, Yassine Haddab, Yann Le Gorrec, Herve Guillou, Momoko Kumemura, Laurent Jalabert, Dominique Collard, and Hiroyuki Fujita, “Improvement of Silicon Nanotweezers Sensitivity for Mechanical Characterization of Biomolecules Using Closed-Loop Control”. *IEEE/ASME Transactions on Mechatronics*, Vol. 20, No. 3, pp. 1418-1427, 2015.  
DOI: <https://doi.org/10.1109/TMECH.2014.2351415>
- [88] H. Sugiura, S. Sakuma, M. Kaneko, and F. Arai, “On-Chip Method to Measure Mechanical Characteristics of a Single Cell by Using Moiré Fringe”. *Micromachines*, Vol. 6, No. 6, pp. 660-673, 2015.  
DOI: <https://doi.org/10.3390/mi6060660>

- [89] K. Nakahara, S. Sakuma, T. Hayakawa, and F. Arai, "On-Chip Transportation and Measurement of Mechanical Characteristics of Oocytes in an Open Environment". *Micromachines*, Vol. 6, No. 5, pp. 648-659, 2015.  
DOI: <https://doi.org/10.3390/mi6050648>
- [90] T. Hasegawa, S. Sakuma, K. Nanatani, N. Uozumi, and F. Arai, "Mechanical characterization system of cyanobacteria using a robot integrated microfluidic chip". in 2015 IEEE/RSJ International Conference on Intelligent Robots and Systems (IROS 2015), pp. 6033-6038, 2015.
- [91] K. Ito, S. Sakuma, M. Kimura, T. Takebe, M. Kaneko, and F. Arai, "Stiffness-index map based on single cell-spheroid analysis using robot integrated microfluidic chip". in 2016 IEEE 29th International Conference on Micro Electro Mechanical Systems (MEMS 2016), pp. 157-160, 2016.
- [92] S. Sakuma, D. Chang, F. Arai, K. Kera, and N. Uozumi, "Mechanical characterization of cyanobacteria under osmotic stress". in 2017 IEEE 30th International Conference on Micro Electro Mechanical Systems (MEMS 2017), pp. 1248-1251, 2017.
- [93] Ginestier, Christophe, Min Hee Hur, Emmanuelle Charafe-Jauffret, Florence Monville, Julie Dutcher, Marty Brown, Jocelyne Jacquemier, et al., "ALDH1 Is a Marker of Normal and Malignant Human Mammary Stem Cells and a Predictor of Poor Clinical Outcome". *Cell Stem Cell*, Vol. 1, No. 5, pp. 555-567, 2007.  
DOI: <https://doi.org/10.1016/j.stem.2007.08.014>
- [94] Stratford, Eva W., Russell Castro, Anna Wennerstrom, Ruth Holm, Else Munthe, Silje Lauvrak, Bodil Bjerkehagen, and Ola Myklebost, "Liposarcoma Cells with Aldefluor and CD133 Activity Have a Cancer Stem Cell Potential". *Clinical Sarcoma Research*, Vol. 1, No. 1, pp. 8, 2011.  
DOI: <https://doi.org/10.1186/2045-3329-1-8>
- [95] Charafe-Jauffret, E., C. Ginestier, F. Iovino, J. Wicinski, N. Cervera, P. Finetti, M.-H. Hur, et al., "Breast Cancer Cell Lines Contain Functional Cancer Stem Cells with Metastatic Capacity and a Distinct Molecular Signature". *Cancer Research*, Vol. 69, No. 4, pp. 1302-1313, 2009.  
DOI: <https://doi.org/10.1158/0008-5472.CAN-08-2741>
- [96] Lee, Gabriel Y.H., and Chwee T. Lim, "Biomechanics Approaches to Studying Human Diseases". *Trends in Biotechnology*, Vol. 25, No. 3, pp. 111-118, 2007.  
DOI: <https://doi.org/10.1016/j.tibtech.2007.01.005>
- [97] Glenister, F.K., "Contribution of Parasite Proteins to Altered Mechanical Properties of Malaria-Infected Red Blood Cells". *Blood*, Vol. 99, No. 3, pp. 1060-1063, 2003.  
DOI: <https://doi.org/10.1182/blood.V99.3.1060>
- [98] Fu-Shi Quan, Kyung Sook Kim, "Medical applications of the intrinsic mechanical properties of single cells". *Acta Biochimica et Biophysica Sinica (ABBS)*, Vol. 48, Issue 10, pp. 865-871, 2016.  
DOI: <https://doi.org/10.1093/abbs/gmw081>
- [99] Dai, Wen, Kun Lian, and Wanjun Wang, "Design and Fabrication of a SU-8 Based Electrostatic Microactuator". *Microsystem Technologies*, Vol. 13, No. 3, 271-277, 2006.  
DOI: <https://doi.org/10.1007/s00542-006-0214-z>

- [100] Zhou, Guangya, and Philip Dowd, "Tilted Folded-Beam Suspension for Extending the Stable Travel Range of Comb-Drive Actuators". *Journal of Micromechanics and Microengineering*, Vol. 13, No. 2, pp. 178-83, 2003.  
DOI: <https://doi.org/10.1088/0960-1317/13/2/303>
- [101] William A. Johnson, and Larry K. Warne, "Electrophysics of Micromechanical Comb Actuators", *Journal of Microelectromechanical Systems*, Vol. 4, No.1, pp. 49-59, 1995.  
DOI: <https://doi.org/10.1109/84.365370>
- [102] Yu Sun, S.N. Fry, D.P. Potasek, D.J. Bell, and B.J. Nelson, "Characterizing Fruit Fly Flight Behavior Using a Microforce Sensor with a New Comb-Drive Configuration", *Journal of Microelectromechanical Systems*, Vol. 14, No. 1, pp. 4-11, 2005.  
DOI: <https://doi.org/10.1109/JMEMS.2004.839028>
- [103] Montasser, I., A. W. Coleman, Y. Tauran, G. Perret, L. Jalabert, D. Collard, B. J. Kim, and M. C. Tarhan, "Direct Measurement of the Mechanism by Which Magnesium Specifically Modifies the Mechanical Properties of DNA", *Biomicrofluidics*, Vol. 11, No. 5, pp. 051102, 2017.  
DOI: <https://doi.org/10.1063/1.5008622>
- [104] Park, Jungwook, Shuhei Nishida, Pierre Lambert, Hideki Kawakatsu, and Hiroyuki Fujita, "High-Resolution Cantilever Biosensor Resonating at Air-Liquid in a Microchannel", *Lab on a Chip*, Vol. 11, No. 24, pp. 4187, 2011.  
DOI: <https://doi.org/10.1039/c1lc20608g>
- [105] Legtenberg, Rob, A W Groeneveld, and M Elwenspoek, "Comb-Drive Actuators for Large Displacements", *Journal of Micromechanics and Microengineering*, Vol. 6, No. 3, pp. 320-329, 1996.  
DOI: <https://doi.org/10.1088/0960-1317/6/3/004>
- [106] Xue, Gaopeng, Masaya Toda, and Takahito Ono, "Comb-Drive XYZ-Microstage With Large Displacements Based on Chip-Level Microassembly", *Journal of Microelectromechanical Systems*, Vol. 25, No. 6, pp. 989-998, 2016.  
DOI: <https://doi.org/10.1109/JMEMS.2016.2607233>



# Appendix A

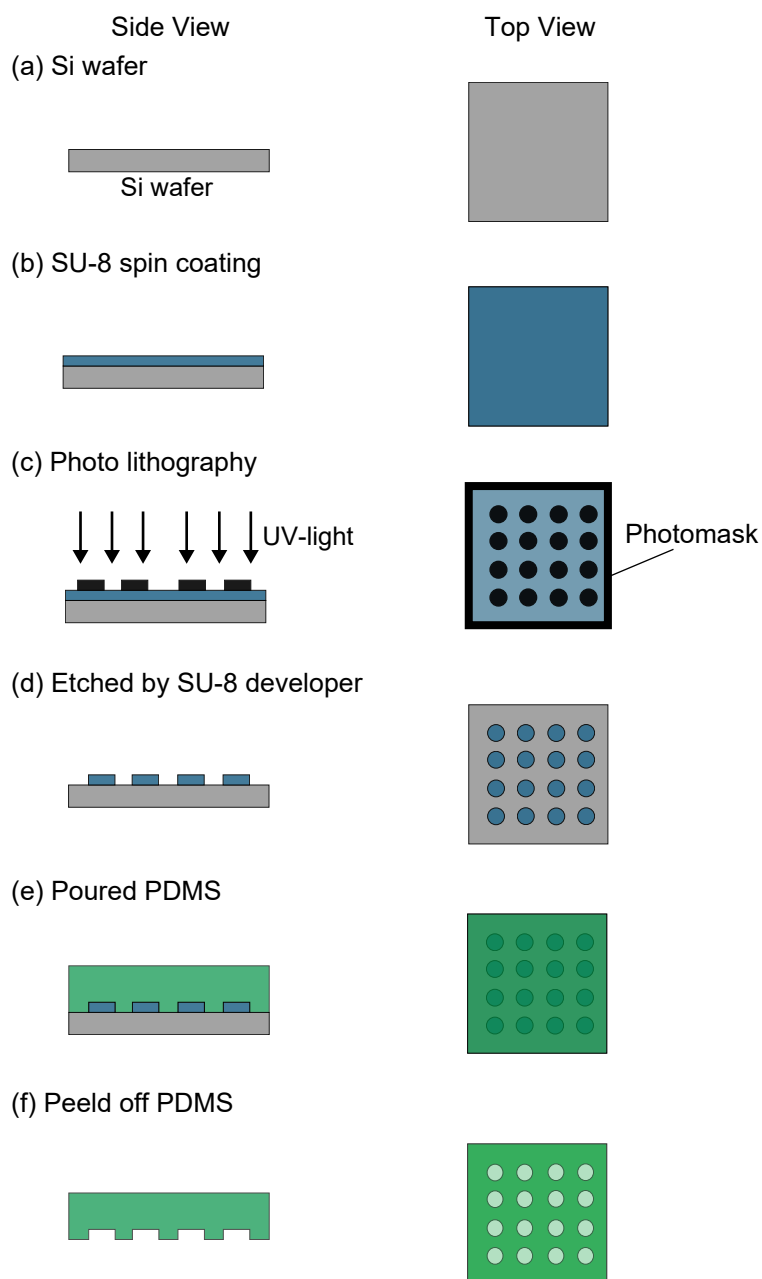
## PDMS microwell fabrication

### Fabrication

The fabrication process of PDMS mold with SU-8, and PDMS microwells are shown in **Fig. A.1**. A photomask for SU-8 lithography was manufactured in VDEC, University of Tokyo and all fabrication processes of SU-8 mold was done in IIS, The University of Tokyo, Japan.

1. A thoroughly cleaned and dried Si wafer (1 mm of thickness) was prepared as the substrate of SU-8 mold.
2. SU-8 epoxy photoresist was spun on to the wafer to the desired thickness and soft baked to remove solvent.
3. A chrome coated glass photomask was used for photolithography. The ultraviolet light exposed the mask onto the coated wafer and cured SU-8 to make the patterned area.
4. A developer solution removed unexposed resist and left behind the negative image of the mask pattern; this served as the negative mold for making PDMS structures.
5. PDMS was mixed with a mass ratio of the base to the curing agent of 10:1, a desired amount was poured onto the mould, and incubated in a vacuum chamber to avoid air bubbles appeared inside. Then, PDMS was cured on a hotplate at 90 °C for 1 hour.
6. The PDMS layer was peeled off from the mould and used as microwells. The PDMS microwells were treated by O<sub>2</sub> plasma for 30-60 s as surface treatments.

The fabricated PDMS micro wells was shown in **Fig. 2.3**. The height of PDMS microwells was around 20 μm. PDMS microwells were placed inside a petri dish for AFM measurement.



**Fig. A.1** Schematic diagram of PDMS microwell fabrication process using SU-8 mold. **(a)** Cleaning of Si wafer. **(b)** Spin coating SU-8 photoresist. **(c)** UV-light exposure through the photomask. **(d)** Developing the SU-8 to make needed patterns. **(e)** Pouring PDMS and curing on a hotplate. **(f)** Peeling off the PDMS from the SU-8 mould.

# Appendix B

## CSC staining

ALDEFLUOR™ is a reagent that identifies stem/ progenitor cells in human bone marrow/ mobilized peripheral blood/ umbilical cord blood by measuring aldehyde dehydrogenase (ALDH) enzyme activity of cells. It is also used for identification and separation of cancer stem cells and normal stem cells. ALDEFLUOR assay can detect only live stem cells and it also maintains a high survival ratio even after staining. Thus, we use it for CSC staining.

The basis for this assay is that uncharged cell ALDH (enzyme) substrate (Bodipy-aminoacetaldehyde, BAAA) is taken up by living cells via passive diffusion. Once inside the cell, BAAA is converted into negatively charged Bodipy-aminoacetate (BAA<sup>-</sup>) by intracellular ALDH. The BAA<sup>-</sup> is then retained inside the cell, causing the cell to become highly fluorescent. The protocol of staining cells is as follows:

1. Cells ( $1 \times 10^6$  cells/ mL) were single cell suspended in ALDEFLUOR assay buffer containing BAAA.
2. Incubate at 37 °C for 30 min (Mix the flask every 10 min to make homogenisation).
3. Measure with a flow cytometer to make sure the CSC staining.

Then, stained cells sort in about 3 % of CSC and 30 % of non-CSC.

# Appendix C

## Working principle

### Electrostatic actuation

The actuation is provided by electrostatic forces between comb structures, which is a commonly used method in MEMS device [99],[100]. The total displacement in a comb-drive actuator is shorter than what is possible in a parallel plate structure. However, it provides a simple control of the actuation.

A comb drive actuator generates electrostatic forces between two electrodes. A simple parallel plane model is used to explain the electrostatic field between the two electrodes [101]. The local electrostatic force in  $x$  -direction  $F_x$  were obtained as below:

$$F_x = \frac{1}{2} \epsilon_0 t \frac{V^2}{g} \times n \quad (\text{C.1})$$

where the  $\epsilon_0 = 8.854 \times 10^{-12}$  F/m is the vacuum permittivity,  $t$  is the thickness of wafer,  $V$  is the potential difference between the electrodes as the actuation voltage,  $g$  is the gap between the opposite teeth, and  $n$  is the total number of comb teeth.

### Differential capacitive sensor

A tri-plate configuration with transverse combs was used for a differential capacitive sensor [102],[74]. The sensor consists of a series of center plate electrodes  $C_0$  that moves to the fixed plate electrodes, and then, form two variable capacitances  $C_1$  and  $C_2$ . The difference of those

two  $\Delta C$  is related to the displacement,  $\Delta x$ , by:

$$\Delta C = C_2 - C_1 \quad (C.2)$$

$$\Delta C = \varepsilon_0 n L t \left[ \left( \frac{1}{d_0 - \Delta x} + \frac{1}{d_1 + \Delta x} \right) - \left( \frac{1}{d_0 + \Delta x} + \frac{1}{d_1 - \Delta x} \right) \right] \quad (C.3)$$

where  $n$  is the number of pairs of electrode combs forming capacitance  $C_1$  and  $C_2$ ,  $\varepsilon_0$  is the vacuum permittivity,  $L$  is the length of electrode plate,  $t$  is the width of a plate (device thickness),  $d_0$  is the initial gap between plates, and  $d_1$  the initial distances between repeating combs (see **Fig. 3.7**).

When  $\Delta x \ll d_0$  as a small displacement, that gives:

$$\Delta C = 2\varepsilon_0 n L t \left[ \left( \frac{1}{d_0^2} - \frac{1}{d_1^2} \Delta x \right) \right] \quad (C.4)$$

To achieve the best resolution of displacement and force,  $\Delta C$  is measured before performing experiments. A signal of sinusoidal excitation  $V_{\text{ref}}$  is supplied by the internal reference of a lock-in amplifier and applied to the fixed plate electrode  $C_0$ . Capacitive sensors that  $C_1$  and  $C_2$  of MEMS device were connected to a lock-in amplifier (Model 7230, AMETEK, Inc., Berwyn, PA, USA) *via* low noise preamplifiers (Model 5182, Signal Recovery, AMETEK, Inc., Berwyn, PA, USA). The currents flowing  $C_1$  and  $C_2$  are converted to voltages and the lock-in amplifier performs the phase detection of that differential inputs at the frequency  $f_{\text{ref}}$ . The amplitude of the output signal  $V_{\text{out}}$  is related to  $\Delta C$  (and consequently, to the  $\Delta x$ ) according to the following transfer equation:

$$V_{\text{out}} = G \cdot 2\pi \cdot f_{\text{ref}} \cdot V_{\text{ref}} \cdot \Delta C$$

where  $G$  is the preamplifier gain.

# Appendix D

## SNT fabrication process

SNT was fabricated in the Fujita laboratory clean room, IIS, the University of Tokyo. Double side microfabrication process on a (100)-oriented silicon on insulator (SOI) wafer (either type N or P; UltraSil Corporation, CA, USA) was performed. **Table. D.1** to **Table. D.4** depicts the process flow to fabricate the SNT.

### Wafer preparation

The SOI wafer thickness were 30  $\mu\text{m}$ , 2  $\mu\text{m}$  and 350  $\mu\text{m}$  for the frontside (top layer) silicon, the buried oxide (BOX) and the backside (handle layer) silicon, respectively. First, the fabrication process was carried out by cutting a 4 inch SOI wafer to 1/4 size. As a result, it was possible to maintain uniformity and could be mass-produced. The cut SOI wafer was cleaned with 10-20 min of the SPM (Sulfuric peroxide mixture) and 20-30 min of the APM (Ammonia peroxide mixture) to remove any solvent and particle on the wafer. Then, the oxide layer was removed with 1 % diluted hydrogen fluoride (HF) which formed on the wafer surface during the cleaning step.

### Frontside etching

The wafer was prebaked on a hotplate. A primer and an S1805 photoresist were coated on frontside Si at 4000 rpm in 30 s and softbaked on the hotplate. The photoresist (S1805 positive photoresist, SHIPLEY) was patterned with a height of 500 nm by photolithography as a deep reactive ion etching (DRIE) mask adopted to the frontside. The frontside elements are corresponding to main component structures, such as comb drive actuators, capacitive sensors, and

tips. The size of photomasks used for lithography in this process were 2.5 inch and were created in VDEC (The University of Tokyo).

The DRIE ended with oxygen plasma ashing step to remove residues and photoresists. After applied DRIE, SPM cleaning was carried out in order to remove the rest of photoresist, and the formed oxide on the silicon surface was removed with diluted HF again.

## **Protection layer**

Since frontside structures are the main components of SNT, they were protected by 3 consecutive layers before starting the backside process. First, by conformal thermal oxidation at 1050 °C for 30 min in dry, SOI wafer formed a thin oxide film. Then, 100 nm-thick Aluminium film was deposited thereon by evaporation. Finally, a 2- $\mu\text{m}$  photoresist (S1818 positive photoresist, SHIPLEY) was spun on the frontside surface and hard baked for 30 min. After protecting the frontside, the process moved to the backside step.

## **Backside etching**


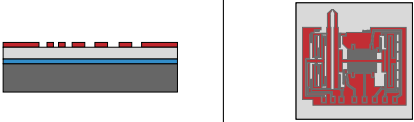
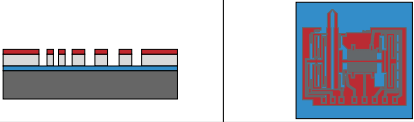
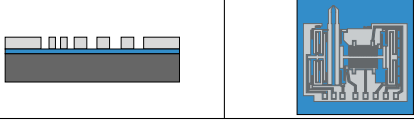
First, 100 nm of Aluminium was deposited by thermal evaporator on the backside silicon surface, and then a photoresist (S1818 positive photoresist, SHIPLEY) was spun to have a thickness of 500 nm. Patterns were formed on Aluminium by photolithography and then Aluminium was etched to make the etched mask for the backside DRIE. There are no detailed patterns on backside, it is only the connection part of frontside structures, and the handling part of the device. The DRIE was applied to the backside Si and it took time to etch 350  $\mu\text{m}$  of Si, e.g., more than 2 hours by an STS DRIE machine but less 1 hour by a Predeus machine. After backside DRIE, the etched wafer and a glass holder for DRIE were put in acetone together. The wafer gently detached from the glass holder and rinsed twice with ethanol. Since fabricated devices in the wafer have already become a fragile structure after the backside DRIE, an oven at 100 °C was used for drying the wafer instead of a nitrogen blower. The rest of Aluminium and the residue photoresist was cleaned by a final SPM in the vertical direction.

## **Releasing BOX layer**





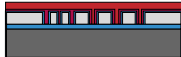

The BOX layer was released with 50 % of HF (diluted with water). A vapor HF etching is suitable for releasing because a wet etching can cause the problem of sticking structures. However, isotropic wet etching process generates a few  $\mu\text{m}$  of under-etched, and it can be controlled by the time. Thus, wet etching was applied for the releasing step. Finally, all  $\text{SiO}_2$  layers such as BOX, protection layer and the layer formed during SPM were removed by this releasing step and dried in the oven at  $100\text{ }^\circ\text{C}$  for 20 min or even more. This final etching induces an under-etching of  $\text{SiO}_2$  BOX layer at electrical pads and mechanically connections part.








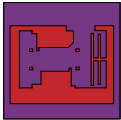

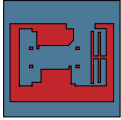
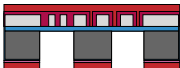
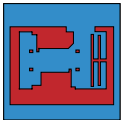
**Table D.1** Fabrication process of SNT (No.1)

Figure (Left: Cross-sectional, Right: Top)	Process	Conditions
	<ul style="list-style-type: none"> <li>· Used wafer</li> <li>· Wafer cut</li> <li>· Wafer cleaning (RCA cleaning)</li> </ul>	SOI (30/2/350) 4 inch size  Cut 1/4 size  1 % HF: 30 s SPM: 10-20 min 1 % HF: 30 s APM: 20-30 min 1 % HF: 30 s
	<ul style="list-style-type: none"> <li>· Formation photoresist (S1805) mask</li> </ul>	Prebake: 110 °C, 2-3 min  S1805 500 rpm × 5 s 4000 rpm × 30 s Softbake: 110 °C 2-3 min  Exposure: 2.3 s Develop: 1 min + $\alpha$ Rinse: water Dry: N <sub>2</sub> blower
	Patterning of frontside Si layer (DRIE)	Bosch Process
	Removal photoresist and cleaning frontside	SPM: 15 min 1 % HF: 30 s



**Table D.2** Fabrication process of SNT (No.2)

Figure (Left: Cross-sectional, Right: Top)	Process	Conditions
		<p>Formation of frontside protection layer -1</p> <ul style="list-style-type: none"> <li>· Thermal oxidation (Dry) for SiO<sub>2</sub> layer</li> </ul>
		<p>Formation of frontside protection layer -2</p> <ul style="list-style-type: none"> <li>· Evaporation Al layer</li> </ul>
		<p>Formation of frontside protection layer -3</p> <ul style="list-style-type: none"> <li>· Formation photoresist (S1818) layer</li> </ul>

**Table D.3** Fabrication process of SNT (No.3)

Figure (Left: Cross-sectional, Right: Bottom)	Process	Conditions	
		Upside down the SOI	Thin oxide layer
		Evaporation Al layer	40 W, $2 \times 10^{-5}$ Pa, 100 nm
		Formation photoresist (S1818) mask	Prebake: 130 °C, 2-3 min with nonwoven cloth wiper (BEMCOT)  S1818 500 rpm $\times$ 5 s 3000 rpm $\times$ 30 s Softbake: 130 °C 2-3 min with nonwoven cloth wiper (BEMCOT)  Exposure: 6 s Develop: 1 min + $\alpha$ Rinse: water Dry: N <sub>2</sub> blower
		Removal Al layer	Al etchant 4-7 min
		Patterning of backside Si layer (DRIE)	Bosch Process

**Table D.4** Fabrication process of SNT (No.4)

Figure (Left: Cross-sectional, Right: Bottom)	Process	Conditions
	<ul style="list-style-type: none"> <li>· Detachment from DRIE glass holder</li>   <li>· Removal photoresist, Al layer, and final cleaning</li> </ul>	<p>Acetone: 5 min            Ethanol -1: 1min            Ethanol -2: 1min            Dry: oven at 100 °C</p> <p>SPM: 15-20 min            in vertical direction            Dry: oven at 100 °C</p>
	<p>Release of BOX layer</p>	<p>Wet etching            50 % HF: 5-15 min            Dry: oven at 100 °C</p>

# Appendix E

## A built-in channel MEMS device fabrication process

### A built-in channel MEMS device

**Table. E.1** to **Table. E.4** depicts the process flow to fabricate the a built-in channel MEMS device. The built-in channel MEMS device was also fabricated in the same facilities with SNT where the Fujita lab's clean room in IIS, the University of Tokyo. The fabrication process was based on Silicon on insulator (SOI) technology. The SOI having the following characteristics: (100) oriented either N type or P type of 30  $\mu\text{m}$  Si frontside (top layer)/ 2  $\mu\text{m}$  buried oxide (BOX) insulator/ and 350  $\mu\text{m}$  Si backside (handle layer) (UltraSil Corporation, CA, USA). **Fig. 3.10** shows SEM images of fabricated device.

### Wafer preparation

The fabrication process was carried out by cutting a 4 inch of SOI wafer to 1/4 size. As a result, it could ensure the uniformity and mass-produced at the university clean room level. The cut SOI wafer was cleaned with 10-20 min of the SPM (Sulfuric peroxide mixture) and 20-30 min of the APM (Ammonia peroxide mixture) to remove any solvent and particle remaining the wafer. Then, the oxide layer was removed with 1 % diluted hydrogen fluoride (HF) which was formed on the wafer surface during the cleaning step.

## Frontside etching

The wafer was prebaked on a hotplate at 110 °C. A primer and an S1805 photoresist (S1805 positive photoresist, SHIPLEY) were spun on frontside Si at 4000 rpm in 30 s and softbaked it on the hotplate at 110 °C. The photoresist, with a height of 500 nm, was patterned by photolithography as an anisotropic deep reactive ion etching (DRIE: Si plasma etching process) mask adopted to the frontside. That would include all main component structures, such as comb drive actuators, capacitive sensors, two tips, and sidewall of microfluidic channel. The size of photomask used for lithography step in this process was 2.5 inch and the mask was produced in VDEC (University of Tokyo) by collaborators.

The wafer with the photoresist pattern was attached to a DRIE glass holder (a carrier wafer) using DP oil to tentatively glue, instead of heat grease. The DRIE formed frontside Si structures with Bosch process, and ended with oxygen plasma ashing step to remove residues or photoresists. After applied DRIE process, SPM cleaning was carried out in order to remove the rest of the photoresist. The formed oxide on the silicon surface during SPM cleaning step was removed with diluted HF again.

## Protecting the front side

Since the structures of front side contains the main component of SNT, it has to be protected by 3 consecutive layers before starting the backside process. This protection layer stays during backside etching process.

The first protection layer, an oxide thin film, formed on SOI wafer by conformal thermal oxidation at 1050 °C for 30 min in dry. Then, the second protection layer as a 100 nm-thick of Aluminium film was deposited thereon by thermal evaporation. Finally, a 2- $\mu$ m photoresist (S1818 positive photoresist, SHIPLEY) was spun on the frontside surface and hard baked in 30 min. After protecting the frontside with these three layers, the process moved to the backside step.

## Backside etching

A 100 nm of Aluminium was deposited by thermal evaporator on the backside silicon surface, and then the photoresist (S1830 positive photoresist, SHIPLEY) was spun on thereon with a thickness

of 500 nm. All patterns were formed on Aluminium by photolithography, and Aluminium was etched by an aluminium etchant to make the etched mask for the backside DRIE.

There were no detailed patterns on backside, only the connection part of frontside structures, the bottom part of the channel, and the handling part of the device. DRIE processes based on the Bosch process was applied to the backside Si surface. The required time for DRIE was depending on the equipment.

After backside DRIE process, the etched wafer and the glass holder for DRIE were put together in acetone. The wafer was gently detached from the glass holder and rinsed twice with ethanol. Some photoresist mask and DP oil as glue could be removed during this process. Since devices which fabricated in the wafer became a fragile structure after the backside DRIE, an oven at 100 °C was used for drying the wafer instead of a nitrogen blower.

The rest of Aluminium mask layer and the residue of photoresist were cleaned from both side of SOI surface by the final SPM process. In this SPM process, the fabricated wafer was put into a weak SPM solution in a vertical direction to avoid breaking fragile structures.

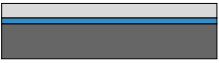
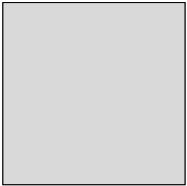

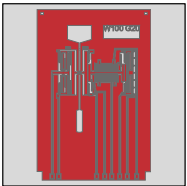
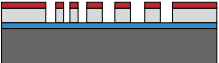
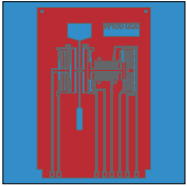
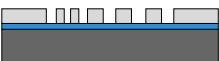
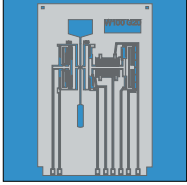
### **Releasing BOX layer**

The BOX layer was released with 50 % of HF (diluted with water). An isotropic wet etching process was easier to control. All SiO<sub>2</sub> layers such as BOX, protection layer and the layer formed during SPM were removed by this releasing step and the wafer was dried in the oven at 100 °C for 20 min or even more.

This final etching induced an under-etch of SiO<sub>2</sub> BOX layer. Of particular importance for the built-in channel MEMS device, the under-etch has to be at least 10 µm in order to release the compressing and sensing tips. The under-etch occurs not only at the tips part but also elsewhere, such as around electrical pads and mechanically connections part, however, the backside was designed as not to be affected from the under-etch.


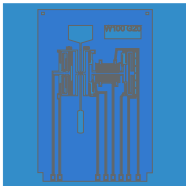

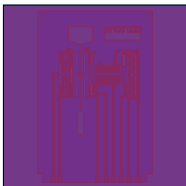
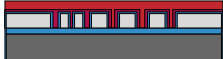
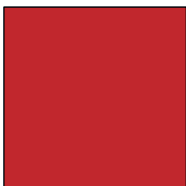
These steps allow successful fabrication of the new Device with build-in microfluidic channel.

**Table E.1** Fabrication process of the channel integrated MEMS device (No.1)


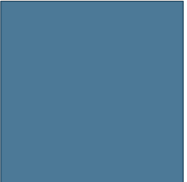

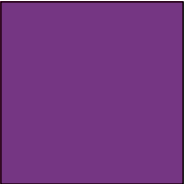

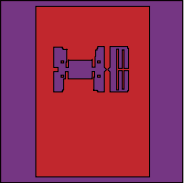

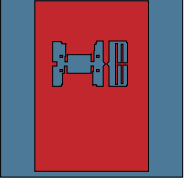
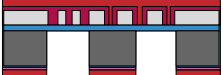
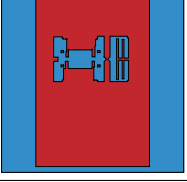
Figure (Left: Cross-sectional, Right: Top)	Process	Conditions
 	<ul style="list-style-type: none"> <li>· Used wafer</li> <li>· Wafer cut</li> <li>· Wafer cleaning (RCA cleaning)</li> </ul>	SOI (30/2/350) 4 inch size  Cut 1/4 size  1 % HF: 30 s SPM: 10-20 min 1 % HF: 30 s APM: 20-30 min 1 % HF: 30 s
 	<ul style="list-style-type: none"> <li>· Formation photoresist (S1805) mask</li> </ul>	Prebake: 110 °C, 2-3 min  S1805 500 rpm × 5 s 4000 rpm × 30 s Softbake: 110 °C 2-3 min  Exposure: 2.3 s Develop: 1 min + $\alpha$ Rinse: water Dry: N <sub>2</sub> blower
 	Patterning of frontside Si layer (DRIE)	Bosch Process
 	Removal photoresist and cleaning frontside	SPM: 15 min 1 % HF: 30 s



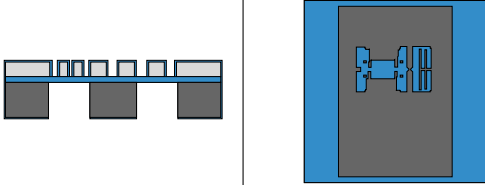
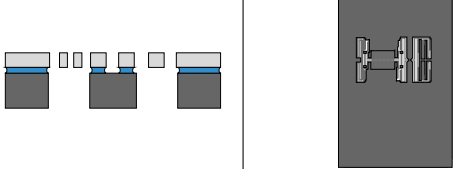
**Table E.2** Fabrication process of the channel integrated MEMS device (No.2)

Figure (Left: Cross-sectional, Right: Top)		Process	Conditions
		Formation of frontside protection layer -1 · Thermal oxidation (Dry) for SiO <sub>2</sub> layer	1050 °C × 30 min
		Formation of frontside protection layer -2 · Evaporation Al layer	40 W, $2 \times 10^{-5}$ Pa, 100 nm
		Formation of frontside protection layer -3 · Formation photoresist (S1818) layer	S1818 500 rpm × 5 s 3000 rpm × 30 s Hardbake: 130 °C over 30 min

**Table E.3** Fabrication process of the channel integrated MEMS device (No.3)

Figure (Left: Cross-sectional, Right: Bottom)	Process	Conditions	
		Upside down the SOI	Thin oxide layer
		Evaporation Al layer	40 W, $2 \times 10^{-5}$ Pa, 100 nm
		Formation photoresist (S1818) mask	Prebake: 130 °C, 2-3 min with nonwoven cloth wiper (BEMCOT)  S1818 500 rpm $\times$ 5 s 3000 rpm $\times$ 30 s Softbake: 130 °C 2-3 min with nonwoven cloth wiper (BEMCOT)  Exposure: 6 s Develop: 1 min + $\alpha$ Rinse: water Dry: N <sub>2</sub> blower
		Removal Al layer (Formation Al layer mask under photoresist)	Al etchant 4-7 min
		Patterning of backside Si layer (DRIE)	Bosch Process

**Table E.4** Fabrication process of the channel integrated MEMS device (No.4)

Figure (Left: Cross-sectional, Right: Bottom)	Process	Conditions
	<ul style="list-style-type: none"> <li>· Detachment from DRIE glass holder</li>   <li>· Removal photoresist, Al layer, and final cleaning</li> </ul>	<p>Acetone: 5 min  Ethanol -1: 1min  Ethanol -2: 1min  Dry: oven at 100 °C</p> <p>SPM: 15-20 min  in vertical direction  Dry: oven at 100 °C</p>
	<p>Release of BOX layer</p>	<p>Wet etching  50 % HF: 5-15 min  Dry: oven at 100 °C</p>

---

## PDMS cover

The PDMS top cover was fabricated using a standard soft-lithography process. **Table. E.5** shows the fabrication process flow of PDMS cover.




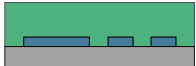

First, SU-8 epoxy photoresist (with a height of 10  $\mu\text{m}$ , SU8-2015, MicroChem, Westborough, MA) was patterned on a thoroughly cleaned Si wafer at the desired thickness and soft baked to remove solvent. The negative image of pattern was left on the Si surface as SU-8 mold for PDMS.  $\text{CHF}_3$  plasma was applied to make a surface more hydrophobic as required.

PDMS was mixed with a mass ratio of base to curing agent at 10:1, and poured on the mould. Then, PDMS was cured on a hotplate at 90  $^{\circ}\text{C}$  for 1 hour and peeled off from the SU-8 mould.

The channel top part except the handling area was formed by PDMS. The channel inlet and outlet were opened using biopsy punchers (1 mm for the inlet and 0.5 mm for the outlet).

Finally, the PDMS cover was aligned and assembled on the MEMS device to form the channel (**Fig. 3.3**).

**Table E.5** Fabrication process of PDMS cover

Figure (Left: Cross-sectional, Right: Bottom)	Process	Conditions
	- Used wafer - Wafer cleaning	Silicon wafer 1 mm <  SPM: 10-20 min
	Coat SU-8	SU-8 3010 500 rpm × 5 s 3000 rpm × 30 s Softbake: 95 °C 5-10 min
	Pattern SU-8	Exposure: 10 s Postbake: 65 °C 1 min 95 °C 5-10 min Develop: 2-5 min Rinse: IPA Dry: blower Hardbake: 200 °C 30 min Surface treatment: CHF <sub>3</sub> 50 W 3 min
	Pour PDMS	Mix base: cure agent = 1: 10 Bake: 90 °C 1 h
	Peel-off	Cut out unnecessary parts